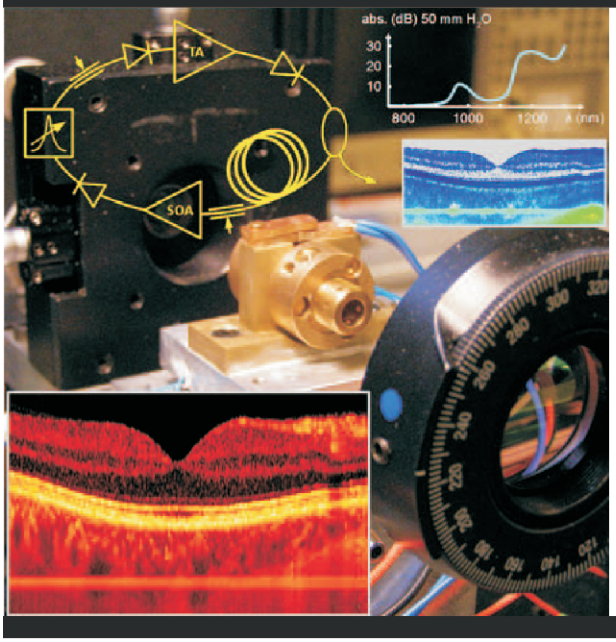

Frequency-swept Light Sources for Optical Coherence Tomography in the 1060 nm range

Sebastian Marschall

Ph.D. Thesis

June 2012

DTU Fotonik
Department of Photonics Engineering

Ph. D. thesis at the Technical University of Denmark

Frequency-swept Light Sources for Optical Coherence Tomography in the 1060 nm range

Sebastian Marschall

Supervisors
Peter E. Andersen
Christian Pedersen

DTU Fotonik, Department of Photonics Engineering
Technical University of Denmark

June 28, 2012

Abstract, English

Optical coherence tomography (OCT) is a non-invasive imaging technique for visualizing the internal structure of scattering materials, such as biological tissues. It generates two- or three-dimensional images of the sample with cellular (micrometer) resolution. OCT has become an important instrument in the biomedical field, especially in ophthalmology, where it is used for diagnosing retinal diseases. Using light at 1060 nm permits deep penetration into the retina and into the layers beneath, the choroid and the sclera. This wavelength range is also beneficial for imaging in eyes affected by cataract. For the 1060 nm band, rapidly tunable lasers—so-called *swept sources*—are available which enable ultra-high speed acquisition of large three-dimensional datasets. However, these light sources require further improvements: higher output power for sufficient signal quality and wider tuning bandwidth for better depth resolution in combination with high tuning speed.

We investigate the performance of novel semiconductor laser gain media in fiber-based high-speed swept source prototypes. We demonstrate high output power using a *tapered amplifier*, and we achieve improved depth resolution with a broadband amplifier and optimization of the light source spectrum. Both technologies are feasible for developing novel high performance swept sources, as we demonstrate by applying the prototypes in OCT imaging. Furthermore, we study numerically how absorption by water in the human eye impairs the performance of retinal imaging. Our simulation reveals a general relationship between the light source bandwidth and the optimal center wavelength, which is supported by our experimental results. This relationship constitutes an

important design criterion for future development of high-speed broadband swept sources.

Abstrakt, Dansk

Optisk kohærenstomografi (OCT) er en ikke-invasiv afbildningsteknik, som anvendes til visualisering af interne strukturer i lysspredende medier, f. x. biologisk væv. OCT danner to- eller tredimensionelle billeder af objektet med cellulær (mikrometer) opløsning. OCT er vigtig for biomedicinske anvendelser, især i oftalmologi, hvor den bruges til diagnose af nethindesygdomme. Med lys omkring 1060 nm kan man afbilde strukturer dybt i nethinden og i lagene bag den, årehinden og senehinden. Desuden er dette bølgelængdeområde fordelagtigt for afbildning af nethinden i øjne med grå stær. For 1060 nm-området findes specielle bølgelængde-skannende laser-lyskilder - såkaldte *swept sources* - som kan bruges til at optage store 3D-billeder med ultra-høj hastighed. Disse lyskilder kræver dog stadig forbedringer: højere effekt for tilstrækkelig signalkvalitet og større tuning båndbredde for bedre opløsning kombineret med høj tuning hastighed.

Vi undersøger ydeevnen af nye halvleder laser gain-medier i fiberoptiske højhastigheds-swept source prototyper. Vi demonstrerer høj effekt med en såkaldt *taperet forstærker*. Desuden opnår vi øget opløsning med en bredbånds-forstærker i forbindelse med optimering af lyskildens spektrum. Disse teknologier er velegnede til udvikling af nye swept sources med forbedrede egenskaber. Det viser vi ved at anvende prototyperne i OCT systemer. Desuden undersøger vi numerisk, gennem simuleringer, hvorledes lysets absorption i vand i det menneskelige øje påvirker afbildningen af nethinden. Vi finder en generel relation mellem lyskildens båndbrede og dens optimale centralbølgelængde, hvilket understøttes af vore eksperimentelle resultater. Denne relation udgør et vigtigt design-

kriterium for videreudvikling af bredbånds-swept sources med høj tuning hastighed.

Contents

Preface

The thesis at hand presents the results of my Ph.D. project at DTU Fotonik, the Department of Photonics Engineering of the Technical University of Denmark (DTU). I conducted the project between November 2008 and January 2012 under guidance of Prof. Peter E. Andersen and Dr. Christian Pedersen at the Risø-Campus in Roskilde, Denmark. My work was part of the European Union project FUN OCT (FP-7 Health, contract no. 201880) which is dedicated to investigating the diagnostic value of functional OCT imaging. Within the project consortium, I had the opportunity for joint work with some of our partners, namely with the groups of Dr. Robert A. Huber at the Ludwig-Maximilians-Universität (LMU), Munich, Germany, as well as Prof. Christoph K. Hitzenberger and Prof. Rainer A. Leitgeb at the Medical University of Vienna (MUW), Austria. I truly enjoyed the fruitful cooperation with all the excellent researchers of the consortium.

At this point, I want to express my sincere gratitude to my supervisors Peter Andersen and Christian Pedersen for their encouragement, guidance and support throughout the entire project. I wish to thank for plenty of valuable advice on technical matters and good practice in scientific work, for intensive discussions about new ideas, and for helpful constructive criticism.

I am indebted to Robert Huber and the members of his research group for giving me the opportunity of joint experiments at LMU, for supporting me with special equipment, and for sharing their experience. It was a pleasure to work together with Thomas Klein and Wolfgang Wieser,

and I want to thank for their invaluable help in putting different ideas to the test.

I am grateful to Christoph Hitzenberger, Rainer Leitgeb, Michael Pircher, and the members of their research groups for welcoming me at MUW and for our fruitful collaboration. I enjoyed working together with Teresa Torzicky on applying our light source prototypes in polarization-sensitive OCT, and I wish to thank her for her great commitment.

Furthermore, I owe earnest gratitude to all those who supported me during my project:

- My colleagues, Ole Jensen for teaching me how to handle tapered amplifiers, Jeppe Dam for joint work on a new tunable laser design, Michael Linde for bonding unpackaged semiconductor chips, and of course Xiaomin Liu and Lars Rishøj for teaching me the high art of fusion splicing.

- Our partners in industry and research institutes who provided equipment an technical advice: Götz Erbert, Bernd Sumpf and Karl-Heinz Hasler (Ferdinand-Braun-Institut, Leibniz-Institut für Höchstfrequenztechnik), Marcus Duelk (Exalos AG), Kevin Hsu (Micron Optics, Inc.), Kim Hansen (NKT Photonics A/S).

- Birgit Sander, Mette Mogensen, and Thomas Jørgensen for their contributions to our review article.

- The technicians and engineers of the department, Finn Pedersen, Henning Larsen, and Peter Jensen, for excellent technical support.

- The administrative staff of the department, especially Charlotte Larsen and Maria Welling, for always being helpful and making my life a lot easier.

- All my colleagues at DTU Fotonik for making the department a nice place to work at, and especially Haynes Cheng, Pernille

Klarskov, Deepak Vijayakumar, André Müller, and Peter-John Rodrigo for simply being great comrades.

- My housemates, Andrew, Thomas and Geoffrey, for making sure that I did not abandon my entire social life while writing my thesis. I owe special thanks to Andrew for proof-reading and for advice on style and language. May he forgive me sticking to AE.

Last but not least I want to thank my parents and my girlfriend Simone for always being there for me. All this would not have been possible without the unconditional support they gave me throughout this entire period.

Sebastian Marschall
June 28, 2012

Publications

We published the results achieved during the Ph.D. project in the following journal articles and conference proceedings:

- S. Marschall, T. Klein, W. Wieser, B. R. Biedermann, K. Hsu, K. P. Hansen, B. Sumpf, K.-H. Hasler, G. Erbert, O. B. Jensen, C. Pedersen, R. Huber, and P. E. Andersen, "Fourier domain mode-locked swept source at 1050 nm based on a tapered amplifier," *Opt. Express* **18**(15), pp. 15820–15831, 2010.

- S. Marschall, B. Sander, M. Mogensen, T. M. Jørgensen, and P. E. Andersen, "Optical coherence tomography—current technology and applications in clinical and biomedical research," *Anal. Bioanal. Chem.* **400**(9), pp. 2699–2720, 2011.

- S. Marschall, C. Pedersen, and P. E. Andersen, "Investigation of the impact of water absorption on retinal OCT imaging in the 1060 nm range," *Biomed. Opt. Express* **3**, pp. 1620–1631, 2012.

- S. Marschall, L. Thrane, P. E. Andersen, C. Pedersen, and K. Hsu, "Frequency-swept laser light source at 1050 nm with higher bandwidth due to multiple semiconductor optical amplifiers in series," *Proc. SPIE* **7168**(1), p. 716824, 2009.

- S. Marschall, T. Klein, W. Wieser, B. Biedermann, K. Hsu, B. Sumpf, K.-H. Hasler, G. Erbert, O. B. Jensen, C. Pedersen, R. Huber, and P. E. Andersen, "FDML swept source at 1060 nm using a tapered amplifier," *Proc. SPIE* **7554**, p. 75541H, 2010.

- S. Marschall, T. Klein, W. Wieser, B. Biedermann, K. Hsu, B. Sumpf, K.-H. Hasler, G. Erbert, O. B. Jensen, C. Pedersen, R. Huber, and P. E. Andersen, "High-power FDML laser for swept source OCT at 1060 nm," *Proc. SPIE* **7715**, p. 77150B, 2010.

- S. Marschall, T. Klein, W. Wieser, T. Torzicky, M. Pircher, B. R. Biedermann, C. Pedersen, C. K. Hitzenberger, R. Huber, and P. E. Andersen, "Broadband Fourier domain mode-locked laser for optical coherence tomography at 1060 nm," *Proc. SPIE* **8213**, p. 82130R, 2012.

- S. Marschall, T. Torzicky, T. Klein, W. Wieser, M. Pircher, E. Götzinger, S. Zotter, M. Bonesi, B. Biedermann, C. Pedersen, R. Huber, C. Hitzenberger, and P. Andersen, "High-speed polarization-sensitive OCT at 1060 nm using a Fourier domain mode-locked swept source," *Proc. SPIE* **8427**, p. 84271D, 2012.

Contributions to collaborative work

Parts of the work for this thesis were carried out jointly with collaborators, mostly within the FUN OCT consortium. Here I describe the individual contributions by me and by my colleagues.

The introductory section on the fundamentals of OCT (**Sec. 2.1**) is loosely based on our review article published in *Analytical and Bioanalytical Chemistry* [1]. The section about applications (Sec. 2.1.5) contains contributions of my co-authors. The remaining parts are originally written by me.

I constructed the high-power swept source (**Ch. 3**) in its initial configuration at DTU. The tapered amplifier had previously been developed by the Ferdinand-Braun-Institut, Leibniz-Institut für Höchstfrequenztechnik. The photonic crystal fiber (PCF) delay line with the required length was prepared by NKT Photonics. I carried out performance tests, first after assembling the laser and later after exchanging the semiconductor optical amplifier (SOA) with a newer device.

In Robert Huber's laboratory at LMU, Thomas Klein, Wolfgang Wieser, and I characterized the light source in detail and acquired first images. My role was setting up and operating the light source and assisting in the measurements and the imaging. At a later point, we equipped the light source with a faster tunable filter, a shorter delay line, and a buffering stage, and recorded first retinal OCT images (**Ch. 6**) at LMU. I assisted Thomas in preparing fiber delay lines with the exact required length and in modifying the setup. For the buffering, we integrated a fast SOA driver developed by Wolfgang.

I installed the light source in Christoph Hitzenberger's laboratory at MUW together with Teresa Torzicky, who subsequently acquired first polarization-sensitive OCT (PS-OCT) images (**Ch. 6**).

I assembled the broadband swept source (**Ch. 4**) and characterized its performance at DTU. The fast SOA driver was provided by Wolfgang

Wieser (LMU). For the control software, I extended the spectral shaping algorithm of Benjamin Biedermann (LMU) and I implemented the automatic control for the tunable filter.

I set up the light source at MUW together with Teresa Torzicky. Subsequently, Teresa acquired and processed test images (Sec. 4.2) and retinal PS-OCT images (**Ch. 6**).

I performed the simulation of the impact of water absorption on retinal imaging (**Ch. 5**) independently at DTU.

Thomas Klein and I tested the low-dispersion delay line (**Ap. A**) together at LMU. We used a swept source setup with a new high-speed tunable filter developed by Thomas. According to his measurements of the chromatic dispersion in the PCF and other fibers, we had the PCF shortened and respliced by NKT Photonics.

I conducted the experiments on gain-multiplexing (**Ap. B**) independently at DTU.

1. Introduction

Optical coherence tomography (OCT) is a relatively young imaging technique that has been developed since the early 1990s [2]. OCT non-invasively generates hi-resolution two- or three-dimensional images of scattering samples and has its main applications in medicine and biological research. With micrometer resolution and millimeter penetration depth, it fills the gap between other imaging modalities providing either deeper penetration (e. g. ultra-sound) or very high resolution (e. g. confocal microscopy).

OCT is based on one-dimensional interferometric reflectometry and ranging techniques that were developed during the 1980s for inspection of optical fibers and waveguide devices [3–5] or for eye length measurements [6, 7]. In 1991, Huang et al. extended the technique by a lateral scan in order to acquire cross-sectional images of the sample, and coined the term optical coherence tomography [2]. They examined biological specimen, like human retina and coronary artery, and demonstrated thus the potential for medical applications.

In 1996, the first system for ophthalmology was commercialized by Humphrey Instruments (now subsidiary of Carl Zeiss Meditec), and since then, OCT became a standard technique for diagnosing retinal diseases and for treatment monitoring [8, 9]. During the past years, systems for intra-vascular imaging entered the market and are expected to become established instruments in cardiology [10, 11]. Intensive research focuses on the development of OCT for other fields such as dermatology [12, 13], gastroenterology [14–16], pulmonology [17], and urology [18]. Typical applications are detection and classification of cancer and pre-cancer

conditions, as well as treatment monitoring or surgery guidance. OCT has also become a valuable tool for developmental biology [19], and can be applied for various technical purposes, e. g. non-destructive material testing or contact free thickness measurements [20].

OCT maps the intensity of light backscattered from different depths in the sample. It gains contrast from variations or discontinuities in the index of refraction and images thus the internal sample structure. In addition, a variety of functional extensions enable spatially resolved measurement of other quantities, such as birefringence [21], flow of liquid [22, 23], elasticity [24], distribution of various substances [25], or optical properties [26, 27].

Biomedical imaging applications typically utilize the optical window between 600 nm and 1300 nm [28]. Due to low absorption by water, wavelengths around 800 nm have traditionally been used for retinal OCT imaging where the probing beam has to pass the vitreous humor twice. Light at 1300 nm is useful for deep penetration into most tissues, such as skin or the coronary artery wall, because of lower absorption by melanin [29] and decreased scattering [30, 31]. The intermediate range around 1060 nm is interesting for deep penetration into the layers beneath the retina (choroid and sclera) [32], because water absorption is lower than at 1300 nm and scattering is weaker than for shorter wavelengths. It is also advantageous for imaging in eyes affected by a cataract [33], and may hence become established in clinical OCT systems, as soon as certain technical challenges have been solved.

There are different ways to implement an OCT system, and the optimal choice depends strongly on the application. Most state-of-the-art research systems acquire the data in the frequency domain, i. e. they probe the sample response to illumination at different optical frequencies [34]. This can be done using a broadband light source for illumination and a spectrometer for detection [35, 36]. Alternatively, one can use a single photodetector in conjunction with a tunable narrowband light source [37, 38], also called a *swept source*. Governed by the avail-

ability of necessary hardware, OCT systems operating below 1000 nm are almost exclusively spectrometer-based, whereas most "long-wave" systems employ a swept source [39].

A swept source is typically a continuously tunable laser based upon a semiconductor gain medium. Semiconductors are very compact, efficient, and convenient in handling, and enable—in contrast to doped crystals or fibers—very fast tuning and even tailoring of the gain spectrum. With fiber-coupled *semiconductor optical amplifiers* (SOAs) and other components developed for telecommunication, one can implement stable and robust fiber-based swept sources [40], most prominent the so-called *Fourier domain mode-locked* (FDML) lasers [41], which enable ultra-fast image acquisition [42].

Swept source OCT (SS-OCT) at 1060 nm is interesting for in vivo retinal imaging, because it enables the acquisition of large 3D-volumes in a very short time [43], thereby minimizing the impact of motion artifacts [44] caused by permanent movements of the eye. However, the implementation of suitable light sources for this band is more challenging than for the 1300 nm range, which offers a variety of highly developed components for telecommunication. During the past few years, similar components have also become available for the 1060 nm band, however these exhibit generally lower performance. SOAs have lower peak gain, their bandwidth is narrower and they provide less optical power. Passive components, such as optical isolators or circulators, suitable for broadband operation are hardly available or very expensive. Furthermore, conventional optical fibers exhibit strong chromatic dispersion in the 1060 nm range, which is a limiting factor for the performance of FDML lasers [45].

The aim of this project is to investigate a number of concepts to improve the performance of swept sources at 1060 nm. We have developed a prototype FDML laser incorporating a *tapered semiconductor gain chip* that generates abundant output power. Although swept source power in the 1060 nm band can be boosted with ytterbium-doped fiber amplifiers

(YDFAs) [43, 46, 47], an exclusively semiconductor-based approach, as we present, offers considerably greater flexibility for future development.

An approach to compensate for chromatic dispersion in this setup by using a specialty *photonic crystal fiber* (PCF) has not improved the overall performance. However, as the experiment revealed, increasing the gain with an additional SOA is a viable method for achieving stable broadband FDML operation, even under non-ideal conditions.

We have implemented another simplified prototype swept source featuring a new *broadband SOA* with a gain spectrum coinciding perfectly with the local water absorption minimum at 1060 nm. By rapid modulation of the pump current, we can optimize the light source spectrum and improve the depth resolution achievable in OCT imaging.

Motivated by the continuing development of broadband light sources, we have investigated numerically how the *water absorption bands* above and below 1060 nm impair the OCT resolution, and whether compensation by shaping the light source spectrum is feasible. As our simulation shows, currently available swept sources are only minimally affected as long as their spectrum is centered on the absorption minimum. This applies to both prototypes we have developed in this project. We also obtain a general relationship for the optimal center wavelength depending on the bandwidth, which is an important design criterion for future development of ultra-broadband swept sources.

By acquiring in vivo OCT images of the human retina using both light source prototypes, we have demonstrated the feasibility of the technologies under investigation. From the practical experience with both configurations, we can derive directions for future development that will lead to the next generation of high-performance swept sources.

This thesis is organized as follows. Chapter 2 provides the necessary background information on OCT in general and more specifically on swept sources. The subsequent chapters present the implementation and performance characterization of the high-power swept source (Chapter 3) and the broadband swept source (Chapter 4). Chapter 5 covers

the numerical simulation of the effects of water absorption on the imaging performance. Chapter 6 shows retinal images acquired with both prototypes, and discusses the light source performance in OCT imaging. Chapter 7 summarizes all results and puts them into perspective with the continuing development of swept sources.

2. Fundamentals

This chapter provides the fundamental knowledge that this project is based on. It is divided into two parts. Sec. 2.1 covers the theoretical framework of optical coherence tomography (OCT), explains which factors influence the performance, and gives a brief overview ofr functional imaging modalities and biomedical applications. Sec. 2.2 focuses specifically on swept sources. It explains the key parameters for swept source OCT performance, different swept source embodiments, and important methods for data processing and performance characterization. It also includes a description of the type of light source that our prototypes are based upon and of the methods that we are using for characterization.

2.1. Optical coherence tomography

Optical coherence tomography (OCT) is an interferometric technique that detects reflected or backscattered light from turbid optical media and retrieves depth-resolved reflectivity profiles of the sample. In every optical coherence tomography (OCT) system, the reflections from the sample interfere with a reference beam originating from the same light source as the probing beam. From the resulting interferogram, one derives the reflectivity profile along the beam axis. This one-dimensional depth scan is commonly termed *A-scan*, in analogy to ultrasound imaging. By scanning the probing beam laterally across the sample, OCT systems perform many adjacent A-scans, which are then combined into two- or three-dimensional images (called B-scans or C-scans, respectively).

This chapter provides a theoretical description of the signal generation and describes different ways of implementing OCT (Sec. 2.1.1). It discusses the important system parameters (Sec. 2.1.2) and the influence of sample properties (Sec. 2.1.3). It also gives a brief overview of functional OCT imaging (Sec. 2.1.4) and the typical applications of OCT (Sec. 2.1.5). The theory part in Sec. 2.1.1 includes the important equations for understanding the underlying principles of OCT, but no detailed derivations. Those can be found in any textbook covering interference phenomena and coherence theory of electro-magnetic waves, e. g. *Fundamentals of Photonics* by Saleh and Teich [48].

2.1.1. Principle of operation

The variety of different OCT implementations can be divided into two classes depending on whether the depth-sectioning is performed in the *time domain* or in the *frequency domain*. Time domain OCT (TD-OCT) systems were the first to be implemented [2]. They work on the principle of *low coherence interferometry* (LCI), a technique for determining the time that light needs to travel a short distance to a reflecting structure and back. Direct measurement of the time of flight is normally not possible, but by means of LCI, one can compare the time delay relative to light traveling along a reference path. In order to understand this principle, let us assume a simple Michelson interferometer (Fig. 2.1, left). Incident beams from a light source with power spectral density $S_{src}(\omega)$ are reflected from a sample surface with reflectivity R_S and a reference mirror with reflectivity R_R, and interfere afterwards on a detector. The spectral density on the detector is then

$$\begin{aligned} S_{det}(\omega,\tau) = &\frac{1}{4}(R_R + R_S)S_{src}(\omega) \\ &\pm \frac{1}{2}\sqrt{R_R R_S}\ S_{src}(\omega)\cos(\omega\,\tau), \end{aligned} \tag{2.1}$$

where ω is the angular frequency of the electromagnetic field and τ the time delay between the light propagating in the two interferome-

ter arms.* The sign of the second term depends on the phase shift in the beam splitter. It is positive at one interferometer output and and negative at the other.†

A single detector (e. g. a photodiode) at the interferometer output measures the integrated intensity

$$\begin{aligned} I_{det}(\tau) &= \int_0^\infty S_{det}(\omega,\tau)d\omega \\ &= \frac{1}{4}(R_R + R_S)I_{src} \pm \frac{1}{2}\sqrt{R_R R_S}\ I_{src}\ |\gamma(\tau)|\ \cos(\omega_c\,\tau), \end{aligned} \tag{2.2}$$

where ω_c is the center frequency and $\gamma(\tau) = \langle E^*_{src}(t)E_{src}(t+\tau)\rangle / I_{src}$ is the normalized auto-correlation function, or coherence function, of the probing light. According to the Wiener-Khintchin theorem, $\gamma(\tau)$ is the Fourier transform of $S_{src}(\omega)$. $|\gamma| = 1$ if $\tau = 0$ and goes to zero if $|\tau|$ becomes large compared to the coherence time, τ_{coh}, which is a measure of the width of $|\gamma|$. The second term in Eq. 2.2 contains hence information about the relative position of the sample surface. As τ varies, there will be a modulation of the detected intensity as long as $\tau \approx \tau_{coh}$ (Fig. 2.1, right). From this condition arises the so-called *coherence gate*, a narrow range in the sample beam around the point where the optical path length equals the length of reference path. If the coherence gate is scanned (by a translation of the reference mirror) through a sample consisting of multiple partially reflective layers, only reflections within the coherence gate contribute to the modulation of I_{det}. Given by the Fourier transform relationships, τ_{coh} is inversely proportional to the spectral width, $\Delta\omega$, of the probing light, i. e. by using a broadband light source, one can create a narrow coherence gate for discriminating reflections from different positions.

*In the following derivations, we will express all relations in terms of ω and τ, as it is typically done in coherence theory. Later on, for discussing OCT performance, we will use more intuitive quantities, namely the ordinary optical frequency $\nu = \frac{1}{2\pi}\omega$, and the distance $z = \frac{1}{2}c\,\tau$ measured from the reference plane, where c is the speed of light.

†In a Michelson interferometer, the input port is at the same time also an output.

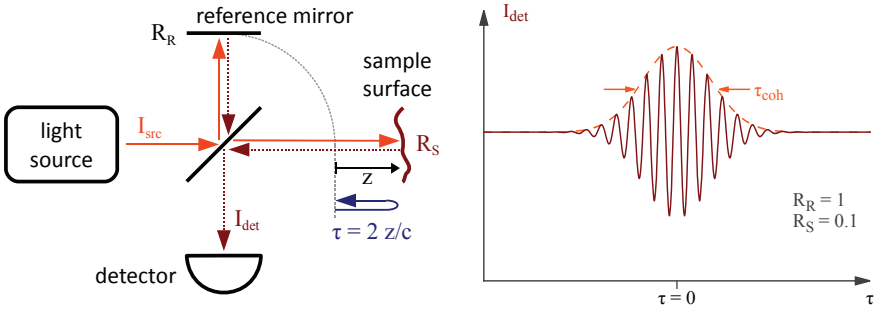

Figure 2.1.: Left: Every OCT system uses an interferometer to determine the time delay, τ, between light reflected from a sample and light traveling a reference path. Right: Time domain interferogram resulting from a single sample reflection.

The signal from multiple weakly reflective layers with reflectivity R_i is

$$\begin{aligned} I_{det} = &\frac{1}{4} I_{src}(R_R + \sum_i R_i) \\ &+ \frac{1}{2} I_{src} \sum_{i \neq j} \sqrt{R_i R_j}\ |\gamma(\tau_{ij})|\ \cos(\omega_c\, \tau_{ij}) \\ &\pm \frac{1}{2} I_{src} \sum_i \sqrt{R_R R_i}\ |\gamma(\tau_i)|\ \cos(\omega_c\, \tau_i), \end{aligned} \tag{2.3}$$

where τ_i is the time delay between the reference path and the i-th layer and $\tau_{ij} = \tau_i - \tau_j$. The signal is contained in the third term of Eq. 2.3, whereas the second term arising from interference between the different reflections within the sample adds to the constant background. The summands in the signal term carry not only information about the positions of reflecting structures, but through $\sqrt{R_i}$ also a measure of their reflectivity. The envelope of I_{det} (as function of the reference mirror position) retrieved by demodulation yields thus the reflectivity profile along

the probing beam axis. The envelope of the interference term from a single reflection, given by $|\gamma(\tau)|$, is called the axial *point spread function* (PSF). Because the signal amplitude also scales with $\sqrt{R_R}$, very weak reflections can be detected with appropriate adjustment of the reference arm intensity.

A *dual balanced detector* that measures the intensity difference between both interferometer outputs cancels out the contributions not arising from interference between the sample beam and the reference beam (i. e. the first and second term in Eq. 2.3) [49, 50]. By eliminating the intensity baseline, one can thus use the full dynamic range of the detection system for the actual signal and suppress a large proportion of the intensity noise.

Using Eq. 2.1, we can also derive the principle of depth scanning in frequency domain OCT (FD-OCT). With a constant time delay, τ, the detected power spectral density, $S_{det}(\omega)$, is modulated with a frequency proportional to τ. In the presence of multiple reflecting layers in the probing beam, the spectrum is a superposition of different frequency components that can be discriminated by a Fourier transform [34]. Hence, by measuring the spectral response of the interferometer, one can locate the position of the reflecting layers without changing the reference path length.

There are two basic ways to measure S_{det} as a function of the optical frequency. One can illuminate the interferometer with broadband light and separate the spectral components with a spectrometer at the output [34–36]. This method is termed *spectral domain OCT* (SD-OCT). Alternatively, using a tunable narrowband light source, one can probe with different optical frequencies sequentially and measure the output intensity with a single photodetector [37, 38, 51]. Such a light source performs a sweep over a broad range of optical frequencies, which led to the term *swept source OCT* (SS-OCT)[‡].

[‡]Throughout the literature, there is no uniform terminology for the OCT schemes with frequency domain depth sectioning. The terms “frequency domain OCT” and

We can understand the principle of FD-OCT by looking at a swept source system. (A similar derivation, with some quantities redefined, is also applicable to SD-OCT.) A swept source has an instantaneous line spectrum, S_l, of narrow, but non-zero width with a varying center frequency, ω_l. The instantaneous intensity of the light source varies typically with ω_l:

$$I_{src}(\omega_l) = \int_0^\infty S_l(\omega_l, \omega) d\omega. \tag{2.4}$$

By adapting Eq. 2.2, we can now derive the detected intensity at the interferometer output (Fig. 2.2, left), assuming a single reflection from a sample with time delay τ_S:

$$\begin{aligned} I_{det}(\omega_l) = &\frac{1}{4}(R_R + R_S) I_{src}(\omega_l) \\ &\pm \frac{1}{2}\sqrt{R_R R_S}\ I_{src}(\omega_l)\ |\gamma_l(\tau_S)|\ \cos(\omega_l \tau_S). \end{aligned} \tag{2.5}$$

γ_l is the normalized coherence function of S_l. In order to understand its influence, we assume here that $|\gamma_l|$ does not vary with ω_l, although it generally does, to some extent [52, 53]. In the second term of Eq. 2.5, I_{src} forms a spectral envelope to the cosine, while the factor $|\gamma_l|$ reduces the amplitude when τ_S becomes large compared to the coherence time of γ_l. The latter effect can be understood as a result of the non-zero linewidth that limits the ability to resolve very fast modulations in the spectrum.

"spectral domain OCT" may be interchanged, or "Fourier domain OCT" may be used for either one. "swept source OCT" is also called "optical frequency domain imaging", while spectrometer-based OCT was formerly referred to as "spectral radar".

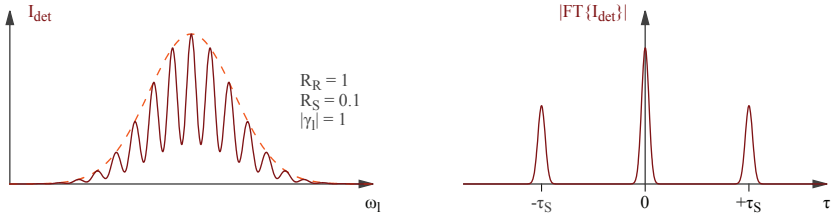

Figure 2.2.: Left: Frequency domain interferogram resulting from a single sample reflection. Right: Fourier transform of the interferogram.

The Fourier transform (FT) of the detected signal into the time domain is then

$$\begin{aligned}\mathrm{FT}\{I_{det}\}(\tau) =& \frac{1}{4}(R_R + R_S)\ \mathrm{FT}\{I_{src}\}(\tau) \\ &\pm \frac{1}{2}\sqrt{R_R R_S}\ |\gamma_l(\tau_S)|\ \mathrm{FT}\{I_{src}\}(\tau) \\ &\otimes \left[\delta(\tau - \tau_S) + \delta(\tau + \tau_S)\right],\end{aligned} \tag{2.6}$$

where $\otimes$ denotes a convolution and δ the Dirac delta function. It comprises a peak centered at zero, plus a peak at $\tau = \tau_S$ representing the reflection (Fig. 2.2, right). Because the Fourier transform is performed on a real even function, it yields also a mirror peak at $\tau = -\tau_S$. This ambiguity divides the effective imaging range in half, if one does not retrieve the full analytical signal of the interferogram with additional measures [54–60]. All peaks are convolved with $\mathrm{FT}\{I_{src}(\omega_l)\}$, which is the point spread function (PSF) in FD-OCT. The peak width is hence inversely proportional to the spectral bandwidth of the swept source. Due to the factor $|\gamma_l|$, the peak amplitude drops when τ_S gets large. This is often referred to as *sensitivity roll-off*. In case of multiple reflections from the sample, the equations get an additional term (analogous to Eq. 2.3) caused by the interference between these reflections. After

the Fourier transform, these create a weak parasitic signal in the vicinity of $\tau = 0$.

Similar equations are also valid for SD-OCT. The power spectrum of the broadband light source takes then the place of $I_{src}(\omega_l)$, and the sensitivity roll-off arises from the limited spectral resolution of the spectrometer and the pixel-size of the detector array.

None of the different OCT embodiments can be singled out as generally superior. The optimal choice always depends on the specific application. In recent years, FD-OCT has become increasingly popular for research and medical applications, due to its significantly higher imaging speed. FD-OCT allows for very high A-scan rates, because it requires no mechanical scanning of the reference path length. This advantage comes, however, at the cost of higher data processing complexity, sensitivity roll-off, and signal ambiguity for positive and negative delays that requires additional measures for compensation [54–60]. The choice between SD-OCT or SS-OCT depends mainly on the operating wavelength range [39]. For wavelengths below 1000 nm, SD-OCT is favored because silicon-based line cameras with sufficient pixel number and high read-out speed are readily available. Higher wavelengths require InGaAs-based cameras that are more expensive and not as technologically advanced. However, high-performance swept sources for the 1300 nm range can be implemented using semiconductor gain-media and optical components developed for telecommunication. During the past few years, similar components have also become available for the intermediate band between 1000 nm and 1100 nm. While in SS-OCT the light source is highly complex, the detection hardware is comparably simple. This enables uncomplicated implementation of dual balanced detection or ultra-high speed image acquisition with multiple probing beams [42, 43]. Furthermore, SS-OCT is less affected by sample motion than SD-OCT [44], and it can provide a significantly longer depth range [61–64].

2.1.2. Figures of merit

A number of characteristics are important to describe the performance of an OCT system and to compare OCT with other imaging techniques.

The main strength of OCT is the depth resolution or *axial resolution*. It is defined as the full width at half maximum (FWHM) of the point spread function (PSF), which is given by the Fourier transform of the light source power spectrum (Eqs. 2.2 and 2.6). For a Gaussian spectrum with FWHM $\Delta\nu$, the axial resolution in a medium with refractive index n is

$$\delta z = \frac{2\ln 2}{\pi}\frac{c}{n\ \Delta\nu} \tag{2.7}$$

$$\approx \frac{2\ln 2}{\pi}\frac{\lambda_c^2}{n\ \Delta\lambda} \approx 0.44\frac{\lambda_c^2}{n\ \Delta\lambda}. \tag{2.8}$$

Eq. 2.8 is commonly used for expressing this relationship in terms of the wavelength bandwidth, $\Delta\lambda$, and the center wavelength, λ_c.[§] With typical light sources, for instance superluminescent diodes (SLDs), a resolution around 5–10 µm (in biological tissue, $n \approx 1.4$) is possible, whereas ultra broadband light sources, such as femtosecond lasers or supercontinuum sources, can provide a resolution of few micrometers or less [65–68].

The *transverse resolution* of OCT is moderate, typically several 10 µm. In contrast to most optical microscopy techniques, such as confocal microscopy [69], OCT gains depth resolution not from an objective with high numerical aperture (NA), but from the coherence gate. Hence, one uses normally a low NA objective that provides a long depth of focus covering the entire depth range. This results, however, in a relatively wide focal spot. A number of techniques have been developed

[§]Statements about the "theoretical resolution" derived from the light source bandwidth should be treated with care. Many authors often ignore the fact that Eq. 2.8 is a first-order approximation and hence inaccurate with increasing $\Delta\lambda$. Furthermore, the equation is frequently applied to non-Gaussian spectra where it is hardly meaningful at all.

that permit focusing tightly for high transverse resolution while maintaining a long imaging depth range. TD-OCT allows for dynamic focusing, i. e. during each A-scan, the sharp focus can be shifted through the sample synchronously with the coherence gate. In FD-OCT, several images acquired at the same site with different focal planes can be compounded [70, 71]. In both domains, one can implement optical coherence microscopy (OCM), where so-called en-face images are acquired in a plane transverse to the probing beam [72]. OCM combines the high spatial resolution of confocal microscopy with the depth-selective coherence gate of OCT.

The *penetration depth* of OCT into typical biological samples is on the order of 1–2 mm, which is higher than that of most other high-resolution imaging techniques. OCT closes hence the gap between modalities providing either deep penetration (e. g. ultra-sound) or very high resolution (e. g. confocal microscopy).

Important for deep penetration into scattering samples is a high *sensitivity*, which is defined as the smallest detectable reflectivity. The sensitivity mostly depends on the detection efficiency and noise sources present in the system. Most OCT systems achieve a sensitivity in the range of 90–100 dB. In FD-OCT, the *sensitivity roll-off* can be an additional limiting factor for the imaging range. SD-OCT systems with high-resolution spectrometers can maintain a roll-off $\leq$ 6 dB[¶] up to $z \approx 2$ mm [73]. With special swept sources, this range can be longer than 10 mm [64].

The *imaging speed* is primarily given by the A-scan acquisition rate and is therefore limited by the reference path scanning velocity in TD-OCT, the line camera read-out rate in SD-OCT, or the sweep rate of the light source in SS-OCT. Fast image acquisition is important for sampling large volumes—especially for in vivo imaging where sample motion cannot be avoided [44]—and it opens the possibility of observing dynamic phenomena temporally resolved [74, 75]. State-of-the-art research sys-

[¶]Which corresponds to a 50% reduction of the interferogram amplitude.

tems feature A-scan rates up to several hundred kilohertz. The fastest high-quality imaging reported to date was demonstrated in a multi-beam SS-OCT system performing 20.8 million A-scans per second [42].

2.1.3. Optical properties of the sample

Apart from the hardware parameters, the performance of OCT imaging is also influenced by sample properties. *Absorption* and *scattering* attenuate the signal, thereby reducing the penetration depth [30]. A mismatch of *chromatic dispersion* in the sample and the reference path leads to a degradation of axial resolution, and should be compensated by inserting dispersive elements into the reference arm [76] or by signal-processing [77, 78].

In biological tissue, the maximum imaging depth is limited by strong scattering [79]. Scattering arises from variations in the index of refraction between different tissue constituents and the surrounding medium [80]. It is dependent on the size and shape of present scatterers, hence the macroscopic scattering properties of different tissue types can vary considerably. Absorption can mostly be avoided by an appropriate choice of the wavelength band. Between 600 nm and 1300 nm, the absorption by water and other typical tissue constituents like melanin or hemoglobin is low (Fig. 2.3, left) and forms an *optical window* [28].

The selection of an operating wavelength within this window depends on the requirements of the application. Light at 1300 nm allows for deep penetration into most tissues, such as skin, arterial wall, or mucosa [31, 79], because absorption by melanin [83] and scattering [84–86] decrease with increasing wavelength. Longer wavelengths, e. g. around 1550 nm or 1700 nm, may enable even deeper penetration for applications where water absorption has no significant influence [87, 88]. However, these wavelength ranges are not suited for probing the human posterior eye segment in vivo due to strong signal attenuation by water, which is the main constituent of the eye [89]. Commonly, wavelengths around 800 nm, where absorption by water is very low, are used for retinal imag-

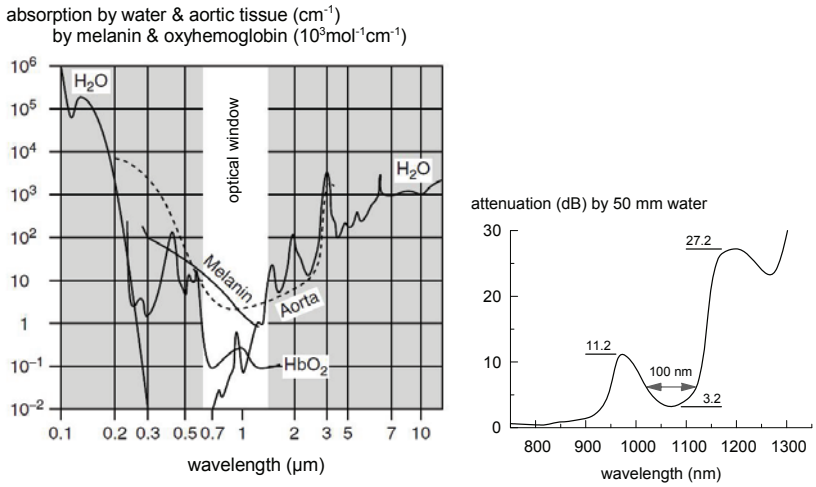

Figure 2.3.: Left: The wavelength band between 600 nm and 1300 nm is well suited for optical imaging, due to relatively low absorption by typical tissue constituents. Adapted from [81]. Right: In addition to wavelengths below 900 nm, there is an intermediate range around 1060 nm, where sufficiently low water absorption permits retinal imaging. Note: transmission through 50 mm water corresponds approximately to a double-pass through a human eye. Data from [82].

ing. There is also an intermediate range around 1060 nm with relatively low water absorption (Fig. 2.3, right). This spectral window is attractive, because weaker absorption in the retinal pigment epithelium (RPE) and decreased scattering in tissue compared to the shorter wavelengths permit deep penetration into the choroid and the sclera beneath the retina [32, 90]. It proved also beneficial for imaging in eyes affected by a cataract [33], and it exhibits minimal chromatic dispersion in water [91].

OCT images of highly scattering samples, like most biological tissues, are subject to *speckles*, i. e. a grainy fine structure caused by interference

of light reflected from many randomly distributed scatterers within the probing volume [92]. Speckle characteristics, such as the size and the intensity distribution, can provide additional information about the underlying scatterers [93, 94]. However, the speckle texture obscures small features in the image and is usually considered a source of noise. Numerous speckle reduction methods have therefore been developed and applied to OCT [92]. Some are based on incoherent addition of several signals from the same location under varying conditions, e. g. angular compounding [95], spatial compounding [96, 97], and frequency compounding [98]. Where compounding is not feasible different image processing techniques can be applied to suppress speckle, e. g. various types of smoothing filters, deconvolution [99,100], wavelet analysis [101], rotating kernel transformation [102], and anisotropic diffusion [103].

2.1.4. Functional imaging

In the basic implementation, OCT generates reflectivity images, which are related to the internal morphology of a sample. However, there are a variety of possibilities for extracting additional functional information, such as polarization properties, local motion, chemical composition or optical and mechanical properties of the sample.

Polarization-sensitive OCT (PS-OCT) detects the polarization state of the of the light backscattered from the sample [21, 104], which can be influenced by birefringent, diattenuating, or depolarizing structures [105–107]. Different implementations of PS-OCT can measure the phase retardation between the orthogonal polarization states [21, 104], the Stokes vector of the backscattered light [108], Müller and Jones matrix distribution [109, 110], optical axis orientation [111], and diattenuation [106]. PS-OCT data have proven valuable for delineating different layers in retinal images [112], for visualizing the orientation of birefringent fiber layers [107] or for detecting strain fields in material samples [113].

By analyzing the OCT signal, one can extract the Doppler shift of the backscattered light caused, for instance, by blood flow in tissue [22, 23]. State-of-the-art *Doppler OCT* systems, which derive the velocity from the phase difference between two subsequent A-scans [114], enable high-resolution, real-time imaging with sub-millimeter per second velocity sensitivity.

OCT is also capable of detecting microscopic displacements or motion within a sample. In conjunction with the controlled application of stress (force per unit area) or vibrations, one can thus map the elasticity of a specimen. Several approaches are commonly referred to as *optical coherence elastography* [115], for instance, tracking local displacements in the speckle pattern during application of constant stress [24, 116, 117] or detecting the Doppler shift while exciting mechanical vibrations in the material [118–121].

A wide variety of extensions to OCT have been developed to retrieve information about the chemical composition of a sample [25, 122]. For instance, *spectroscopic OCT* aims at detecting substances, such as hemoglobin, by identifying the absorption finger prints within the broad light source spectrum [123, 124] or by comparing the signal attenuation in different wavelength bands [125, 126]. OCT can also gain specific contrast from coherent non-linear processes [127], e. g. *second harmonic generation* or *coherent anti-Stokes Raman scattering* (CARS) [128].

Furthermore, *exogenous contrast agents* can provide specificity. These can, for instance, be near-infrared (NIR) dyes in conjunction with spectroscopic OCT [129] or with a pump-probe technique [130], or microspheres [131, 132] and nanoparticles [133, 134], which locally enhance the scattering. One can, for example, utilize them in order to increase the contrast between blood vessels and surrounding tissue [131], or target them to specific markers [129], e. g. receptors expressed on diseased or cancerous cells [135].

By analyzing reflectivity-based A-scans, one can extract optical properties, such as the refractive index [26] or the scattering coefficients

[27, 136, 137], for instance in order to detect and characterize pathologic changes in tissue samples. However, since the contributions of scattering and absorption are difficult to separate, the focus of research in recent years has been instead on deriving diagnostic information from the total attenuation coefficient [138–141].

2.1.5. Applications

OCT has found manifold applications in medicine and biology, as well as a variety of technical applications.

In *ophthalmology*, OCT is used for direct imaging of the ocular structure in the anterior and posterior segments of the human eye [142–144]. OCT has been very successful as a non-invasive, contact-free modality capable of generating high-resolution cross-sectional images of retinal structures that are inaccessible with any other technique (Fig. 2.4, left). It is today the clinical standard for diagnosis and treatment control in retinal diseases, such as age related macular degeneration [145], diabetic retinopathy [146, 147], and glaucoma [148]. Additionally, OCT is a valuable instrument for nearly all fields of ophthalmology, such as monitoring and follow-up after eye surgery, detecting macular holes and vascular occlusions, as well as examination of the anterior eye segment [149–152].

Integrated into an endoscope, OCT has also become a powerful tool for *cardiology* [10]. Similar to intravascular ultrasound imaging, OCT can visualize cross-sections of the coronary artery walls, however with substantially higher resolution [154]. Intensive research aims at the detection and classification of vulnerable atherosclerotic plaques that can lead to myocardial infarctions [11, 155–159]. The major clinical application of intravascular OCT is currently monitoring and follow-up for percutaneous coronary interventions [160], especially for the deployment of coronary stents (Fig. 2.4, right) [161–165].

From its onset, the potential of OCT as instrument for *dermatology* was investigated, and it appeared promising for examination skin abnormalities that are difficult to assess by visual inspection. Hence, most

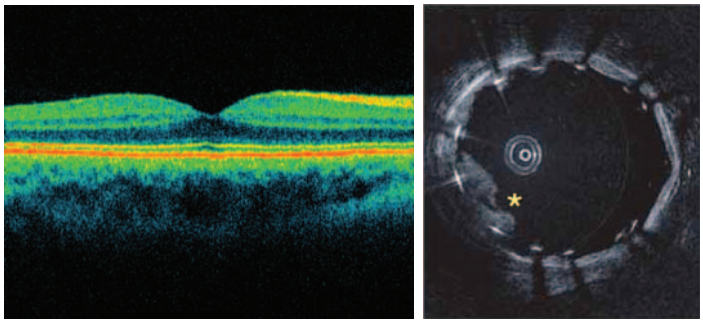

Figure 2.4.: Left: OCT image of the fovea at the center of a healthy human retina [1]. Right: OCT image of a stented porcine coronary artery with a tissue prolapse between the stent struts (asterisk) [153].

research has focused on non-melanoma skin cancer (NMSC). In NMSC diagnosis, OCT can potentially reduce the number of invasive skin biopsies, assist in finding an optimal location for a biopsy or measure tumor thickness [166]. However, despite many promising initial results in research, OCT has not yet been established in clinical dermatology. Although it can visualize changes in the skin morphology occurring in NMSC lesions [167–169], the reliable discrimination of malignant lesions from benign ones is considerably more challenging [13, 170, 171].

OCT also has the potential for numerous other applications in both medical research and in the clinical environment. It is promising for cancer diagnosis, especially as an alternative to excisional biopsies [172,173]. In conjunction with endoscopy, OCT can access hollow organs like the gastrointestinal tract [14–16], the bronchi [17] and the urinary bladder [18]. Subcutaneous imaging needles [174–176] and forward imaging probes [177–179] enable minimally invasive examination in many areas. OCT may also become a modality for surgery guidance, e. g. for the intra-operative identification of metastatic lymph nodes in breast can-

cer patients [180, 181] in order to reduce the number of unnecessary resections.

In addition to the various medical applications, OCT has become an established technique for studying small-animal models in *developmental biology* [19]. It has, for example, been used for anatomical and functional imaging of the developing cardiovascular system in different species, such as frog tadpoles [182,183], avian embryos [184–187], and mouse embryos [188]. These studies aim for better understanding of the cause of heart malformations, which are the leading cause of birth defect-related deaths in humans.

Although the majority of applications for OCT are in the biomedical field, it is also being used for many other purposes [20]. To name a few examples, OCT can perform precise characterization of surface profiles and measure the thickness and refractive index in thin-film structures. It enables non-destructive sub-surface examination of various materials and monitoring of processes in microfluidic systems. Furthermore, OCT proved a valuable tool for archeology and arts conservation [189].

2.2. Swept sources

Swept source OCT (SS-OCT) requires a highly specialized light source. This section provides a discussion of the key characteristics for high-performance swept sources (Sec. 2.2.1). It introduces the typical swept source implementations along with alternative approaches (Sec. 2.2.2), and it explains the important methods for data processing and light source characterization (Sec. 2.2.3). This also includes a description of the type of swept source that we are working with and of our methods for the performance characterization.

2.2.1. Figures of merit

Every light source for OCT must span a broad *spectral bandwidth* in order to enable a high axial resolution (Eq. 2.7). In case of a swept

source, this corresponds to the tuning range or *sweep range*. Often, the FWHM of the spectral envelope, I_{src}, is stated as the bandwidth, although it has little value for comparing light sources with spectra of different shape. In this thesis, the term bandwidth always refers to the total spectral range where frequency-swept narrowband light is emitted. Current broadband swept sources for the 1060 nm range can have a bandwidth wider than 110 nm [47, 190].

However, not only the bandwidth is important, but also the *spectral shape*. The point spread function (PSF)—given by the Fourier transform of I_{src} (Eq. 2.2, Eq. 2.6)—should preferably have low side-lobes, since these limit the dynamic range. For a given total bandwidth, different spectra may be used to trade-off axial resolution and dynamic range, similar to window functions in spectral analysis [191]. In TD-OCT and SD-OCT, this principle can be exploited to a limited extent by numerical apodization of the recorded signals [192,193], whereas actual shaping of a broadband light source spectrum requires complex spectral filters [194]. In contrast, swept sources permit direct arbitrary spectral shaping by power regulation simultaneous with the frequency sweep [195].

Another important figure is the *sweep rate*, which determines the image acquisition speed. Unless an OCT system scans the samples with several beams simultaneously [42, 43], it performs one A-scan per frequency sweep. Commercial swept sources with 100 kHz sweep rate have recently become available, whereas a sweep rate of more than 5 MHz has been achieved with a research system [42].

The *linewidth* of most swept sources is relatively broad compared to typical lasers, usually several 10 GHz. The resulting coherence length of a few millimeters is sufficient for many biomedical applications, although some applications may require longer imaging ranges up to several 10 mm [62, 64].

Furthermore, a swept source must provide sufficient *output power* to achieve a good signal-to-noise ratio (SNR). Biological samples are normally probed with a sample beam power close to the maximum permis-

sible exposure (MPE) level. For the eye, this power level is relatively low (∼2 mW[‖]), but other tissues can tolerate higher exposure. Certain system designs can also increase the power demand, for instance an interferometer architecture that retrieves an increased proportion of the light from the sample at the expense of higher losses on the input side [73] or simultaneous scanning with multiple beams [42, 47]. Preferably, a swept source should emit several 10 mW average power for typical OCT applications.

2.2.2. Implementation

The commonly used swept sources are tunable lasers, which can perform a rapid, continuous frequency sweep. Different setups have been realized using laser crystals [37], rare-earth doped fibers [197, 198] or semiconductor optical amplifiers (SOAs) as gain medium [38]. The latter have the advantage of a very short excited-state lifetime (nanoseconds), which enables very fast tuning. Semiconductor optical amplifiers (SOAs) are very compact, efficient and easy to handle due to direct electric pumping. They feature high gain and broad bandwidth, and they are available for many wavelength ranges. Fiber-coupled SOA modules enable uncomplicated implementation of alignment-free all-fiber swept sources (Fig. 2.5 a), which have gained great popularity in the scientific environment [40, 199].

A difficulty with this type of light source arises from the polarization-dependent gain of SOAs and bend-induced birefringence in optical fibers. Wavelength-dependent rotation of the propagating light's polarization state can impair or even suppress the lasing at some wavelengths, leading to a "notched" or discontinuous light source spectrum. A polarization

[‖] The MPE is defined by the standards IEC 60825 and ANSI Z136.1. The power level depends on the exposure time, illuminated area on retina and other parameters. For wavelengths above 1000 nm, 1.5–2 mW is commonly considered safe for 10 s exposure [43, 196].

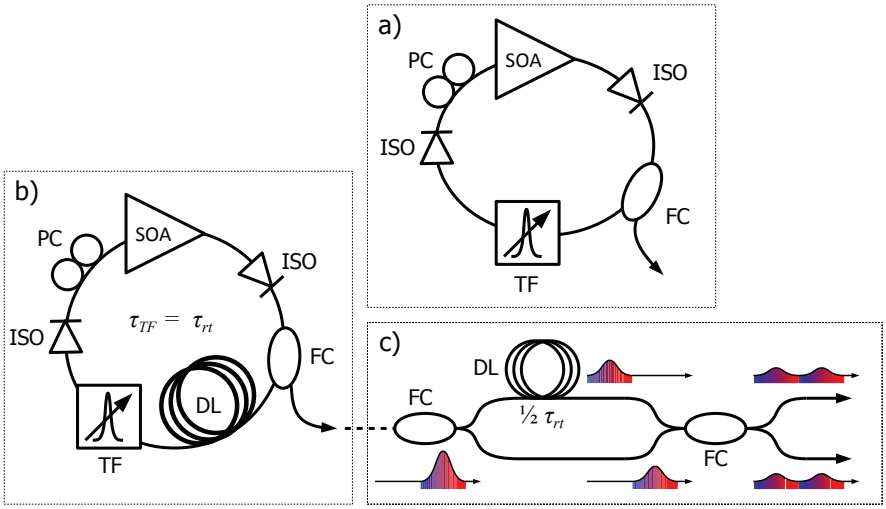

Figure 2.5.: Fiber-based swept source configurations. a: simple tunable laser, b: Fourier-domain mode-locked laser, c: optional buffering stage.

controller can to some extent compensate for this effect, but good adjustment for a broad wavelength range can be difficult, in practice.

For applications in the 1060 nm range with high power demand, the SOA can be complemented with an ytterbium-doped fiber amplifier (YDFA) [43, 46, 200]. However, the YDFA gain spectrum offers little flexibility and can limit the bandwidth of the light source [200]. Furthermore, one must take care of the hazard of self-pulsing [201] to ensure patient safety and to avoid hardware damage.

Another key component of a swept source is a rapidly tunable filter that selects which optical frequencies are amplified in the resonator. Two approaches have found wide-spread application. One utilizes a diffraction grating in conjunction with different kinds of beam deflectors, such as galvanometer-mounted mirrors [38], rotating polygon mir-

rors [202, 203], or mirrors actuated by micro-electro-mechanical systems (MEMS) [204]. Also electro-optic [205] and acousto-optic [206] deflectors have been investigated, but have until now not shown sufficient performance. Similarly, Fabry-Perot filters tuned by piezo- or MEMS-actuators offer a broad tuning range and a sufficiently narrow linewidth [40, 190]. Fiber-based Fabry-Perot filters have proven very valuable for swept source development, since they are easy to handle and highly flexible [62, 207], and they permit very high sweep rates up to 370 kHz [208].

Fabry-Perot filters or oscillating scanning mirrors can support broadband sweeping with several 100 kHz repetition rate, but only with a bidirectional sweep (typically sinusoidal). This is a disadvantage, because the laser performance (output power and coherence) is often significantly lower for one sweep direction [40, 199, 209], due to non-linear effects in the SOA. Because the light being amplified undergoes a small negative frequency shift, the laser operates best in the sweep direction with decreasing frequency—or increasing wavelength, respectively—which is commonly termed the "forward" sweep direction [40, 199]. At high tuning speed, the backward sweep is normally useless, which reduces the light source duty cycle by 50%.

Besides the maximum frequency supported by the tunable filter, the build-up time for coherent laser light from spontaneous emission is a limitation for the sweep rate in this type of laser [199]. Up to a certain sweep rate, light at each wavelength can pass the filter transmission window for a sufficient number of round trips in the resonator saturate the gain medium. If the sweep rate is increased beyond this limit, the output power will drop. Lasing will be suppressed first at the wavelengths with lowest net gain and will ultimately cease completely. This sweep rate limit is inversely proportional to the resonator length, hence a short laser cavity enables rapid sweeping [190].

Alternatively, one can circumvent this limitation by synchronizing the filter sweep period, τ_{TF}, with the resonator round-trip time, τ_{rt}, thus

allowing the laser light to circulate without interruption. This technique, called Fourier domain mode-locking (FDML) [41], requires a very long resonator determined by the sweep rate that the tunable filter supports. This can be realized by a fiber delay line of several hundred meters to several kilometers length (Fig. 2.5 b).

A challenge in the practical implementation of Fourier domain mode-locked (FDML) lasers is chromatic dispersion in optical fibers, which prevents perfect frequency matching for the entire sweep range [45]. Laser light at wavelengths with a frequency mismatch is subject to increased loss in the tunable filter. This reduces the photon lifetime and leads to a degradation of the instantaneous coherence length [63], or even to a decreased sweep bandwidth [210]. However with adequate dispersion compensation, FDML lasers can have a very high coherence length [63, 64].

With a method called *buffering* [208], one can increase the light source sweep rate, f_{sw}, beyond the repetition rate of the tunable filter, f_{TF}. While reducing the SOA duty cycle by a factor of 2^m ($m \in \mathbb{N}$), one can split the laser output into 2^m copies and recombine them temporally delayed (Fig. 2.5 c). Thus, one can obtain a unidirectional sweep with full duty cycle at $f_{sw} = 2^m \cdot f_{TF}$ [42,43,208,211]. This, however, reduces the average output power by a factor 2^{m+1}, hence an additional booster SOA is often necessary after the last buffering stage.

All swept sources that have been reported in practical OCT applications to date are tunable lasers in one of the configurations described above. However, a number of alternative approaches have been investigated in the context of SS-OCT or are currently under development. Built from the same components as the described fiber-based lasers, a *swept amplified spontaneous emission* (ASE) *source* enables very high sweep rates without being limited by the build-up time for laser light [212]. It is, however, difficult to operate, because several tunable filters must be precisely synchronized. *Stretched pulse supercontinuum sources* can perform ultra-fast frequency-sweeps without an

active tuning mechanism [213], but have not shown sufficient SNR for OCT imaging of highly scattering samples. They can, however, be used for nanometer-precision interferometric profilometry [214]. Recently, *dispersion-tuned mode-locked lasers* have been proposed for SS-OCT, and sweep rates up to 500 kHz have been demonstrated [215, 216]. However, laser output power and bandwidth show significant degradation with increasing sweep rate.

The most promising alternative technologies are compact diode lasers with integrated tuning mechanism, for instance *MEMS-tunable vertical-cavity surface-emitting lasers* (VCSELs), which operate inherently on a single optical frequency. A VCSEL-based swept source for the 1300 nm band was recently presented, performing a continuous sweep at 760 kHz with broad bandwidth and good coherence length [217]. Monolithic *distributed Bragg reflector* (DBR) *lasers* realized at 1550 nm and 1300 nm have also shown great potential for broadband high-speed tuning [218, 219]. They permit linear frequency-sweeping at repetition rates of several hundred kilohertz and offer unprecedented flexibility for adjusting the light source characteristics to various purposes.

In this project, we explore possibilities for improving swept sources using new semiconductor gain media, while at the same time providing a prototype for subsequent OCT studies. As platform, we have chosen the fiber-ring laser architecture (Fig. 2.5 a) with a fiber-coupled Fabry-Perot tunable filter. This implementation enables uncomplicated assembly of a mechanically stable light source requiring minimal alignment. At the same time, it offers high flexibility for adapting details in the configuration and for adjusting the operating parameters. It allows hassle-free coupling to measurement setups or imaging systems via delivery fibers. Furthermore, implementing Fourier domain mode-locking (FDML) for high speed sweeping is straight-forward, simply by inserting a fiber delay line (Fig. 2.5 b).

2.2.3. Methods for data processing and signal characterization

This section describes important methods specifically related to SS-OCT. The first part explains the acquisition of spectral interferograms with linear sampling in the optical frequency domain, which is necessary for the subsequent discrete Fourier transform (DFT). The second part covers the typical measurements yielding the key characteristics of a swept source, such as the bandwidth and the spectral shape, or the performance figures for OCT imaging, namely the achievable resolution, sensitivity and sensitivity roll-off.

Signal linearization

The spectral interferograms generated in an FD-OCT system must be sampled in equal intervals in the optical frequency domain. Otherwise, the DFT yields A-scan profiles with degraded depth resolution and signal amplitude. The degradation gets worse with increasing delay between sample and the reference path. A swept source can—depending on the tunable filter in use—have a highly non-linear sweep. For instance, a Fabry-Perot filter can at high sweep frequencies only follow a sinusoidal tuning curve. Data acquisition in equal time intervals would thus lead to distorted interferograms, which must be corrected before processing.

There are different approaches for retrieving the frequency-linear signal. One can send a fraction of the light source output through an auxiliary interferometer (e. g. Fabry-Perot type) with fixed free spectral range (FSR) thereby generating pulses of light at equal frequency intervals, which can be used as clock for the analog-to-digital converter (ADC). This method requires no further signal processing before the DFT, but pulse jitter can introduce sampling errors [220], and many high-speed ADCs do not support a variable external clock. Furthermore, the fixed FSR of the auxiliary interferometer limits the spectral sampling resolution of the SS-OCT system, which in turn limits the

maximum probing depth. Alternatively, one can generate an interferogram (e. g. with a Michelson or Mach-Zehnder interferometer), calculate the full analytical signal with a Hilbert transform, and thus retrieve the phase, $\phi(t)$, of the oscillating signal:

$$\phi(t) = 2\pi\tau\nu_l(t) + \phi_0. \tag{2.9}$$

ν_l is the instantaneous frequency of the swept source and τ is the delay in the auxiliary interferometer. ϕ_0 is an unknown offset, because this method does not yield an absolute value for the optical frequency, but only its relative temporal evolution. With the corresponding value of ϕ assigned to each data point, one can now interpolate the signal (e. g. with cubic splines or with a polynomial) and resample it in equal ϕ-intervals.

If the light source sweep is sufficiently stable, one can record the calibration curve, $\phi(t)$, only once in a while instead of simultaneously to every A-scan. One can then use the OCT interferometer for this purpose, e. g. by flipping a mirror into the sample arm or by installing an additional auxiliary reference arm [43].

Swept source characterization

A number of measurements are typical for determining the performance of a swept source.

With an optical spectrum analyzer (OSA), one can visualize the absolute sweep range on the wavelength scale. However, the information contained in such a spectrum has otherwise rather little significance. A non-linear sweep of the light source leads to a distorted spectrum, because an OSA integrates the power spectral density over time. For instance, for sinusoidally sweeping light sources, "horn"-like artifacts appear at one or both ends of the sweep range if the sweep turning points are within the gain spectrum. Furthermore, the OSA integrates over both sweep directions and can hence not show the asymmetry in

performance. By contrast, the instantaneous output power, $I_{src}(\nu_l(t))$, monitored with a fast photodetector reveals directly the actual spectral shape for both sweep directions and the stability of the output power from sweep to sweep.

Typically, we use an OSA to visualize the laser emission relative to the ASE background, and to measure the absolute sweep range. During sweep operation, we monitor the instantaneous output power with an oscilloscope, which provides in real time all information necessary for adjusting the control parameters (SOA current, filter tuning voltage, polarization controller setting).

An important part of the characterization is the generation of PSFs with a simple interferometer (typically Michelson or Mach-Zehnder). Plotted as function of the coordinate $z = c\tau/2$, the FWHM of the PSF peak yields the achievable axial resolution in air. The height of the peaks for increasing delay, τ (or z, respectively), reveals the sensitivity roll-off. Commonly, one plots $20\log_{10}$ of the linear signal. The PSF amplitude represents then the relative reflectivity of the sample in dB.

For the PSFs, we generate interferograms with a fiber-based Mach-Zehnder interferometer (MZI) with dual balanced detection. In both interferometer arms, the light propagates a variable distance in air between two fiber collimators. For a roll-off measurement series, we record one phase curve in the same interferometer with short or medium delay, and use it to linearize the interferograms we acquire subsequently.

To determine the sensitivity, one decreases the interferometer delay almost to zero and attenuates the sample beam until the PSF peak is just visible above the noise floor. The sensitivity is then the sum of the signal-to-noise ratio (SNR) (on the $20\log_{10}$ scale) and the attenuation. If the loss in the sample arm optics is known, one can include it in the attenuation and thus calculate the theoretical maximum sensitivity achievable with the light source. The sensitivity scales with the incident power on the sample, hence this value must always be stated, as well. Different definitions of the noise level, e. g. the standard deviation [199,

221] or the root mean square value [222] of the noise in a certain z-range, can also lead values differing by several decibels.

We perform the sensitivity measurements either using the MZI or prior to OCT imaging by inserting a mirror into the sample arm of the imaging interferometer. The latter method provides a measure for the total system performance under the particular operating conditions. To determine the SNR, we record the standard deviation of the noise floor in a range around the signal peak while the sample arm is blocked.

3. High-power swept source

SOAs for the 1060 nm range provide significantly lower output power than those for the telecommunication bands around 1300 nm or 1550 nm. During the past few years, new semiconductor gain chips with saturated output power approaching 100 mW became available, but the risk of optical damage to the anti-reflection coated crystal facet limits the average output of fiber-coupled SOA-modules to 20–30 mW. Depending on the laser output coupling ratio and the need for optical isolators, the net laser output may then be limited to 10–15 mW. This is sufficient for simple ophthalmic SS-OCT applications, because for the eye, the maximum permissible exposure (MPE) is about 2 mW in the 1060 nm range (see note in Sec. 2.2.1). However, with continuing development, new configurations with higher power demand emerge, e. g. ultra-high speed swept sources with multiple buffering stages [43], or interferometers optimizing the light retrieval from the sample at the expense of higher losses on the input side [73]. There are also applications not related to OCT requiring swept sources with higher power, for instance pumping of optical parametric oscillators for mid-infrared spectroscopy [223, 224].

The power limitation can be overcome by using a special type of semiconductor gain element, a so-called tapered amplifier (TA), which feature high saturation power and a broad output facet and can thus emit up to several watts of light [225]. Previously, Adhimoolam and Groß et al. demonstrated wavelength-swept lasers based on TAs in free-space ring resonators with sweep rates up to 1 kHz [223, 224].

We have integrated a broadband TA into a fiber-based swept source and prove its feasibility for high-speed FDML operation and OCT imag-

ing. We use the TA permitting high output power levels in conjunction with an additional conventional SOA that provides large small-signal gain. In contrast to other light sources with equal gain media in series [226–228], our configuration benefits from the complementary characteristics of the two amplifiers. Hence, we achieve stable FDML operation with high output power, and can exploit the full gain bandwidth even under non-ideal conditions, such as high loss or dispersion in the laser resonator.

Furthermore, we investigate the influence of chromatic dispersion by comparing the FDML performance with two different fibers as delay line: a conventional single-mode fiber and a low-dispersion photonic crystal fiber (PCF). With the PCF, the effects of dispersion are significantly reduced, but its high insertion loss leads to lower overall performance in comparison to the standard fiber. In both configurations, the additional gain provided by the SOA is crucial for good performance. Not only does it compensate for intrinsic losses, it also helps to overcome the bandwidth-limiting effects of dispersion in the standard fiber.

Although our prototype light source leaves room for optimization, it brings important insights for future swept source development. Firstly, TA technology is suitable for generating high output power with semiconductor gain media. Secondly, high gain is important for good performance of an FDML swept source, especially when the resonator exhibits strong chromatic dispersion.

This chapter presents the implementation of the high-power swept source (Sec. 3.1), a detailed characterization (Sec. 3.2.1) and first OCT images (Sec. 3.2.2). Furthermore, it explains subsequent modifications to the initial setup and the resulting changes in the performance (Sec. 3.2.3). The chapter concludes with a discussion of the results within the context of continuing swept source development (Sec. 3.3).

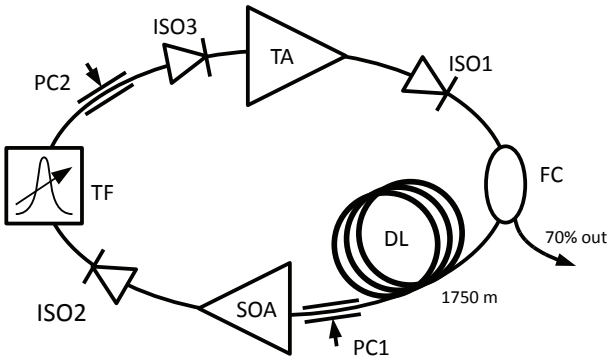

Figure 3.1.: Setup of the high-power swept source. TA: tapered amplifier including fiber-coupling optics, SOA: semiconductor optical amplifier, TF: tunable filter, DL: delay line, FC: fiber coupler, ISO: optical isolator, PC polarization controller.

3.1. Implementation

The key component in our light source setup (Fig. 3.1) is the tapered amplifier (TA) (Ferdinand-Braun-Institut, Leibniz-Institut für Höchstfrequenztechnik). Its output is focused into a single-mode fiber and passes an optical isolator for suppression of backreflections, which could damage the TA. A fiber coupler directs 70% of the light out of the cavity and the remaining 30% into a delay line (1.75 km optical fiber). An SOA (InPhenix) amplifies the light before it passes a fiber-coupled Fabry-Perot tunable filter (Micron Optics), which selects a narrow wavelength band (150 pm FWHM) that is fed back to the TA. Further optical isolators before and after the filter ensure unidirectional lasing in the resonator and suppress backreflections from the Fabry-Perot cavity. Polarization controllers in the cavity adjust the polarization state of the light at the amplifier inputs to match the axis of maximum gain.

3.1.1. Tapered amplifier

A tapered amplifier (TA) is a special type of SOA with a two-sectioned waveguide architecture combining the power handling capability of a broad-area diode laser with the good beam quality of a single-mode SOA. It has a narrow ridge waveguide on the input side, which supports only the fundamental transverse mode of the light field. This is followed by the gain-guided tapered section where the mode field slowly broadens while maintaining its original single-mode profile. A relatively low confinement factor leads to high saturation power, and the broad output facet can tolerate high power levels without taking damage. TAs can therefore generate up to several watts of light, but still emit a beam of high quality, suitable for efficient coupling to single-mode fibers.

We use a new broadband TA (Ferdinand-Braun-Institut) with 50 nm ASE bandwidth (FWHM, peak at 1060 nm) at 2.5 A pump current. It features a single-quantum-well structure with a 1 mm long ridge-waveguide section and a 3 mm long tapered section with 4° full taper

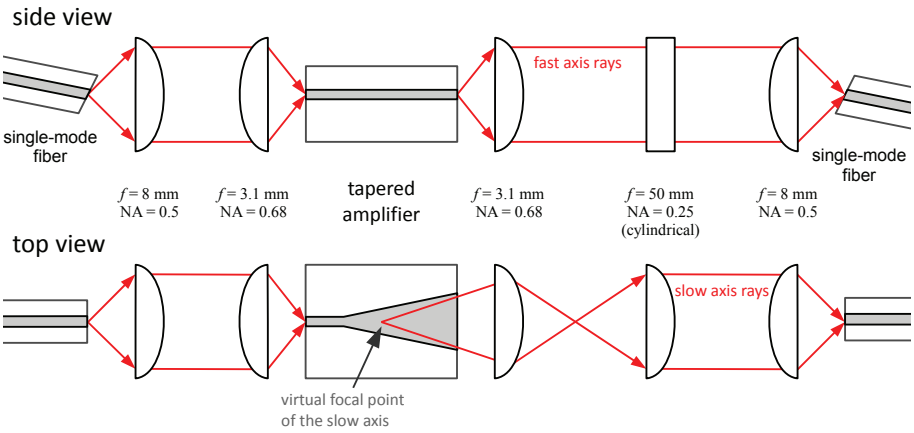

Figure 3.2.: Fiber-coupling optics of the tapered amplifier.

angle. The output facet is hence wider than 200 µm, as compared to a few micrometers in a single-mode waveguide.

Since the TA is not available in a fiber-coupled module, we have integrated it into the FDML resonator with free-space optics (Fig. 3.2). We collimate the astigmatic output beam with an aspheric lens and a cylindrical lens, and focus it then to the core of an angle-polished single-mode fiber. On the input side, a pair of aspheric lenses collimates the beam emerging from the resonator fiber and focuses it to the ridge waveguide of the TA.

The fiber-coupling efficiency on the output side of a TA depends typically on the pump current and the emitted power. In a laser resonator with a current below threshold, the TA emits mostly ASE, of which only a small fraction is coupled into the single-mode fiber due to low beam quality. The coupling ratio improves as the current rises towards the laser threshold. At high currents, the beam quality degrades again, and correspondingly also the coupling ratio [229]. In our setup, we can couple up to 40% of the TA output into a single-mode fiber.

3.1.2. Serial amplifier architecture

High gain per resonator round trip is essential for good FDML performance. FDML resonators exhibit often high losses due to various fiber-optical components (e. g. isolators) and due to the frequency mismatch caused by chromatic dispersion in the delay line [210]. Whereas a TA can generate very high output power, it has lower small-signal gain than a conventional SOA due to its lower confinement factor. With a moderate current ($I_{TA} = 2.5\,\mathrm{A}$) the fiber-coupled TA unit has a small-signal gain of about 15 dB, as compared to a typical SOA with 20 dB or more. Using only the TA as solitary gain medium yields poor FDML performance. The laser output fluctuates from sweep to sweep and exhibits strong relative intensity noise, whereas the total sweep bandwidth hardly exceeds 40 nm. Increasing the pump current up to 5 A leads only to slightly higher average power, and it does not reduce the fluctuations or the

noise. Presumably, the power-dependent coupling efficiency results in non-linear feedback, which makes this laser configuration susceptible to any kind of power fluctuations.

High gain provided by multiple amplifiers in series can improve the overall performance of a swept source [226]. Hence, we have added a conventional SOA (InPhenix IPSAD1001–4113), which acts similar to a pre-amplifier. In addition to increasing the small-signal gain, it plays a stabilizing role. On the one hand, the spontaneous emission transmitted from the SOA through the tunable filter is a stable seed for the TA, independent of the varying fiber-coupling efficiency. On the other hand, saturation of the SOA gain dampens any power fluctuations originating from the TA output or the fiber-coupling optics.

3.1.3. Delay line

We use a 1.75 km long delay line resulting in a resonator round-trip frequency of approximately 116 kHz, close to a mechanical resonance of the tunable filter. We compare the light source performance with two different delay lines, one consisting of conventional single-mode fiber and one made of a special low-dispersion photonic crystal fiber (PCF). The single-mode fiber (Corning HI 1060) has low insertion loss, around 2 dB, but introduces a significant amount of chromatic dispersion. The longest and the shortest round-trip time in the range of interest (1030 nm to 1100 nm) differ by approximately 4.5 ns. For the PCF (NKT Photonics SC–5.0–1040, designed for zero dispersion at 1040 nm), we estimated 0.9 ns as the maximum mismatch of round-trip times within the same range. The insertion loss of the PCF is significantly higher, around 10 dB. It originates partly from inherent attenuation ($\sim$3.8 dB/km according to the manufacturer test data) and partly from several splices between the PCF, a length of HI 1060 fiber on each side for connecting to the resonator components, and a mode-field adapting intermediate fiber.

3.2. Performance

3.2.1. Characterization of the initial setup

With the HI 1060 delay line, the light source supports FDML operation with maximal sweep bandwidth when the tunable filter frequency, f_{TF}, is between 116.78 kHz and 116.86 kHz. Due to chromatic dispersion, the resonator round-trip frequency, f_{rt}, varies considerably within the bandwidth of the laser, so that the FDML operating frequency is not as clearly defined as for a laser in the 1300 nm band.

The instantaneous output power (Fig. 3.3 a) shows a strong asymmetry between the forward sweep (from short to long wavelengths) and the backward sweep. When f_{TF} is tuned to the maximum round-trip frequency within the sweep spectrum, $f_{rt,max}$, the light source runs stable with high output power during the forward sweep, while the backward sweep power decreases severely and is subject to strong amplitude fluctuations. If $f_{TF} = f_{rt,min}$, the performance degrades only during the forward sweep, and if $f_{rt,min} < f_{TF} < f_{rt,max}$, both sweep directions are partially affected.

This phenomenon can be explained as a combined effect of chromatic dispersion in the delay line and frequency down-conversion due to nonlinear processes in the semiconductor amplifiers [209]. Because of the frequency shift, positive detuning of an FDML laser ($f_{TF} > f_{rt}$) affects the backward sweep significantly stronger than the forward sweep [230], and vice versa with negative detuning ($f_{TF} < f_{rt}$). If $f_{TF} = f_{rt,max}$, the laser is positively detuned in the entire sweep range, and the performance degrades mostly during the backward sweep. Correspondingly, if $f_{TF} = f_{rt,min}$, only the forward sweep is severely affected. As a result, only one sweep direction appears useful for OCT imaging. In terms of power and stability, the light source performs best when it is tuned for optimal forward sweep operation.

The average output power is 20–25 mW with $f_{TF} = 116.853$ kHz and pump currents $I_{TA} = 2.3$ A and $I_{SOA} = 300$ mA. The average power dur-

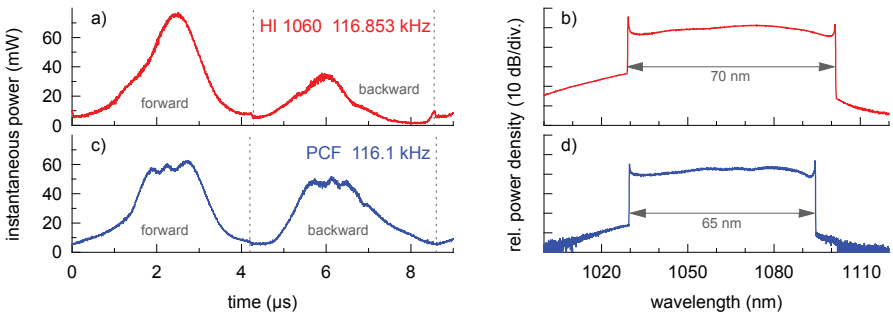

Figure 3.3.: The instantaneous output power of the light source is high (a, c), but there is a strong asymmetry between forward and backward sweep. The asymmetry is lower with the PCF-delay line. The HI 1060 delay line permits a slightly higher total sweep range than the PCF (b, d).

ing the forward sweep, which would be used for imaging, is approximately 30–35 mW. These power levels are sufficient for most ophthalmic OCT applications. Even if one buffers the forward sweep in order to double the A-scan rate, one has two outputs with at least 7 mW each to work with.

These output power levels are, however, lower than expected. In a simple free-space resonator, the same TA can emit several hundred milliwatts with 1–2 A pump current, and in general such devices can generate several watts of laser light [21, 28]. Apparently, the feedback in the current fiber-optic configuration is not sufficient for saturating the gain of the TA. The SOA, on the other hand, operates in the saturation regime and limits thereby the feedback to the TA. In conjunction with losses caused by the fiber-coupling optics, the isolators, and the tunable filter, this leads to the comparably low output.

The total sweep range is 70 nm (Fig. 3.3 b), and the FWHM after linearization in the optical frequency domain is 11.5 THz (∼42 nm). This

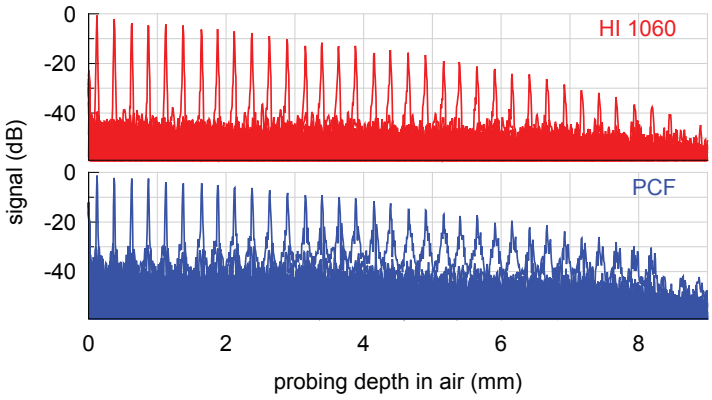

Figure 3.4.: The plotted point spread functions (forward sweep) reveal a better overall performance with the HI-1060 delay line (top). With the PCF (bottom), the signal roll-off is slightly slower, but the noise floor is higher and the peaks have larger side lobes.

corresponds well with the tuning range of the TA during preliminary tests. Obviously, this FDML laser configuration exploits the gain bandwidth of the TA very well, even though the resonator is subject to high chromatic dispersion.

With the PCF delay line, the sweep frequency range for FDML operation is narrower, from 116.085 kHz to 116.1 kHz, and the asymmetry in the transient output power (Fig. 3.3 c) is significantly lower, both due to lower dispersion. Still, one sweep direction is subject to strong power fluctuations and does not appear useful for OCT. Furthermore, the polarization rotation in the PCF is apparently significantly faster than in the single-mode fiber. We cannot completely eliminate all artifacts (notches in the spectrum) by adjusting the polarization controllers. For $f_{TF} = 116.1\,\mathrm{kHz}$ and the same pump currents as above, the forward sweep is stable and has an average power around 30 mW. The total

sweep range is 65 nm (Fig. 3.3 d) and the FWHM roughly 42 nm.

The characteristics of both configurations are remarkably similar because of common limiting factors. The saturation power of the SOA limits the output power of the light source, whereas the gain bandwidth of the TA limits the sweep bandwidth. Regarding the effects of dispersion, the PCF-configuration is clearly closer to the ideal case, where both sweep directions exhibit symmetric output power. But due to the very high insertion loss, it does not improve the overall performance in this light source setup.

With both delay lines, we achieve point spread functions (PSFs) with 15 µm FWHM. This enables ∼11 µm axial resolution in tissue, which is adequate for OCT imaging. The sensitivity roll-off is also similar for both fibers (Fig. 3.4). An exponential fit to the PSF peaks for $z \leq 6\,\mathrm{mm}$ yields 3.4 dB/mm roll-off with the HI-1060 delay line (6 dB at $z \approx 1.8\,\mathrm{mm}$) and 3.1 dB/mm with the PCF (6 dB at $z \approx 1.9\,\mathrm{mm}$). Besides the slightly better roll-off, the PSFs exhibit higher side lobes and a higher noise floor in the PCF configuration.

3.2.2. Imaging

Due to the better overall performance, we use the the HI 1060 delay line for acquiring OCT images. In this configuration, the shot noise limited sensitivity is 110 dB with 10 mW sample arm power (corrected for interferometer coupling losses). By imaging slices of cucumber and of human skin in vivo (Fig. 3.5), we demonstrate the OCT capability of this light source configuration. The images consist of 1200 A-scans acquired during the forward sweep. The cucumber images visualize clearly the cellular structure, and show a penetration depth of more than 1.5 mm into the water-rich tissue. Averaging over a number of B-scans can significantly reduce the noise, as the qualitative comparison of a single frame (Fig. 3.5 a) and a moving average over 10 B-scans (Fig. 3.5 b) reveals. This shows the potential for exploiting the high data acquisition rate to improve the image quality. For the skin images, an average over

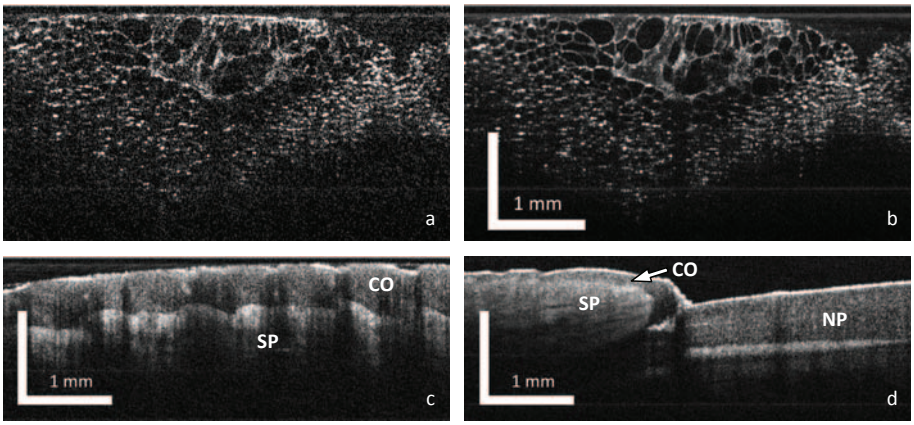

Figure 3.5.: OCT images of a slice of cucumber show deep penetration ($> 1.5\,\mathrm{mm}$) into the water-rich tissue (a: single frame, b: 10 frames averaged; scale bar assuming $n = 1.33$). In vivo OCT images of skin at the finger tip (c) and of the nail fold region (d) show clearly the stratum corneum (CO) and the border to the stratum spinosum (SP), as well as a cross-section through the nail-plate (NP). (3 frames averaged, scale bar assuming $n = 1.4$).
Acquired by W. Wieser (LMU). Sample power: 2.5 mW; data acquisition: 12 bit, 400 Msamples/s, 200 MHz analog bandwidth.

3 frames yields adequate noise reduction. Clearly visible features are the border between the thick stratum corneum and the lower parts of the epidermis at the finger tip (Fig. 3.5 c), as well as the cross-section through the nail-plate and the epidermis structure adjacent to the nail fold (Fig. 3.5 d). As these images confirm, the light source is feasible for high-speed OCT imaging.

3.2.3. Subsequent modifications

A newer SOA model (InPhenix IPSAD1001C–5113) that has become available after the initial characterization provides higher gain and saturation power. It improves the feedback to the TA, thus increasing the output power (Fig. 3.6) as well as broadening the achievable sweep bandwidth. With $I_{TA} = 2.3\,\mathrm{A}$, the light source emits ∼33 mW—as compared to previously 25 mW—with a continuous sweep over 80 nm. By increasing the current to 4 A, we can generate more than 50 mW average power (Fig. 3.6 b).

Even higher output power at lower currents is possible, if we interchange the positions of the SOA and the tunable filter in the resonator (e. g. ∼40 mW average power with $I_{TA} = 1.5\,\mathrm{A}$ and $I_{SOA} = 150\,\mathrm{mA}$). This leads also to completely symmetric instantaneous power in both sweep directions (Fig. 3.7 a). However, the useful sweep range is then limited to about 60 nm. When the tunable filter sweeps to the very edges of the laser gain spectrum, the output power is dominated by spontaneous emission from the SOA amplified by the TA. In the time-averaged spectrum (Fig. 3.7 b), this appears as a series of fluctuating laser lines with approximately 400 GHz mode-spacing in the range of maximum gain. It is still not clear what leads to the development of pronounced modes instead of homogeneous broadband amplification. Judging by the mode-spacing, there might be a weakly resonating structure of approximately 100 µm length in the amplifier waveguide. Although this configuration is interesting for generating high power, it seems not optimal for OCT in terms of the bandwidth. Hence for OCT imaging, we use the light source in its initial setup (Fig. 3.1).

Another model of Fabry-Perot filter (Lambdaquest) permits a tuning frequency of 175 kHz and exhibits less thermal drift. We use it in conjunction with a delay line made of 1155 m standard fiber (Corning SMF28). This fiber is not purely single-mode in the 1060 nm range, but it functions sufficiently well, as Klein et al. previously demonstrated [43], and is considerably less expensive than HI 1060 fiber. With a buffering

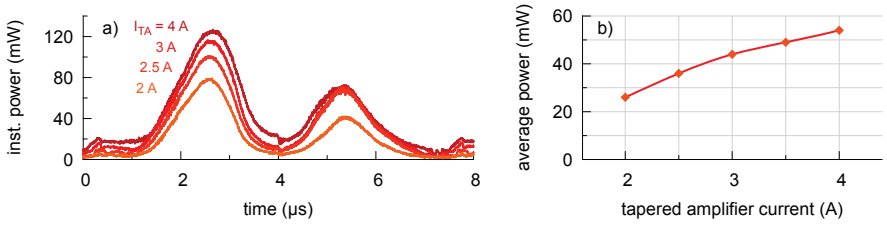

Figure 3.6.: Instantaneous output power (a) and average power (b) with a newer SOA. The light source shows good performance if $I_{TA} \geq 2\,\mathrm{A}$, and can provide abundant power for OCT applications.

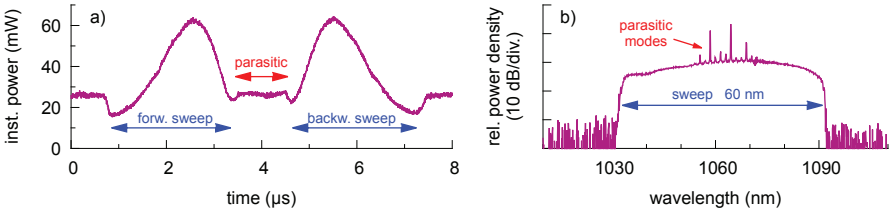

Figure 3.7.: With the SOA and the tunable filter interchanged, the instantaneous power is high and symmetric in both sweep directions (a). However, parasitic modes appear when the sweep range exceeds 60 nm (b).

stage, we can create a delayed copy of the forward sweep while suppressing lasing during the backward sweep by switching off the SOA current. In this configuration, we can achieve a sweep rate of 350 kHz and a net output power of 10 mW at $I_{TA} = 2.5$ A. With in vivo OCT images of the human retina (Ch. 6), we can prove the feasibility of this light source configuration for high-speed imaging in ophthalmologic applications.

3.3. Discussion

Tapered amplifiers (TAs) are suitable gain media for swept sources with high output power. With a new broadband TA, we have constructed a prototype FDML laser capable of generating an average output power of 30–50 mW with a sweep range of 70–80 nm, and enabling an A-scan rate up to 350 kHz. The laser is implemented in a dual-amplifier configuration with the TA generating abundant output power and an auxiliary SOA providing sufficient gain. Hence, we can exploit the full gain bandwidth in spite of losses and dispersion in the resonator.

The test of a low dispersion PCF delay line in this prototype has not yielded conclusive results. The effects of dispersion are clearly weaker with the PCF in use in comparison to a conventional single-mode fiber, but the overall performance does not improve due to significantly higher insertion loss. Originally, we assumed that the PCF might be of advantage in conjunction with a faster tunable filter that would permit to use a shorter delay line. However, a later experiment with a high-speed filter has not been successful either (Ap. A).

Subsequent to our demonstration, a similar light source has been developed at Ludwig-Maximilians-Universität (LMU) employing an ytterbium-doped fiber amplifier (YDFA) [43] instead of a TA. Both concepts have advantages and drawbacks. A YDFA can provide high gain and high power and can be assembled from readily available fiber components. With the peak gain around 1030 nm [231], it can complement the spectrum of an SOA [46], but it may also limit the bandwidth of a

broadband light source [47]. Generally, the possibilities for modifying the YDFA gain spectrum are very limited, and the concept cannot be easily transferred to other wavelength ranges. Furthermore, the feasibility of an FDML laser using only a YDFA without an additional SOA seems doubtful, as this configuration has until now not shown convincing performance [200]. Another serious drawback of the YDFA is the hazard of self-pulsing [201], which must be taken care of in order to ensure patient safety and to avoid damage to the optical setup.

A TA module optimized for SS-OCT requires further development, as described above, but it would make the setup simpler and potentially more efficient due to direct electrical pumping. It could also benefit from the general advantages of semiconductor gain media, namely unsurpassed flexibility for tailoring the gain spectrum or adjusting small-signal gain and saturation power. And due to the short excited state life time in semiconductors, there is no self-pulsing hazard. Importantly for swept source development in general, the tapered waveguide concept can just as well be applied in other spectral ranges where no suitable doped fibers are available.

The TA we use is not specifically designed for OCT. As the experiments have shown, it is feasible, but further development is necessary in order apply it in a swept source for clinical OCT applications. Primarily, compact fiber-coupled modules providing stable optimized feedback are needed [229]. With improved feedback, the TA can generate significantly higher output power than we could demonstrate in our setup. However, since OCT does not require watts of power, a modified amplifier design with higher small-signal gain at the expense of reduced maximum power might be better suited. It could even yield good performance without an auxiliary SOA. Furthermore, broadening the gain bandwidth by using similar quantum-well structures like those in broadband SOAs would be advantageous for OCT applications.

Besides setting up a working light source prototype, we have gained important insights for future swept source development. Firstly, tapered

amplifier technology is feasible for implementing semiconductor-based swept sources with high output power. It is applicable to different kinds of semiconductor gain elements and offers thus the full flexibility for tailoring the gain spectrum or choosing the operating wavelength range. Secondly, high gain is crucial for good performance of swept sources, especially FDML lasers. It does not only compensate for intrinsic losses of the optical components, it also counteracts the bandwidth limiting effects of chromatic dispersion in FDML resonators. Specialized semiconductor gain media developed according to these principles could pave the way towards the next generation of high-power broadband and high-speed swept sources.

4. Broadband swept source

The interest in resolving ever smaller details drives the development of light sources with increasing spectral bandwidth. Whereas TD-OCT and SD-OCT can benefit from multiplexed SLDs, short-pulse lasers or supercontinuum sources [32, 73], the matter becomes considerably more challenging in SS-OCT, due to the need for suitable broadband laser gain media.

During the past few years, swept sources for the 1060 nm band with more than 110 nm sweep range have become available [47, 190]. These, however, are based on short free-space resonators, hence their tuning speed is ultimately limited by the build-up time of laser light [199]. A sweep rate of 100 kHz, as recently demonstrated [190], approaches the limit of feasibility, because an external resonator with fixed length cannot become arbitrarily short. At a certain point, the resonator mode-spacing becomes so large that the laser starts mode-hopping. With an FDML laser that overcomes this speed limitation, the achievable bandwidth is usually lower. A fiber-based ring resonator exhibits higher losses than a free-space setup, hence high gain covering the entire range is required.

Typical SOAs for the 1060 nm band could until a few years ago support sweep ranges of 70–80 nm in fiber-based resonators. In order to extend the bandwidth beyond that of a single SOA, we investigated gain-multiplexing, i. e. the application of two SOAs with shifted gain spectra in parallel, as it was previously demonstrated in the 1300 nm range [232]. As our test results show, the principle can also be applied at 1060 nm, but it is hardly feasible for our practical application (details

in Ap. B).

Recently, new SOAs have become available with a gain bandwidth spanning most of the low water absorption range around 1060 nm. Using such a broadband SOA, we have constructed an FDML laser that supports a sweep range up to 100 nm. With constant pump current we achieve an axial resolution of 12 µm in air, and by shaping the spectrum with current modulation we can improve the resolution to 9 µm in air (∼6.5 µm in tissue). The spectrum coincides perfectly with the water absorption minimum, hence there is no significant degradation of the axial resolution due to the surrounding absorption bands. With equal power in both sweep directions, we can utilize the full sweep rate of 350 kHz without buffering the light source output. In order to ensure stable operation during the measurement period, we implemented automatic control of the tunable filter. Hence, we can demonstrate a high-speed swept source yielding high axial resolution in a simple and robust all-fiber configuration.

The following sections give a description of the light source implementation (Sec. 4.1), present the characterization and the performance tests (Sec. 4.2), and discuss the results in the context of broadband swept source development (Sec. 4.3).

4.1. Implementation

This section provides a description of the optical setup of the laser and the circuitry for control and monitoring (Sec. 4.1.1), and it explains the software algorithms used for spectral shaping (Sec. 4.1.2) and for the automatic tunable filter control (Sec. 4.1.3).

4.1.1. Laser resonator and control circuitry

The swept source setup is a standard FDML ring-resonator (Fig. 4.1), comprising a single SOA (Exalos ESO330004), a Fabry-Perot tunable filter (Lambdaquest) with 180 pm linewidth (FWHM), and a 1155 m long

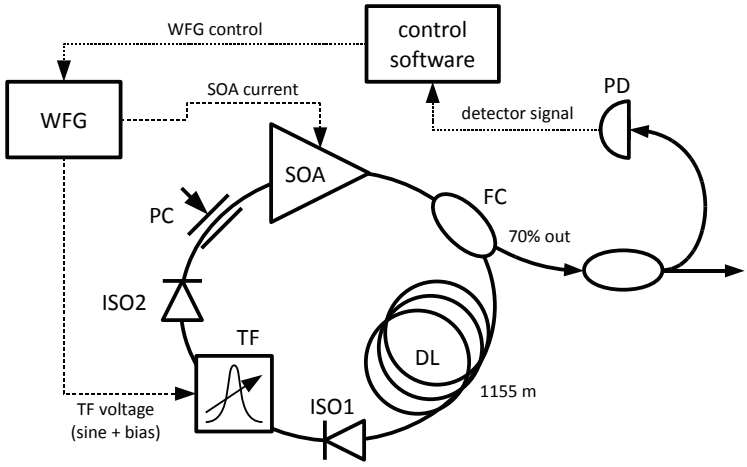

Figure 4.1.: Setup of the broadband swept source with control circuitry. SOA: semiconductor optical amplifier, TF: tunable filter, DL: delay line, FC: fiber coupler, ISO: optical isolator, PC polarization controller, WFG: waveform generator, PD: photodetector.

delay line made of standard single-mode fiber (Corning SMF28). The resulting resonator round-trip frequency matches the maximum feasible operating frequency of the tunable filter, 175 kHz. Broadband isolators ensure unidirectional lasing, and a polarization controller corrects for polarization rotation in the fibers. 70% of the light are coupled out of the resonator. For the initial performance characterization, we extract the light directly after the SOA, in order to monitor its output power directly. If the swept source is used with an interferometer causing strong backreflections, one isolator (ISO1) can be moved between the SOA and the output coupler. This does not affect the laser operation but reduces the output power by approximately 2 dB.

We operate the SOA with a special diode driver (Wieserlabs WL-

LDC 10D) that permits modulation of the pump current with 15 MHz analog bandwidth. The tunable filter drive signal (sine wave and bias) as well as the current modulation waveform are synthesized by an arbitrary waveform generator (Thurlby Thandar Instruments TGA12104) controlled by a computer. The computer receives the signal from a 125 MHz photodetector, which monitors the instantaneous output power of the light source. In a LabView program running on the computer, we have integrated full control over the tunable filter and the SOA current, power monitoring, spectral shaping and automatic filter bias correction.

4.1.2. Spectral shaping

With constant pump current, the spectrum of an SOA-based swept source exhibits typically a high peak on the long-wavelength side and a flat tail towards the short wavelengths. Whereas this tail can cover a considerable part of the total sweep range, it does not significantly improve the axial resolution. Modulation of the pump current synchronously with the wavelength-sweep permits a broader distribution of the power, which can improve the axial resolution for a given sweep range.

An iterative algorithm originally developed by Biedermann et al. [195] (LMU) computes the current waveform for a desired spectral shape. It receives the photodetector signal as input data, and it can upload waveform data for the current modulation to the waveform generator. Starting with constant current, the algorithm compares the photodetector signal with the target shape and adjusts the modulation waveform accordingly. This step is repeated until the integrated difference between actual shape and target shape falls below a preset threshold. With appropriate settings, the algorithm needs 5 to 10 iterations each taking a few seconds.

An addition to the original algorithm is an estimation of the light source output power from the detector signal. This gives us better control of the resulting power level and enables monitoring by the control software, which can switch off the SOA current when critical peak or av-

erage power thresholds are exceeded. Furthermore, we added the option to use an interferogram envelope as signal to be optimized instead of the photodetector signal. Thus, we can for instance obtain a spectral shape that compensates for wavelength-dependent losses in an OCT imaging setup or in a water cell that mimics the ocular absorption spectrum.

4.1.3. Tunable filter bias control

The piezo-actuated Fabry-Perot filter can exhibit considerable drift as a result of changing ambient temperature and warming up during high-speed sweep operation. For a number of reasons, this is detrimental for the practical application in SS-OCT. The filter sweep range should match the laser gain bandwidth in order to achieve the widest possible sweep with continuous lasing. Filter drift would cause a mismatch, leading to a narrowing of the laser bandwidth. It can also introduce an error in the interferogram linearization if a previously recorded phase curve is used. The effect is worst for the spectral shaping performance, which depends critically on the temporal alignment of the current modulation waveform with the sweep over the SOA gain spectrum. Already a small shift of the sweep range can lead to a distortion of the spectral shape at those points where the modulation waveform has the steepest gradients.

The drift can be compensated by adjusting the bias voltage of the tunable filter. We implemented an algorithm that performs these adjustments automatically, enabling hands-off operation of the swept source over an extended period.

Our bias control algorithm receives the instantaneous power signal from the photodetector as input data. Once we have adjusted all light source operating parameters, we store this trace as a reference, R. Subsequently, the program keeps acquiring the power signal, S, approximately 4 times per second, calculates the relative point-by-point difference and computes from those values an absolute error, E_{abs}, and a signed error, E_{sgn}:

$$E_{abs} = \frac{1}{N} \sum_i \left| \frac{R[i] - S[i]}{R[i]} \right|, \tag{4.1}$$

$$E_{sgn} = \frac{1}{N} \sum_i \frac{R[i] - S[i]}{R[i]}, \tag{4.2}$$

where N is the number of data points and i is the data point index. For an appropriately selected range of data points—we achieved good results with data from the long-wavelength end of the sweep—E_{abs} is a sensitive indicator for deviations from the reference. In addition, the sign of E_{sgn} shows, whether the filter bias needs to be corrected up or down. Once E_{abs} exceeds a tolerance threshold, the program changes the bias voltage in steps of 0.01 V into the direction determined by E_{sgn}. When it has reached the minimum value of E_{abs} it remains idle until E_{abs} runs out of tolerance again.

4.2. Performance

Even with a moderate constant pump current of 270 mA, the SOA can support continuous lasing over a sweep bandwidth up to 100 nm in the fiber-ring resonator (Fig. 4.2). The instantaneous power trace has the typical shape with a peak on the long-wavelength side and a flat tail extending to the short wavelengths (Fig. 4.3 a). The average power is 24–25 mW with $I_{SOA} = 270$ mA. After linearization, the peak has an FWHM of 15 THz (∼55 nm), and PSFs generated with this spectrum yield an axial resolution of 12 µm in air. Remarkably, the power difference between forward and backward sweep (i. e. from short to long wavelengths and vice versa) is very low. Obviously, the SOA can reach the saturation regime in both sweep directions, due to sufficiently high gain.

By modulating the SOA pump current during the sweep, we can improve the achievable axial resolution. The gain bandwidth increases

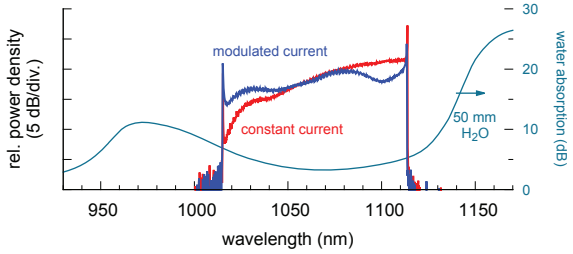

Figure 4.2.: The sweep spectrum of the broadband swept source spans up to 100 nm and coincides perfectly with the range of low water absorption.

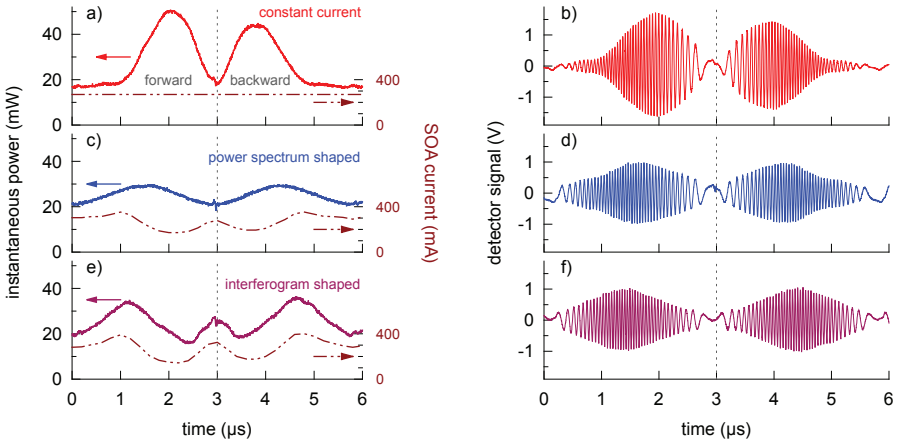

Figure 4.3.: Instantaneous output power (a, c, e) and exemplary interferograms (b, d, f) with constant or modulated SOA current.

with the pump current. However, above 270–300 mA, the output power can easily reach critical levels (> 40 mW average power from the SOA fiber) that can cause damage to the SOA. In order to avoid that, we

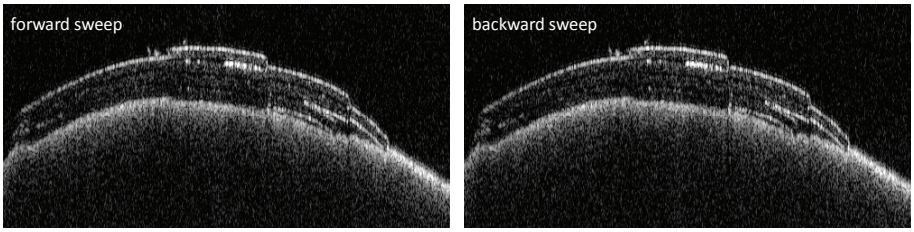

Figure 4.4.: An OCT B-scan of 3 adhesive tape layers on paper split into two images (consisting of either forward sweep A-scans or backward sweep A-scans only) does not exhibit an apparent difference in image quality between the two sweep directions. Acquired by T. Torzicky (MUW).

apply lower current while the tunable filter sweeps over the gain maximum and higher current at the edges of the spectrum, thus shaping the spectral peak flatter and broader. The total sweep range can hardly be extended*, but a more homogeneous power distribution over the sweep range can already improve the OCT depth resolution considerably. We achieve good results with a Gaussian peak truncated at the 10%-points on top of a constant baseline that ensures laser operation above threshold during the entire sweep. With approximately 30 mW peak power and 20 mW baseline (Fig. 4.3 c), we measured 23 mW average power and an axial resolution of 9 µm in air.

The relatively high baseline may not result in a PSF with optimal side-lobe suppression, but it has practical advantages. Reference interferograms generated with a Mach-Zehnder interferometer (MZI) have high amplitude over the entire sweep range (Fig. 4.3 d). This enables reliable extraction of the phase curve for frequency linearization. In im-

*Attempts to achieve lasing over a broadened sweep range led to the destruction of two SOAs. Apparently, the crystal facets or anti-reflection coatings on the output side took damage when the peak current exceeded 420–430 mA.

age data, the side-lobe suppression can be flexibly adjusted by numerical apodization of the A-scan interferograms.

After the spectral shaping, both sweep directions have equal power profiles. Hence both sweeps can be used for OCT imaging, as we confirm with test images (Fig. 4.4). The interferograms exhibit a small residual asymmetry, which we attribute to differences in the instantaneous laser linewidth. By letting the algorithm optimize the interferogram envelope instead of the power profile, we can eliminate this asymmetry (Fig. 4.3 f). While this does not yield an additional improvement of the resolution, it can be a way to compensate for wavelength-dependent losses in an imaging setup.

The sensitivity roll-off is rather fast, as plotted PSFs show (Fig. 4.5). We calculate the roll-off for a short probing depth with a linear fit to the PSF peaks for $z \leq 1\,\mathrm{mm}$ (Tab. 4.1). The roll-off is faster with spectral shaping, and in all cases faster for the backward sweep. Although a slower roll-off is preferable, the swept source can still be used for retinal imaging, since the retina is only a few hundred micrometers thick [233]. Other FDML swept sources and spectrometer-based systems with similar roll-off have been successfully applied for this purpose [43, 73].

Table 4.1.: Sensitivity roll-off (in dB/mm) for 1 mm probing depth.

	forward	backward
constant current	6.8	8.0
power spectrum shaped	7.8	9.6
interferogram shaped	8.5	10.8

The sweep spectrum is centered approximately at 1065 nm and coincides thus perfectly with the local minimum in the water absorption spectrum (Fig. 4.2). The axial resolution is hence minimally impaired by the surrounding water absorption bands. To verify this we have sim-

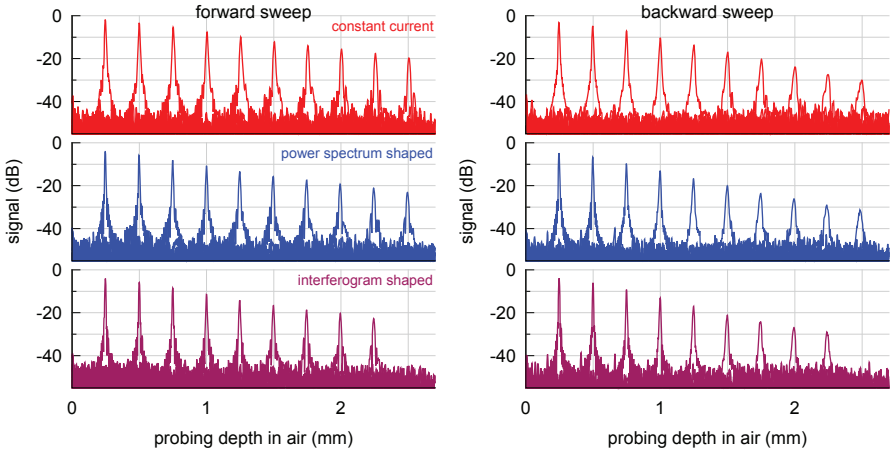

Figure 4.5.: Point spread functions obtained for both sweep directions with constant or modulated SOA current.

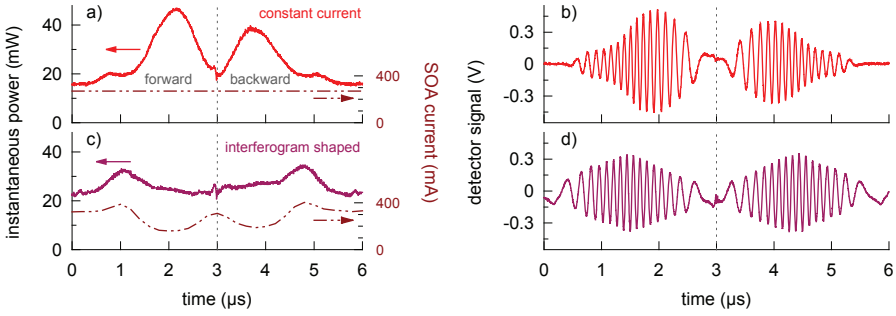

Figure 4.6.: Instantaneous output power (a, c) and exemplary interferograms (c, d) with 50 mm water in one interferometer arm.

ulated a double-pass through a human eye by placing a 50 mm thick water-filled glass vessel into one arm of the MZI. Although the interferogram amplitude is attenuated, the envelope shape with constant SOA

current changes not significantly (compare Fig. 4.3 b and Fig. 4.6 b). The resulting PSF is still 12 µm wide. By shaping the interferogram envelope symmetrically (Fig. 4.6 d), we obtain again the improved resolution of 9 µm. These results are consistent with our detailed numerical study on the impact of water absorption in retinal imaging (Ch. 5).

4.3. Discussion

Using a new broadband SOA, we set up an FDML swept source for the 1060 nm wavelength band featuring a sweep range up to 100 nm and more than 20 mW average output power. By modulating the pump current, we optimized the power spectrum and improved the axial resolution by 25% to 9 µm in air. Since compensation for the thermal drift of the tunable filter is crucial for the practical applicability of spectral shaping, we implemented automatic control of the filter bias voltage enabling hands-off operation for extended periods.

Both sweep directions exhibit similar performance and can be used for OCT imaging, enabling an A-scan rate of 350 kHz without buffering. Since the sweep spectrum is centered close to 1060 nm, the depth resolution is minimally affected by water absorption, making this light source ideal for retinal imaging.

There is still room for improving the performance. Most beneficial would be adequate dispersion compensation in the resonator. This could improve the sensitivity roll-off and eliminate the residual asymmetry between both sweep directions [64]. However, a feasible technical solution for the 1060 nm band has yet to be developed. Nevertheless, this comparably simple and robust light source configuration can already be applied in high-speed OCT imaging with high resolution, as we confirm with images of the human retina in vivo (Ch. 6).

5. The impact of water absorption in retinal imaging

In vivo OCT imaging of the human posterior eye segment is to a large extent governed by the optical properties of water, the main constituent of the vitreous humor [89]. Whereas dispersion is very low in a broad range around 1060 nm [91], a considerable fraction of the probing light is absorbed. For propagation through 50 mm water—which corresponds roughly to a double-pass through a human eye—the absorption minimum at 1060 nm is a relatively narrow operating window with 100 nm FWHM (Fig. 2.3). The parts of the light source spectrum that extend into the absorption bands are subject to increased attenuation, which narrows the transmitted spectrum and reduces the axial resolution of the OCT system. By adapting the light source spectrum, one can compensate for the water absorption at the expense of higher average attenuation [196]. However, the total incident power on the eye is limited by the maximum permissible exposure (MPE). Hence, maintaining the axial resolution comes with a penalty in signal strength or sensitivity, respectively, which increases with the light source bandwidth. This raises the question: how broad a bandwidth is actually useful for OCT in the 1060 nm band? Or more specifically: what is the resolution-sensitivity trade-off depending on the light source bandwidth?

As Hariri et al. concluded earlier [196], 3 µm resolution in air could be achieved with a hypothetical light source generating a truncated Gaussian spectrum after water absorption. They did, however, not state which fraction of the probing light would be absorbed. Experimentally, they compared the resolution achievable with a regular SLD and a "mod-

ified" SLD featuring an increased spectral peak in the short-wavelength absorption band. In the case of a double-pass through 25 mm water, the resolution in air improved minimally from 7.9 µm to 7.7 µm. As this light source did not permit arbitrary spectral shaping, the question about the feasibility of true absorption compensation remained unanswered.

Recent technological developments make a detailed analysis of the topic once more highly relevant. With new broadband SOAs, swept sources spanning the 1060 nm water absorption window have become possible. Bandwidths in the range of 90–100 nm have been demonstrated with FDML lasers and up to 120 nm with short-cavity lasers. At the same time, high-speed SOA drivers enable optimization of the light source spectrum and true absorption compensation. However, due to the resolution-sensitivity trade-off and technical challenges connected with implementing broadband light sources, it is important to know how effectively broad bandwidth can be used.

With a numerical simulation, we have investigated the impact of water absorption, covering a wide range of bandwidths and center wavelengths. As our results show, current state-of-the art light sources with a bandwidth up to 120 nm centered close to 1060 nm are not severely affected. The resolution degradation is below 10 % and can be compensated with minimal loss of sensitivity. The impact increases drastically when the bandwidth exceeds 150 nm, and for further broadening lower center wavelengths yield the best performance.

In the following sections, we explain the method of the simulation (Sec. 5.1), present the results (Sec. 5.2), and discuss their meaning for present and future swept source design (Sec. 5.3).

5.1. Method

Using a script implemented in Mathematica, we simulate the interference of two beams from the same light source in a simple interferometer, and we calculate a point spread function (PSF) from the resulting sig-

nal. We compare the PSFs in the cases assuming no water absorption or transmission through 50 mm of water in one interferometer arm. Furthermore, we calculate a light source spectrum that yields the original interferogram shape after water absorption with the same average power as the initial spectrum. A comparison of the PSF amplitudes gives a measure of the sensitivity drop due to the absorbed fraction of the light. We neglect the effects of chromatic dispersion in water, because it is low in this spectral range and can be corrected numerically in a real system [78].

We perform the simulation using a light source spectrum with Gaussian shape truncated at the $1/e^2$-points.

$$I_0(\nu) = \begin{cases} \exp\left[-2\left(\frac{\nu-\nu_c}{\Delta\nu/2}\right)^2\right] & \text{if} \quad |\nu-\nu_c| \leq \Delta\nu/2 \\ 0 & \text{if} \quad |\nu-\nu_c| > \Delta\nu/2 \end{cases} \tag{5.1}$$

ν_c is the center frequency and $\Delta\nu$ is the full width of the spectrum. This spectral shape results in a good compromise between a narrow peak and low side lobes of the PSF, and can be realized with an SOA-based swept source with rapid current modulation.

In order to determine the sensitivity penalty, we compare the signal amplitudes achieved with different spectra normalized to equal average intensity. For an arbitrary spectrum, $I_x(\nu)$, we calculate the time-averaged intensity

$$\langle I_x \rangle = \frac{1}{\tau_{sw}} \int_0^{\tau_{sw}} I_x(\nu_l(t))dt. \tag{5.2}$$

By integrating over one sweep period, τ_{sw}, of the time-dependent light source frequency, $\nu_l(t)$, we can take a non-linear sweep into account. We assume here the most non-linear sweep characteristics found in a swept source, sinusoidal tuning of the wavelength, which results in a frequency sweep

$$\nu_l(t) = \left\{ \frac{1}{\nu_{max}} + \frac{1}{2}\left(\frac{1}{\nu_{min}} - \frac{1}{\nu_{max}}\right)\left[1 + \sin\left(2\pi\,\frac{t}{\tau_{sw}}\right)\right]\right\}^{-1}, \tag{5.3}$$

where $\nu_{max} = \nu_c + \Delta\nu/2$ and $\nu_{min} = \nu_c - \Delta\nu/2$. With the average intensity thus calculated, we normalize the light source spectrum:

$$I_{0n}(\nu) = \frac{I_0(\nu)}{\langle I_0 \rangle}. \tag{5.4}$$

After transmission through a length of water, l, the spectrum changes according to the Beer-Lambert law:

$$\begin{aligned} I_{0a}(\nu) &= I_{0n}(\nu)\, T(\nu) && (5.5)\\ &= I_{0n}(\nu)\, \exp[-\mu_a(\nu) l]. && (5.6) \end{aligned}$$

For the absorption coefficient, μ_a, we use the values reported by Palmer and Williams [82] interpolated with cubic splines.

Assuming perfect balanced detection and neglecting chromatic dispersion in water, the detector signal* generated with an interferometer path length difference, d, is

$$V_{0n}(\nu) = I_{0n}(\nu)\, \cos\left(\tfrac{2\pi}{c}\nu d\right) \quad \text{(without absorption)}, \tag{5.7}$$

$$V_{0a}(\nu) = \sqrt{T(\nu)}\, I_{0n}(\nu)\, \cos\left(\tfrac{2\pi}{c}\nu d\right) \quad \text{(absorption in one arm)}. \tag{5.8}$$

In order to yield an interferogram with the original spectral envelope after water absorption, we calculate a compensating spectrum and normalize it:

$$I_c(\nu) = \frac{I_0(\nu)}{\sqrt{T(\nu)}}, \tag{5.9}$$

$$I_{cn}(\nu) = \frac{I_c(\nu)}{\langle I_c \rangle}. \tag{5.10}$$

*For simplicity, we omit a constant conversion factor between differential intensity and detector signal.

The resulting detector signal assuming water absorption in one interferometer arm,

$$V_{ca}(\nu) = \sqrt{T(\nu)}\, I_{cn}(\nu)\, \cos\left(\tfrac{2\pi}{c}\nu d\right) \tag{5.11}$$

$$= \frac{I_0(\nu)}{\langle I_c \rangle}\, \cos\left(\tfrac{2\pi}{c}\nu d\right) \tag{5.12}$$

$$= V_{0n}(\nu)\, \frac{\langle I_0 \rangle}{\langle I_c \rangle}, \tag{5.13}$$

has the same shape as V_{0n}, but a lower amplitude.

Fig. 5.1 illustrates the principle with examples for I_{0n}, I_{0a}, and I_{cn} at two different bandwidths. A spectrum with state-of-the-art bandwidth (30 THz) centered in the water absorption minimum is almost uniformly attenuated. For compensation, only a small fraction of the total power needs to be redistributed from the center to the edges. In contrast, an ultra-broadband spectrum would require a large power fraction for com-

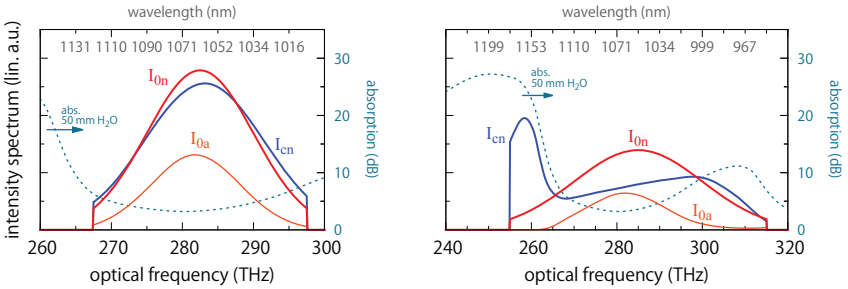

Figure 5.1.: The shape of a state-of-the-art broadband spectrum (left, $\Delta\nu = 30\,\mathrm{THz}$) changes only slightly. A hypothetical ultra-broadband spectrum (right, $\Delta\nu = 60\,\mathrm{THz}$) gets strongly attenuated below 265 THz, and compensation would here require a large fraction of the total power. I_{0n} and I_{cn} are normalized to unity power.

pensating the attenuation of the tail extending into the steep absorption band edge below 265 THz.

To quantify the effect of water absorption with and without spectral compensation, we calculate V_{0n}, V_{0a}, and V_{ca} with different values of ν_c (275 THz to 290 THz) and $\Delta\nu$ (5 THz to 60 THz). We calculate interferograms with $l = 50$ mm and $d = 0.5$ mm and compute the corresponding PSF with a discrete Fourier transform (DFT). For the DFT, we sample all signals from 200 THz to 400 THz in 0.1 THz steps, which produces a sufficient number of equally spaced data points in all PSFs. Finally, we determine the amplitude, a, and FWHM, w, of the PSF peaks by fitting a Gaussian function to the data points. Comparison of a in the three cases yields the signal drop caused by the water absorption, and $w/2$ (in µm) is the corresponding axial resolution in air.

5.2. Results

For our investigation, there are two quantities of interest: the relative broadening of the PSF peak due to the water absorption, $(w_{0a} - w_{0n})/w_{0n}$, and the drop of the signal amplitude with and without compensation relative to the reference without water absorption, a_{0a}/a_{0n} and a_{ca}/a_{0n}. We compare these as a function of the bandwidth at different center frequencies (Fig. 5.2), or vice versa (Fig. 5.3). The signal drop is plotted here on a $20\log_{10}$ scale, which corresponds to the decrease in OCT sensitivity (in dB). We use the optical frequency as abscissa in all plots, but we add auxiliary labels with the corresponding wavelength or wavelength range.

With a bandwidth < 25 THz (90–100 nm), the resolution degrades by less than 10% at all center frequencies covered by the simulation (Fig. 5.2 a). The broadening increases fastest with the bandwidth at the low center frequencies, which are closest to steep absorption band edge. Maintaining the resolution would bring a considerable sensitivity penalty that increases rapidly for bandwidths > 30 THz (Fig. 5.2 b). As

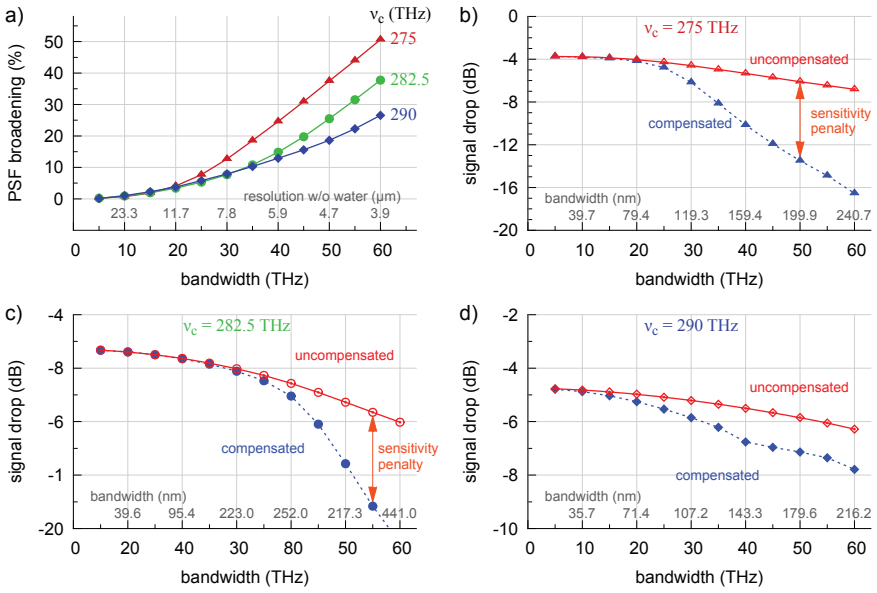

Figure 5.2.: Broadening of the point spread function (a) and signal drop (b-d) as function of the bandwidth. The secondary abscissa scale in (a) states the axial resolution in air without degradation by water absorption.

expected, the lowest signal drop with a low or moderate bandwidth can be achieved with a sweep spectrum centered on the water absorption minimum (Fig. 5.2 c), whereas a high center frequency leads to the slowest drop—with and without compensation—and would be of advantage with a bandwidth > 50 THz (Fig. 5.2 d).

The PSF broadening and the signal drop as function of the center frequency reveal the same relationships (Fig. 5.3), but this visualization is more useful for choosing the optimal operating point for a given bandwidth. With a moderate bandwidth of 30 THz, the resolution degradation is almost constant in the range of the simulation (Fig. 5.3 a). It

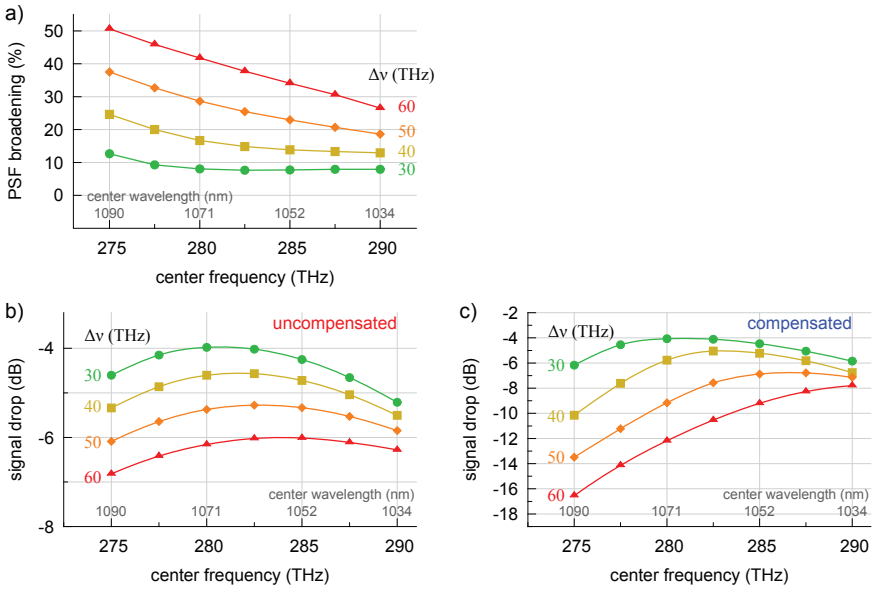

Figure 5.3.: Broadening of the point spread function (a) and signal drop (b-c) as function of the center frequency.

only rises slightly if $\nu_c \leq 280\,\mathrm{THz}$. The signal drop (Fig. 5.3 b) is lowest at $\nu_c = 280$–$282\,\mathrm{THz}$ (1065–1070 nm) and the penalty for compensating the resolution degradation is negligible (Fig. 5.3 c). If the bandwidth increases, the resolution degrades significantly faster at the low center frequencies, and the point of minimal signal drop shifts to higher frequencies. With the uncompensated spectrum, the signal drop varies only slightly ($< 1\,\mathrm{dB}$). However, the penalty for maintaining the resolution by absorption compensation becomes highly dependent on the center frequency, because of the steep absorption band edge on the long-wavelength side. The transmitted spectrum is virtually clipped at 1140–1150 nm, and a large fraction of the incident power needs to be sacrificed for compensating these losses.

5.3. Discussion

As our simulation reveals, current state-of-the-art swept sources with bandwidths up to 25–30 THz (≤ 120 nm) suffer little degradation of the resolution ($< 10\%$) if the sweep range is centered on the water absorption minimum (1060–1070 nm). This includes both prototypes we presented in the previous chapters (Ch. 3 & Ch. 4). Maintaining the optimal resolution by spectral shaping is in this range possible with a negligible penalty (< 1 dB). The resolution limiting effect becomes severe when the bandwidth exceeds 40 THz ($\sim$150 nm). Then, the optimal operating range shifts to shorter wavelengths, because all spectra are virtually clipped at 1140–1150 nm by the steep absorption band edge.

Our numerical study focuses on one spectral shape, but it reveals the general trends representative for typical swept sources. With the bandwidth provided by state-of-the-art SOAs, water absorption is not a severely limiting factor for the axial resolution, as long as the center wavelength is close to the absorption minimum. Further extension of the bandwidth is only feasible towards the short-wavelength side where the absorption band is significantly lower.

The exact numbers for resolution degradation and sensitivity drop depend of course on the particular spectrum and sweep characteristics, but the simulation can easily be adapted and offers a framework for studying a variety of effects in OCT systems. Not only can one assume arbitrary spectra or sweep characteristics. One can, for instance, include influences from an imaging setup or chromatic dispersion in the beam path. Given the increasing technical challenges connected with extending the bandwidth of swept sources, this model is a valuable tool for determining the optimal specifications at an early stage in the development process.

6. Retinal imaging

After the basic characterization, we demonstrated the performance of both light source prototypes (Ch. 3, Ch. 4) in OCT imaging of the human retina in-vivo. With the high-power swept source, we recorded retinal images at LMU subsequent to installing the buffering stage. We used both prototypes in conjunction with the polarization-sensitive OCT (PS-OCT) system at Medical University of Vienna (MUW).

In the following, we present the retinal images recorded with both the high-power swept source (Sec. 6.1) and the broadband swept source (Sec. 6.2). Although the sets of images are not directly comparable due to acquisition with different OCT setups and under varying conditions, they permit a general evaluation of the light source performance. We will also discuss the practical applicability of both configurations and point out where further development is required (Sec. 6.3).

Appendix C provides a brief introduction to the anatomy of the retina and its adjacent layers. The PS-OCT setup and the method of signal evaluation are described in Appendix D.

6.1. Imaging with the high-power swept source

Using the high-power swept source with a buffering stage, we can acquire OCT images at an A-scan rate of 350 kHz. Exemplary B-scans out of a 3D dataset (Fig. 6.1) show adequate resolution of the retinal layers and deep penetration into the choroid and the sclera. By averaging a number of B-scans, we can reduce speckle and detector noise, which yields a clear definition of the retinal layer boundaries, the choroid structure

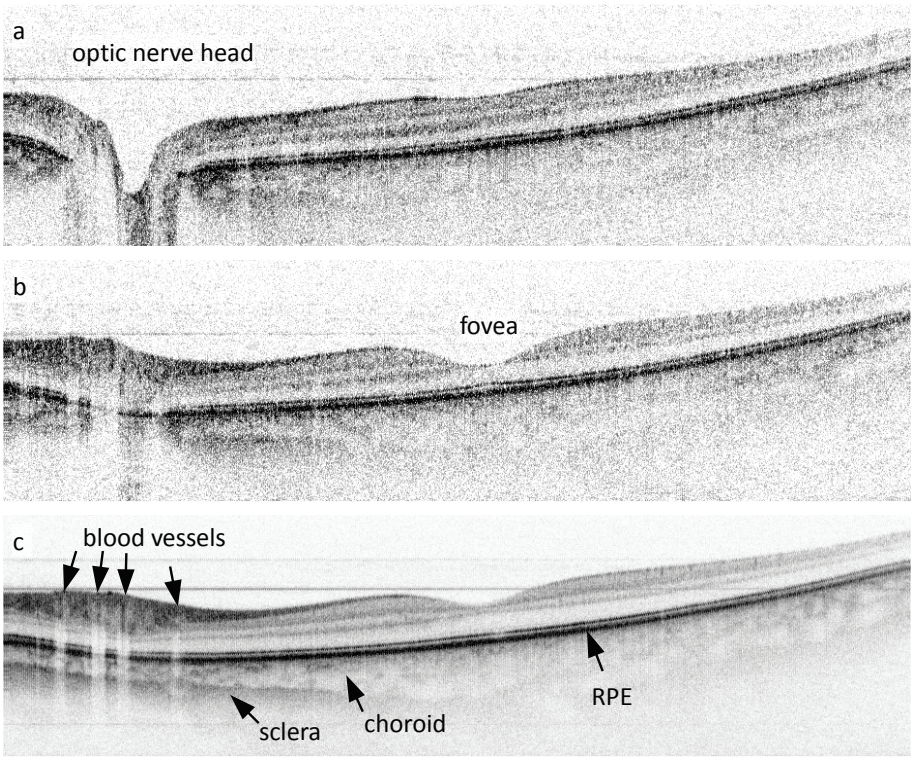

Figure 6.1.: Retinal OCT images acquired with the high-power swept source show an adequate resolution of the layer structure and deep penetration into the choroid. (a, b: single frames, c: 10 frames averaged)
Acquired by T. Klein (LMU). Sample power: 1.5 mW; data acquisition: 12 bit, 400 Msamples/s, 200 MHz analog bandwidth.

and the choroid/sclera interface. The average over ten adjacent frames (Fig. 6.1 c) illustrates the ability to utilize the high data-acquisition rate for improving the image quality, although one would normally use more

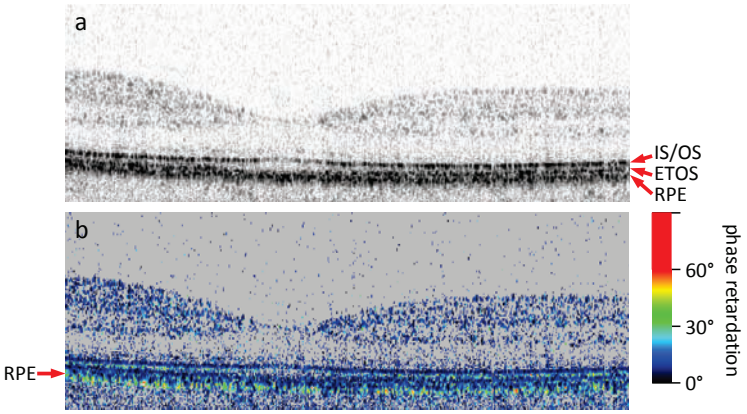

Figure 6.2.: The high-power swept source is suitable for PS-OCT, as preliminary images show (a: reflectivity, b: phase retardation). Acquired by T. Torzicky (MUW). Sample power: 2 mW; data acquisition: 12 bit, 500 Msamples/s, 350 MHz analog bandwidth.

densely sampled frames or several frames from the same location.

Light from the laser resonator is to a high degree linearly polarized because of the polarization-dependent gain of the SOA and the TA. After adjustment with a polarization controller, more than 90% pass a polarizer. Hence, we can use the swept source output for PS-OCT imaging with only a minor loss for filtering the polarization state.

As test images acquired at MUW (Fig. 6.2) confirm, the light source works well in PS-OCT imaging. Although the imaging setup was still under development and did not yield optimal sensitivity, the images show the expected features: very low phase retardation in most of the retinal layers and polarization-randomizing in the retinal pigment epithelium (RPE). The resolution is sufficient to distinguish the inner segment/outer segment junction of the photoreceptors (IS/OS), the end

tips of the photoreceptor outer segments (ETOS), and the RPE*.

During imaging, difficulties in the practical handling of this swept source setup became apparent. For optimal fiber-coupling of the tapered amplifier, the fiber-tips must be positioned in the lens focus with micrometer-precision. Drift of the used 3-axis translation stages makes frequent readjustments necessary—sometimes as often as every 30 minutes. While this has not been a severe problem for the characterization, it limits the feasibility for extended OCT measurement series. Furthermore, adjustment of the numerous degrees of freedom in the setup can be time-consuming and requires a considerable amount of experience.

Because fiber-coupled broadband SOAs have become available, which can generate adequate power levels, we have not continued working with the high-power swept source. With the broadband swept source, buffering is not necessary, because both sweep directions can be used for OCT imaging. Hence, it can provide sufficient power for the OCT system at MUW.

6.2. Imaging with the broadband swept source

The broadband swept source is feasible for retinal imaging, as a set of PS-OCT images of a human fovea in vivo shows (Fig. 6.3). We acquired the A-scans at a rate of 350 kHz using both the forward and the backward sweep. Like in the test images (Fig. 4.4), we cannot see any artifacts resulting from differing signal quality of the two sweep directions. The sensitivity is 95–96 dB for the forward sweep and about 94 dB for the backward sweep. We recorded 50 B-scans at the same location, which we average (Fig. 6.3 b, d-f) to reduce noise and speckles.

The axial resolution is sufficiently high to distinguish all retinal layers (Fig. 6.3 b) that have been identified previously in OCT literature

*There has been some controversy about the physical origin of the "triple band" structure at the outer boundary of the retina in high-resolution OCT images [234]. We adopt here the interpretation that seems most plausible, to date.

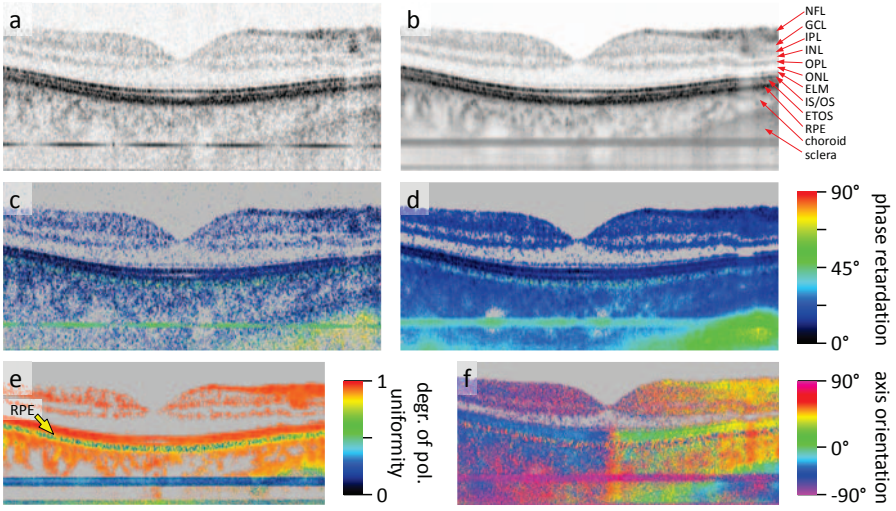

Figure 6.3.: With the broadband swept source, we can acquire high-resolution PS-OCT images of the retina with deep penetration into the choroid and the sclera (a, c: single frames; b, d-f: 50 frames averaged). The horizontal stripe in the lower part is a parasitic signal from the imaging/detection system.
Acquired by T. Torzicky (MUW). Sample power: 2 mW; data acquisition: 12 bit, 500 Msamples/s, 350 MHz analog bandwidth.
Retinal layers: NFL: nerve fiber l., GCL: ganglion cell l., IPL: inner plexiform l., INL: inner nuclear l., OPL: outer plexiform l., ONL: outer nuclear l., ELM: external limiting membrane, IS/OS: inner segment/outer segment junction of photoreceptors, ETOS: end tips of photoreceptor outer segments, RPE: retinal pigment epithelium.

[9, 112, 235]. The three highly reflective layers at the outer part of the retina (IS/OS, ETOS, RPE) are clearly resolved; also the external limiting membrane (ELM) is visible. The penetration is sufficient for imaging the choroid and parts of the sclera. At the choroid/sclera boundary, the phase retardation increases steeply (Fig. 6.3 c,d), whereas it is nearly

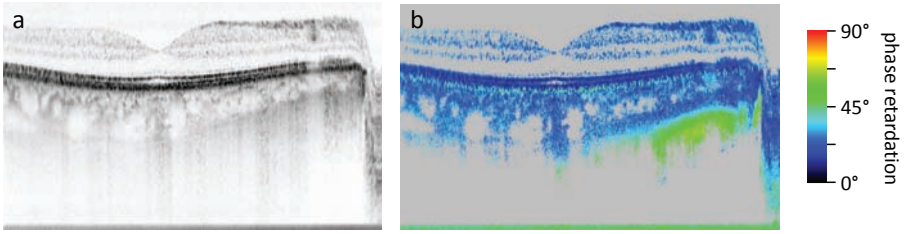

Figure 6.4.: Reflectivity (a) and retardation (b) images as in Fig. 6.3 b+d with the reference plane positioned deeper behind the retina. The depth of the optic nerve head (right edge) is covered, but due the sensitivity roll-off, the signal from the inner retinal layers gets weaker. Acquired by T. Torzicky (MUW).

constant in the non-birefringent inner retinal layers and in the choroid. The depolarizing RPE appears clearly as a layer of random retardation values. It can be distinguished even better by its low degree of polarization uniformity (DOPU) calculated from the averaged Stokes vectors of the 50 B-frames (Fig. 6.3 e).

The optical axis map (Fig. 6.3 f) is not as straight-forward to interpret, but it shows typical features that have been reported previously [107]: a laterally varying offset in the inner retinal layers originating from the anterior eye segment, and a changing value in the central part of the outer retinal layers (IS/OS, ETOS), caused by the Henle fiber layer[†]. However, axis orientation data are generally more meaningful in a transverse plane view of segmented layers from a 3D dataset, where they, for instance, may be associated with the direction of fiber bundles.

Also the broadband swept source emits inherently highly polarized light. Hence, up to 90% of the power can pass the polarizer at the interferometer input. With a polarization controller on the delivery fiber, we can adjust the exact power level for imaging.

[†]An area in the central retina with oblique photoreceptor axons.

The entire retina and choroid can be imaged in the fovea region, despite the fast roll-off. However, precise positioning of the reference plane is necessary to capture the region of interest with high sensitivity, which complicates the process. The roll-off becomes problematic for imaging the optic nerve head, which extends over a longer depth range (Fig. 6.4). Hence, improvement of the laser linewidth is important for practical applicability of this swept source configuration.

6.3. Discussion

Both the high-power swept source and the broadband swept source are feasible for retinal imaging. In reflectivity images, we can resolve the retinal layers reported in the OCT literature. Phase retardation images show the expected features, low birefringence in most of the retina and the choroid, depolarization in the RPE and increasing birefringence at the sclera boundary. Both swept sources emit inherently polarized light, which can be used for PS-OCT without significant losses.

In terms of performance and handling, both configurations have advantages and drawbacks. The high-power swept source features a slower sensitivity roll-off, which increases the tolerance for positioning the reference plane relative to the sample, and allows to image structures extending over a larger depth range like the optic nerve head. The light source setup is more complex, since two optical amplifiers are needed. Due to the strong asymmetry between forward and backward sweep, imaging with the full A-scan rate requires buffering, which reduces the output power by 6 dB. Most important for practical application is stable fiber-coupling of the tapered amplifier to eliminate the need for frequent readjustment. Integration of tapered amplifiers into compact fiber-coupled modules is possible [229], although these are not yet commercially available.

The broadband swept source features a less complex and more robust setup, using only a single fiber-coupled SOA. Due to the high sweep

symmetry, both sweep directions can be used for imaging, hence no buffering stage is necessary. As a result, the broadband swept source can provide almost as much power as the buffered high-power swept source, which is sufficient for a standard OCT system for ophthalmology. The relatively fast sensitivity roll-off limits the useful probing depth range. In the fovea region, the entire retina and choroid can be imaged, but for deeper structures like the optic nerve head, an improvement of the roll-off is necessary. Adequate dispersion compensation for the FDML resonator is a promising approach [64], as soon as a feasible technical solution for the 1060 nm band is developed. With the resulting narrowed instantaneous linewidth, the broadband FDML laser will be an excellent light source for high-speed retinal OCT imaging.

7. Summary and outlook

Within the frame of this project, we have explored different concepts for improving the performance of swept sources for optical coherence tomography (OCT) in the 1060 nm range. We have focused mainly on the possibilities given by new semiconductor gain media, specifically tapered amplifiers for generating abundant output power and broadband semiconductor optical amplifiers (SOAs) enabling a wide sweep bandwidth without a complex setup. We have developed two prototype light sources and demonstrated their feasibility by applying them in retinal OCT imaging. Furthermore, we have tested an approach for achieving better performance in high-speed Fourier domain mode-locked (FDML) lasers by using a low-dispersion fiber delay line, and we have investigated numerically how the water absorption bands above and below 1060 nm limit the depth resolution for OCT imaging of the human retina.

As our experiments reveal, tapered amplifier technology is feasible for implementing swept sources with high output power. With our prototype FDML laser, we can demonstrate 30–50 mW average power over a sweep range up to 80 nm. By buffering the output, we achieve an A-scan rate up to 350 kHz with 10–15 mW average power. Thus, we can acquire large sets of high-quality retinal images within a few seconds.

Using the low-dispersion photonic crystal fiber (PCF) as delay line in this FDML laser does not yield improved performance, as compared to conventional single-mode fiber. Although lower asymmetry in the output power for the two sweep directions is a clear indicator for reduced dispersion, the sensitivity roll-off improves only marginally. Due to high insertion loss the bandwidth narrows even slightly. Furthermore, fast

polarization-rotation leads to a "notched" or even discontinuous spectrum. Unless these issues can be resolved, the PCF is not feasible for implementing low-dispersion FDML resonators.

Instead, high gain—in our case provided by an additional SOA—permits exploiting the full bandwidth of the used gain media, even with a dispersive delay line in use. Imperfect frequency matching caused by chromatic dispersion is translated into additional wavelength-dependent losses by the tunable filter. Hence, the resulting limitation of the sweep bandwidth can, to a certain extent, be compensated by sufficiently high gain.

With the availability of new broadband SOAs, high performance swept sources with a simple and robust all-fiber setup have become possible. In a second prototype using only a single SOA, we have demonstrated a sweep range up to 100 nm centered near the water absorption minimum at 1060 nm. Due to high small-signal gain, the performance is very similar for both sweep directions, and this can be further improved by spectral shaping. Hence, we can utilize the full bidirectional sweep rate of 350 kHz without buffering. By spectral shaping, we can also optimize the axial resolution for a given sweep bandwidth, and achieve an improvement by 25% to 9 µm in air (∼6.5 µm in tissue). Crucial for spectral shaping, we compensate for the thermal drift of the tunable filter with an automatic control algorithm ensuring stable long-term operation of the light source.

We have applied both light sources successfully for in vivo polarization-sensitive OCT imaging of the human retina. We achieve sufficient resolution for distinguishing the retinal layers, as well as deep penetration into the choroid and the sclera. The less complex broadband swept source configuration is easier to handle, and is thus better suited for practical application. It yields a better resolution, but exhibits a faster sensitivity roll-off, which makes imaging of extended structures, like the optic nerve head, difficult. An important direction for future development is hence dispersion compensation for FDML resonators in the 1060 nm band.

The development of specialized semiconductor gain elements would be highly interesting, as well. Tapered amplifiers, on the on hand, can emit significantly more power than required for biomedical OCT applications, but their small-signal gain is too low for effective operation in a single-amplifier configuration. The new broadband SOAs, on the other hand, have a wide bandwidth and high gain. They could also generate abundant power—the saturation level is in the range of 50 mW ex-fiber or higher—but this potential cannot be exploited due to the hazard of damaging the output facet. A combination of these technologies—broadband high-gain SOAs with a raised damage threshold, possibly realized by adding a short tapered section—could be the key to an ideal swept source gain medium.

Motivated by the continuing development of broadband light sources, we have investigated numerically how the water absorption bands above and below 1060 nm impair the OCT resolution, and whether compensation by spectral shaping is feasible. As our simulation shows, currently available swept sources are only minimally affected as long as their spectrum is centered on the absorption minimum. Absorption compensation is in this case possible with only a minor sensitivity penalty. With increasing bandwidth, the optimal operating point shifts to shorter center wavelengths. Whereas our simulation reveals the general trends for typical light source characteristics, it can be adapted to a wide range of particular cases, and may thus become an important tool for future development of ultra-broadband swept sources.

During the past few years, the field of swept source development has grown rapidly, in research and industry alike. Driven by the demand for high-speed image acquisition, considerable efforts went into increasing the sweep rate. With the progress in MEMS technology, compact tunable lasers have become available that permit some hundred kilohertz sweep rate, and other implementations approaching the megahertz regime are about to enter the market. In the short and medium term, however, FDML lasers will enable the highest possible sweep rates.

Since we performed our studies using FDML resonators, the concepts we investigated are feasible for high speed imaging. However, most of our results—especially those demonstrating the possibilities of new semiconductor gain media—are also applicable to other types of tunable lasers, and are hence a valuable contribution to the development of the next generation of high-performance, high-speed swept sources.

A. Low-dispersion FDML resonator

In a first experiment (Ch. 3), we have been able to reduce the dispersion effects in an FDML laser by using a specialty photonic crystal fiber (PCF) with a zero-dispersion point close to 1040 nm (NKT Photonics SC–5.0–1040) for the delay line. However, due to high insertion loss in the 1.75 km long fiber spool, the overall performance has not improved, as compared to using a delay line made of conventional single-mode fiber. A new prototype Fabry-Perot filter tunable with 420 kHz repetition rate permits a shorter FDML resonator length, approximately 485 m. Since the insertion loss of the delay line decreases with its length, we have investigated whether the PCF can be of advantage in this configuration. We observe a somewhat slower sensitivity roll-off with the PCF when comparing the performance at moderate sweep range, ∼67 nm. However, at higher bandwidth, fast polarization rotation in the PCF leads to interruption of the laser activity at several wavelengths, which we cannot compensate with polarization controllers.

The PCF features not only low chromatic dispersion between 1000 nm and 1100 nm, the dispersion is also anomalous at wavelengths above 1030–1040 nm, and can thus to a certain extent compensate the normal dispersion of conventional fiber (such as Corning HI 1060 or SMF28). Hence, a delay line consisting of according lengths of the PCF and of standard single-mode fiber (SMF) appears promising.

After measurements of different fiber dispersion profiles, we can estimate the total wavelength-resolved round-trip time. With 410 m PCF, 55 m SMF28 and the remaining length of the resonator formed by the HI 1060 fibers of the optical components, we obtain a zero-dispersion

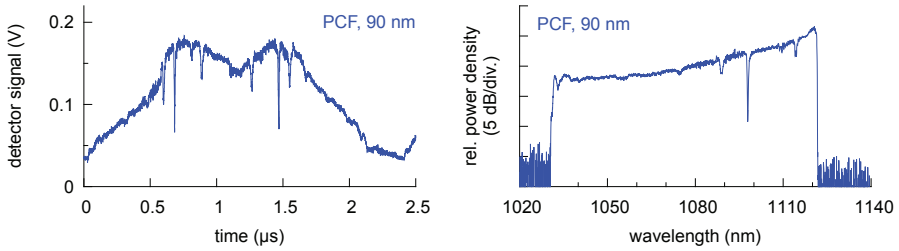

Figure A.1.: The instantaneous output power (left) and the averaged spectrum (right) exhibit deep "notches" caused by fast polarization rotation.

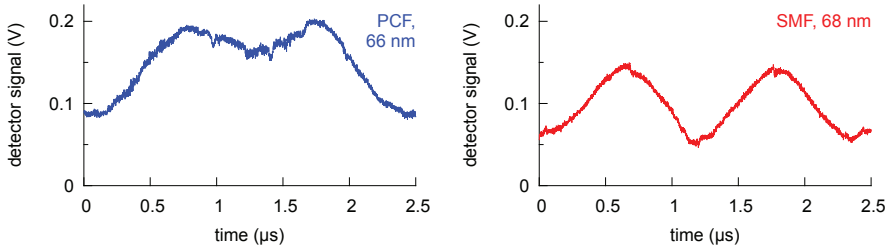

Figure A.2.: A continuous sweep with the PCF delay line (left) is possible with reduced sweep range, but some polarization notches remain in the power spectrum. In contrast, the swept source runs well with the SMF delay line (right), even with lower SOA pump currents.

point close to 1060 nm. The maximum round-trip time mismatch in the range from 1000 nm to 1120 nm is approximately 170 ps, as compared to 1.6 ns with an all-SMF delay line.

The shortened PCF has a residual insertion loss of 5 dB, dominated

by the splice losses*. Due to this loss and loss in the other optical components, we need two SOAs in series for FDML operation. Polarization rotation in the delay line leads to notches in the sweep spectrum, which we cannot completely compensate by adjusting the polarization controllers. With wide sweep ranges ($> 70\,\mathrm{nm}$), laser activity is interrupted at several wavelengths during the sweep (Fig. A.1), which degrades the light source performance in OCT imaging. Even increasing the radius of the fiber spool to $26''$ does not solve the problem, although it should lower the bend-induced birefringence [236].

At a lower sweep range (66–68 nm), we compare the performance of the light source with either the PCF delay line or with SMF instead. With the lower loss of the SMF, the laser requires lower SOA currents for stable operation over the full sweep range (175 & 295 mA as compared to 300 & 380 mA with the PCF). The polarization can be adjusted without difficulty, whereas the instantaneous power envelope of the PCF configuration still shows some residual polarization notches (Fig. A.2). With the PCF, the sensitivity roll-off is slower, $4.4\,\mathrm{dB/mm}$ for $z \leq 2.5\,\mathrm{mm}$ as compared to $5.5\,\mathrm{dB/mm}$ with the SMF, but the difference is not as pronounced as expected from a 90% reduction of the round-trip time mismatch.

Judging by the results of this experiment, this PCF does not appear feasible for designing a low-dispersion FDML swept source. Although the use of the combined PCF-SMF delay line leads to a reduction of the sensitivity roll-off as compared to an all-SMF delay line, we cannot achieve a significantly longer coherence length due to the higher insertion loss. Furthermore, considerably faster polarization rotation in the PCF limits the achievable bandwidth for a continuous sweep. Unless these properties of the PCF can be improved, this approach of dispersion reduction is not feasible for practical swept source development.

*On each side, a piece of HI 1060 with a fiber connector is spliced to the PCF.

B. Gain-multiplexing

One way of increasing the gain bandwidth beyond that of a single SOA, is to use two SOAs with shifted gain spectra in a parallel configuration [232]. This concept can also be applied at 1060 nm, as we demonstrate here. However, while we achieve a tuning range of 120 nm, there is only a minor improvement in axial resolution due to significantly different output power levels of the two selected SOAs. Since the actual SOA performance as laser gain medium can hardly be predicted before purchase, we have not pursued this approach further.

The selected SOAs originate both from the same batch (InPhenix IPSAD1001–4113) and have similar ASE power and bandwidth, but different center wavelengths. Judging by the ASE spectra (Fig. B.1), this pair appears capable of a combined sweep range wider than 100 nm.

In a simple fiber-based tunable laser (Fig. B.2), we split the light into

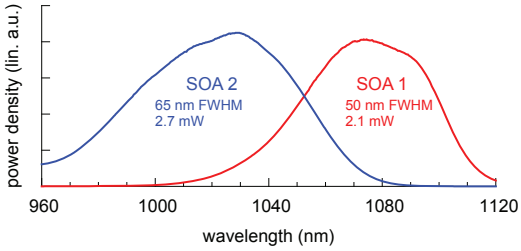

Figure B.1.: Judging by the spontaneous emission characteristics, the two selected SOAs can together span a spectral range wider than 1000 nm to 1100 nm.

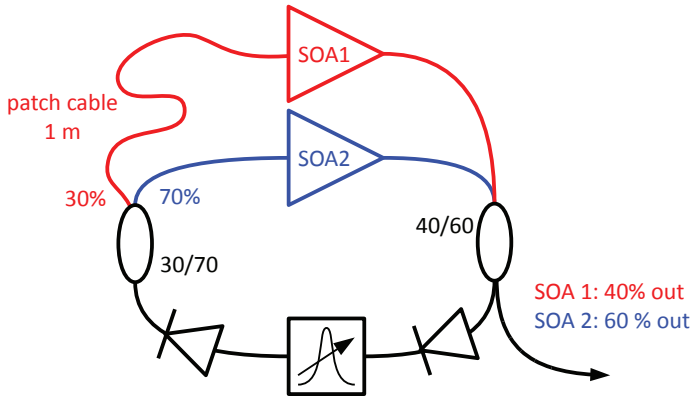

Figure B.2.: In the test setup, we avoid interference with different lengths of the two SOA branches. We adjust the fiber couplers in order to give SOA 2 stronger feedback and to extract more of its output power from the resonator.

two branches, each containing one SOA, and recombine it afterwards using ordinary fiber couplers. The recombining coupler serves at the same time as output coupler for the laser resonator. A 1 m fiber patch cable inserted in one branch prevents interference, which otherwise leads to a strong modulation of the output power. Unexpectedly, the output power contribution from SOA 2 is very low, even if it receives a larger fraction of the circulating light as feedback and a larger part of its output is extracted from the resonator. Despite similar ASE characteristics, the two SOAs have apparently considerably different saturation levels.

At 1 kHz sweep rate and 350 mA SOA current, a sweep range of 120 nm with continuous laser emission is possible (Fig. B.3 left). By switching each SOA off in turn, we can see their individual contributions. SOA 2 with its low output power adds only a flat tail on the short-wavelength side of the spectrum, as the instantaneous power traces reveal (Fig. B.3 right). The corresponding interferograms (Fig. B.4) show

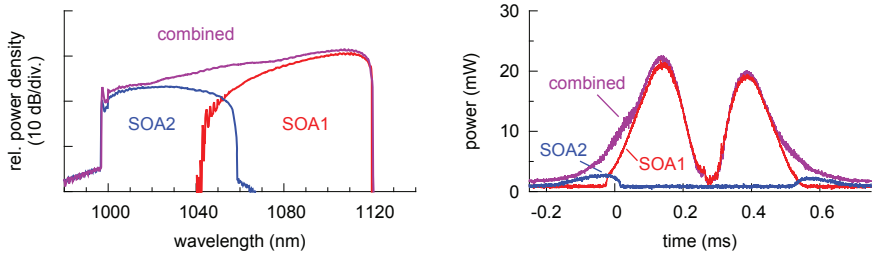

Figure B.3.: The combined bandwidth is considerably broader than that of the single SOAs (left). However, the instantaneous output power of SOA2 is significantly lower than of SOA1 (right) and adds only a flat tail on the blue end of the spectrum.

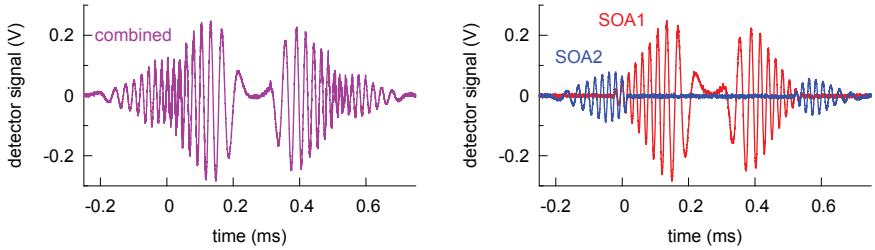

Figure B.4.: The interferogram spans a wider range when both SOAs are combined (left). However, SOA2 contributes only fringes with relatively low amplitude (right), not broadening the main peak.

the same features. The low amplitude signal from SOA 2 does not broaden the main peak of the interferogram and can hence hardly improve the OCT depth resolution. Remarkably, despite 1 m path length difference between the two branches, the power signals and interfer-

ograms exhibit residual interference noise in the overlap range of the single SOA contributions.

In another test, we compare the output power and achievable resolution with both or only one of the SOAs (Tab. B.1). When only one SOA is active, we adjust the tunable filter sweep range to the gain bandwidth of that SOA in order to see its actual "stand-alone" performance. Whereas the total sweep range with both SOAs combined is 40% wider than that of SOA 1 alone, the PSF becomes only about 12% narrower, due to the low output power of SOA 2.

Table B.1.: Comparison of the performance with gain-multiplexing and single-SOA operation

	power (mW)	sweep range (nm)	PSF width (a.u.)
SOA 1 only	7.5	83	5.0
SOA 2 only	3.4	63	5.6
combined	11.0	114	4.4

Although continued work on gain-multiplexing would not be meaningful with this SOA pair, we can draw the following conclusions from these test results. Equal performance of the used SOAs—especially in terms of the saturated output power—is crucial for gain-multiplexing. Unfortunately, SOA manufacturers do often provide only ASE characteristics, which is not sufficient for predicting the device performance as a laser gain medium. A choice of appropriate devices prior to purchase is hence nearly impossible.

Gain-multiplexing is possible in a simple setup using ordinary fiber couplers for splitting and recombining the light. However, interference between the different light paths must be avoided. This requires either equal path lengths with micrometer precision and high stability, or a

large path length difference of at least several decimeters. The former is technically challenging, and the latter is not feasible for high-speed FDML lasers, which require a uniform resonator length for all wavelengths. Other solutions for avoiding interference are necessary, e. g. a wavelength-multiplexing device for splitting and recombining the light, or rapid switching of the pump currents activating only one SOA at a time. Neither the transition slope of a wavelength-multiplexing element (such as a dichroic mirror) nor the rise time of an SOA driver can be infinitely narrow. Hence, there would always remain either residual interference artifacts or a gap in the swept source spectrum.

Taking the added complexity of the light source setup into account, gain-multiplexing using available fiber-optic components appears not feasible in the 1060 nm range. It could, however, be a viable method for increasing the bandwidth, if all beam splitting/combining optics are integrated together with the SOAs in one package with precise and stable alignment.

C. The posterior eye segment

The posterior segment of the human eye (Fig. C.1) is formed by the vitreous body and the enclosing shell that consists of three layers. The outermost protective coat is the *sclera*, which is partially visible as the white of the eye. On the inside, the sclera is covered with a network of blood vessels, called *choroid*. The choroid provides oxygen and nutrients to the *retina*, the light-sensitive innermost layer. The retina itself is divided into a number of distinct layers (Fig. C.2). Upon the retinal

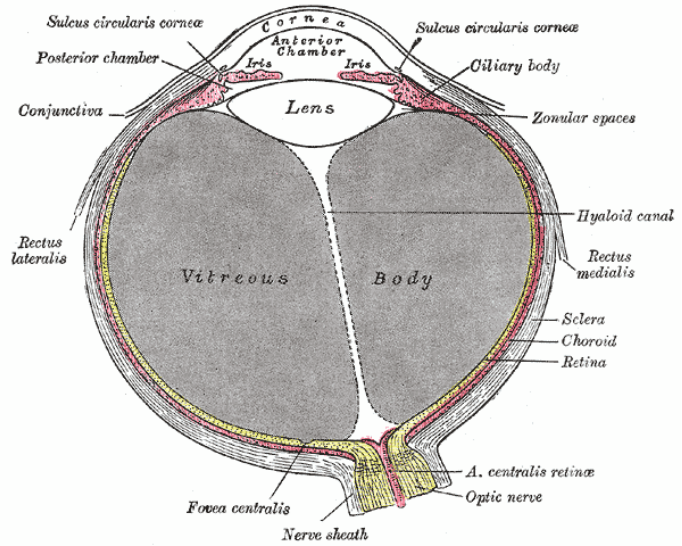

Figure C.1.: Schematic cross-section of the human eye. Source: [237]

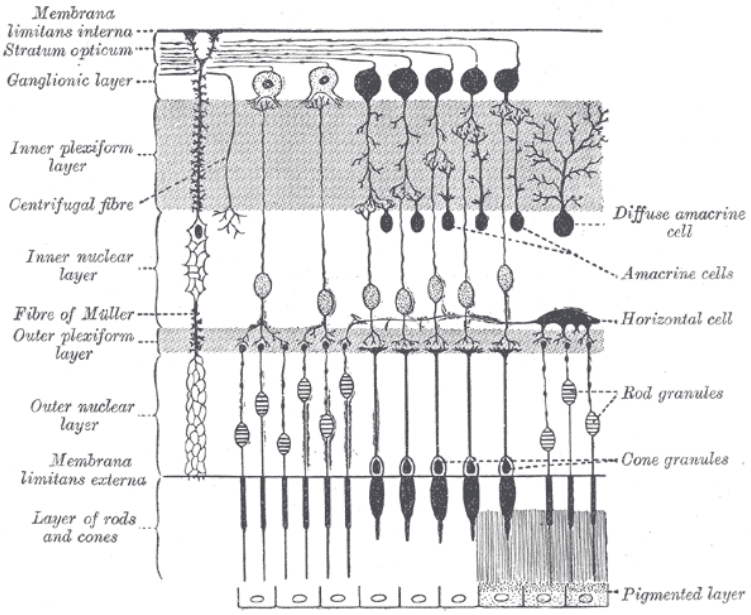

Figure C.2.: Schematic cross-section of the human retina illustrating the layer structure with different cell types. Source: [237]

pigment epithelium (RPE), that forms the border to the choroid, follow the photoreceptors, then different types of neurons and finally the nerve fibers that carry the visual information to the optic nerve. On the retina, there are two prominent spots, the optic disc where the optic nerve enters the eye—also called optic nerve head—and the fovea, a pit close to the center. The fovea has the highest density of photoreceptors providing high acuity vision, whereas the optic nerve head has no receptors at all and is hence a blind spot. The thickness of the retina ranges from 100–200 µm at the fovea to about 500 µm at the optic disc [233]. Beneath the fovea, the choroid is 200–300 µm thick, and gets thinner in the peripheral areas [233].

D. Polarization sensitive OCT

The PS-OCT setup at MUW (Fig. D.1) is a two-channel system that probes both polarization states simultaneously, as originally demonstrated by Hee et al. [21]. Light from the swept source passes a polarization controller and a polarizer. This creates a linear input polarization state and allows adjustment of the input power. A beam splitter cube distributes the light to the reference arm and the sample arm. In the reference arm, a half wave plate at 22.5° angle to the incident polarization vector turns the polarization by 45°, distributing the light equally to both polarization channels. The reference arm power can

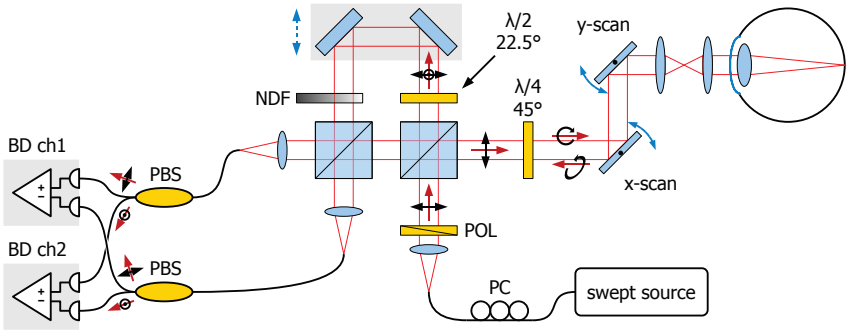

Figure D.1.: The two-channel PS-OCT setup can interrogate both orthogonal polarization states simultaneously. POL: polarizer, PC: polarization controller, PBS: polarizing beam splitter, BD: balanced detector, NDF: variable neutral density filter.

be adjusted with a variable neutral density filter. In the sample arm, the incident light passes a quarter wave plate at 45° angle and becomes thus circularly polarized. The light returning from the sample is in general elliptically polarized, depending on the phase retardation that it has accumulated on a double-pass through the sample. The intensity distribution in the two polarization channels changes accordingly. The returning probing beam interferes in a second beam splitter cube with the reference beam, independently in both polarization channels. Fiber-optic polarizing beam splitters separate the two polarization components of the light from both output ports and direct them accordingly to two balanced detectors.

Linearizing and Fourier transforming the two detector signals yields the complex A-scan profiles of both polarization channels, $\tilde{A}_{1,2}(z) = A_{1,2}(z)\exp[i\Phi_{1,2}(z)]$. From the amplitude, A, and the phase, Φ, we derive the local reflectivity, R,* the single-pass phase retardation angle, δ, and the optical axis orientation, θ [21, 111, 238]:

$$R(z) \propto A_1(z)^2 + A_2(z)^2, \tag{D.1}$$

$$\delta(z) = \arctan\left[A_1(z)/A_2(z)\right], \tag{D.2}$$

$$\theta(z) = 90^\circ - \tfrac{1}{2}\left[\Phi_1(z) - \Phi_2(z)\right]. \tag{D.3}$$

δ and θ are cumulative, i. e. in birefringent material the values change along the A-scan direction, in non-birefringent material they remain constant.

We can obtain images with reduced speckle and noise by averaging several B-scans. For the polarization images, we apply the methods that led to the best results in a previous study by Götzinger et al. [239]. We calculate the phase retardation from the separately averaged signals of both channels, and we average the phase difference in a complex phasor representation in order to avoid errors due to the 2π-discontinuity.

*Equivalent to an A-scan from a purely reflectivity-detecting OCT system, but free of artifacts caused by polarization rotation.

Phase retardation maps are an instrument for distinguishing polarization-maintaining, birefringent and depolarizing structures. The value at each point is cumulative for the distance that the light beam propagated through the sample. Hence, birefringence becomes apparent as a change in the retardation value along the A-scan axis, whereas a polarization-maintaining structure leads to a constant value. Depolarization is associated with the scattering process. Therefore, a depolarizing layer, such as the retinal pigment epithelium (RPE), appears as a band of random retardation values, but it does not randomize the values of deeper structures. In retinal imaging, this principle can be exploited for segmenting the RPE by calculating the so-called degree of polarization uniformity (DOPU)—equivalent to the degree of polarization calculated from an averaged Stokes-vector [112]—which yields low values for depolarizing structures. We average the Stokes vectors over many subsequently acquired B-frames, which preserves spatial resolution better than averaging over a spatial window [239].

List of Abbreviations

ADC analog-to-digital converter.

ANSI American National Standards Institute.

ASE amplified spontaneous emission.

CARS coherent anti-Stokes Raman scattering.

DBR distributed Bragg reflector.

DFT discrete Fourier transform.

DOPU degree of polarization uniformity.

DTU Technical University of Denmark.

ELM external limiting membrane.

ETOS end tips of the photoreceptor outer segments.

FD-OCT frequency domain OCT.

FDML Fourier domain mode-locked.

FDML Fourier domain mode-locking.

FSR free spectral range.

FT Fourier transform.

FWHM full width at half maximum.

IEC International Electrotechnical Commission.

IS/OS inner segment/outer segment junction of the photoreceptors.

LCI low coherence interferometry.

LMU Ludwig-Maximilians-Universität.

MEMS micro-electro-mechanical system.

MPE maximum permissible exposure.

MUW Medical University of Vienna.

MZI Mach-Zehnder interferometer.

NA numerical aperture.

NIR near-infrared.

NMSC non-melanoma skin cancer.

OCM optical coherence microscopy.

OCT optical coherence tomography.

OSA optical spectrum analyzer.

PCF photonic crystal fiber.

PS-OCT polarization sensitive OCT.

PSF point spread function.

RPE retinal pigment epithelium.

SD-OCT spectral domain OCT.

SLD superluminescent diode.

SMF single-mode fiber.

SNR signal-to-noise ratio.

SOA semiconductor optical amplifier.

SS-OCT swept source OCT.

TA tapered amplifier.

TD-OCT time domain OCT.

VCSEL vertical-cavity surface-emitting laser.

YDFA ytterbium-doped fiber amplifier.

Bibliography

[1] S. Marschall, B. Sander, M. Mogensen, T. M. Jørgensen, and P. E. Andersen, "Optical coherence tomography—current technology and applications in clinical and biomedical research," *Anal. Bioanal. Chem.* **400**(9), pp. 2699–2720, 2011.

[2] D. Huang, E. A. Swanson, C. P. Lin, J. S. Schuman, W. G. Stinson, W. Chang, M. R. Hee, T. Flotte, K. Gregory, C. A. Puliafito, and J. G. Fujimoto, "Optical coherence tomography," *Science* **254**(5035), pp. 1178–1181, 1991.

[3] W. Eickhoff and R. Ulrich, "Optical frequency domain reflectometry in single-mode fiber," *Appl. Phys. Lett.* **39**, pp. 693–695, 1981.

[4] D. Uttam and B. Culshaw, "Precision time domain reflectometry in optical fiber systems using a frequency modulated continuous wave ranging technique," *J. Lightwave Technol.* **3**(5), pp. 971–977, 1985.

[5] K. Takada, I. Yokohama, K. Chida, and J. Noda, "New measurement system for fault location in optical waveguide devices based on an interferometric technique," *Appl. Opt.* **26**, pp. 1603–1606, 1987.

[6] A. F. Fercher, K. Mengedoht, and W. Werner, "Eye-length measurement by interferometry with partially coherent light," *Opt. Lett.* **13**, pp. 186–188, 1988.

[7] D. Huang, J. Wang, C. P. Lin, C. A. Puliafito, and J. G. Fujimoto, "Micron-resolution ranging of cornea anterior chamber by optical reflectometry," *Laser Surg. Med.* **11**(5), pp. 419–425, 1991.

[8] M. E. van Velthoven, D. J. Faber, F. D. Verbraak, T. G. van Leeuwen, and M. D. de Smet, "Recent developments in optical coherence tomography for imaging the retina," *Prog. Retin. Eye Res.* **26**(1), pp. 57–77, 2007.

[9] W. Drexler and J. G. Fujimoto, "State-of-the-art retinal optical coherence tomography," *Prog. Retin. Eye Res.* **27**(1), pp. 45–88, 2008.

[10] A. F. Low, G. J. Tearney, B. E. Bouma, and I.-K. Jang, "Technology insight: optical coherence tomography – current status and future development," *Nat. Clin. Pract. Card.* **3**(3), pp. 154–162, 2006.

[11] G. J. Tearney, I.-K. Jang, and B. E. Bouma, "Optical coherence tomography for imaging the vulnerable plaque," *J. Biomed. Opt.* **11**(2), p. 021002, 2006.

[12] R. Steiner, K. Kunzi-Rapp, and K. Scharffetter-Kochanek, "Optical coherence tomography: Clinical applications in dermatology," *Med. Laser Appl.* **18**(3), pp. 249–259, 2003.

[13] M. Mogensen, G. B. E. Jemec, L. Thrane, T. M. Jørgensen, and P. E. Andersen, "OCT imaging of skin cancer and other dermatological diseases," *J. Biophotonics* **2**(6-7), pp. 442–451, 2009.

[14] R. K. Wang, J. B. Elder, and V. Smith, "High resolution imaging of colonic mucosa using optical coherence tomography," *Proc. SPIE* **4251**, pp. 242–246, 2001.

[15] J. A. Evans, J. M. Poneros, B. E. Bouma, J. Bressner, E. F. Halpern, M. Shishkov, G. Y. Lauwers, M. Mino-kenudson, N. S.

Nishioka, and G. J. Tearney, "Optical coherence tomography to identify intramucosal carcinoma and high-grade dysplasia in Barrett's esophagus," *Clin.l Gastroenterol. H.* **4**(1), p. 38, 2006.

[16] Y. Chen, A. D. Aguirre, P. L. Hsiung, S. Desai, P. R. Herz, M. Pedrosa, Q. Huang, M. Figueiredo, S.-W. Huang, A. Koski, J. M. Schmitt, J. G. Fujimoto, and H. Mashimo, "Ultrahigh resolution optical coherence tomography of Barrett's esophagus: preliminary descriptive clinical study correlating images with histology," *Endoscopy* **39**(7), p. 599, 2007.

[17] M. Tsuboi, A. Hayashi, N. Ikeda, H. Honda, Y. Kato, S. Ichinose, and H. Kato, "Optical coherence tomography in the diagnosis of bronchial lesions," *Lung Cancer* **49**(3), pp. 387–394, 2005.

[18] C. A. Jesser, S. A. Boppart, C. Pitris, D. L. Stamper, G. P. Nielsen, M. E. Brezinski, and J. G. Fujimoto, "High resolution imaging of transitional cell carcinoma with optical coherence tomography: feasibility for the evaluation of bladder pathology," *Brit. J. Radiol.* **72**(864), pp. 1170–1176, 1999.

[19] S. A. Boppart, M. E. Brezinski, B. E. Bouma, G. J. Tearney, and J. G. Fujimoto, "Investigation of developing embryonic morphology using optical coherence tomography," *Dev. Biol.* **177**(1), pp. 54–63, 1996.

[20] D. Stifter, "Beyond biomedicine: a review of alternative applications and developments for optical coherence tomography," *Appl. Phys. B–Lasers O.* **88**(3), pp. 337–357, 2007.

[21] M. R. Hee, D. Huang, E. A. Swanson, and J. G. Fujimoto, "Polarization-sensitive low-coherence reflectometer for birefringence characterization and ranging," *J. Opt. Soc. Am. B* **9**(6), pp. 903–908, 1992.

[22] J. A. Izatt, M. D. Kulkarni, S. Yazdanfar, J. K. Barton, and A. J. Welch, "In vivo bidirectional color Doppler flow imaging of picoliter blood volumes using optical coherence tomography," *Opt. Lett.* **22**, pp. 1439–1441, 1997.

[23] Z. Chen, T. E. Milner, D. Davé, and J. S. Nelson, "Optical Doppler tomographic imaging of fluid flow velocity in highly scattering media," *Opt. Lett.* **22**, pp. 64–66, 1997.

[24] J. M. Schmitt, "OCT elastography: imaging microscopic deformation and strain of tissue," *Opt. Express* **3**, pp. 199–211, 1998.

[25] C. Yang, "Molecular contrast optical coherence tomography: A review," *Photochem. Photobiol.* **81**(2), pp. 215–237, 2005.

[26] G. J. Tearney, M. E. Brezinski, J. F. Southern, B. E. Bouma, M. R. Hee, and J. G. Fujimoto, "Determination of the refractive index of highly scattering human tissue by optical coherence tomography," *Opt. Lett.* **20**, pp. 2258–2260, 1995.

[27] A. Knüttel and M. Boehlau-Godau, "Spatially confined and temporally resolved refractive index and scattering evaluation in human skin performed with optical coherence tomography," *J. Biomed. Opt.* **5**(1), pp. 83–92, 2000.

[28] J. A. Parrish, "New concepts in therapeutic photomedicine; photochemistry, optical targeting and the therapeutic window," *J. Invest. Dermatol.* **77**, pp. 45–50, 1981.

[29] J.-L. Boulnois, "Photophysical processes in recent medical laser developments: A review," *Laser Med. Sci.* **1**(1), pp. 47–66, 1986.

[30] J. M. Schmitt, A. Knüttel, M. Yadlowsky, and M. A. Eckhaus, "Optical-coherence tomography of a dense tissue: statistics of attenuation and backscattering," *Phys. Med. Biol.* **39**(10), pp. 1705–1720, 1994.

[31] A. Alex, B. Považay, B. Hofer, S. Popov, C. Glittenberg, S. Binder, and W. Drexler, "Multispectral in vivo three-dimensional optical coherence tomography of human skin," *J. Biomed. Opt.* **15**(2), p. 026025, 2010.

[32] B. Považay, K. Bizheva, B. Hermann, A. Unterhuber, H. Sattmann, A. F. Fercher, W. Drexler, C. Schubert, P. K. Ahnelt, M. Mei, R. Holzwarth, W. J. Wadsworth, J. C. Knight, and P. S. J. Russel, "Enhanced visualization of choroidal vessels using ultrahigh resolution ophthalmic OCT at 1050 nm," *Opt. Express* **11**(17), pp. 1980–1986, 2003.

[33] B. Považay, B. Hermann, A. Unterhuber, B. Hofer, H. Sattmann, F. Zeiler, J. E. Morgan, C. Falkner-Radler, C. Glittenberg, S. Blinder, and W. Drexler, "Three-dimensional optical coherence tomography at 1050 nm versus 800 nm in retinal pathologies: enhanced performance and choroidal penetration in cataract patients," *J. Biomed. Opt.* **12**(4), p. 041211, 2007.

[34] A. F. Fercher, C. K. Hitzenberger, G. Kamp, and S. Y. El-Zaiat, "Measurement of intraocular distances by backscattering spectral interferometry," *Opt. Commun.* **117**(1–2), pp. 43–48, 1995.

[35] M. A. Bail, G. Häusler, J. M. Herrmann, M. W. Lindner, and R. Ringler, "Optical coherence tomography with the "spectral radar": fast optical analysis in volume scatterers by short-coherence interferometry," *Proc. SPIE* **2925**, pp. 298–303, 1996.

[36] G. Häusler and M. W. Lindner, "'coherence radar' and 'spectral radar' – new tools for dermatological diagnosis," *J. Biomed. Opt.* **3**(1), pp. 21–31, 1998.

[37] B. Golubovic, B. E. Bouma, G. J. Tearney, and J. G. Fujimoto, "Optical frequency-domain reflectometry using rapid wavelength

tuning of a Cr^{4+}:forsterite laser," *Opt. Lett.* **22**(22), pp. 1704–1706, 1997.

[38] S. R. Chinn, E. A. Swanson, and J. G. Fujimoto, "Optical coherence tomography using a frequency-tunable optical source," *Opt. Lett.* **22**(5), pp. 340–342, 1997.

[39] B. E. Bouma, S.-H. Yun, B. J. Vakoc, M. J. Suter, and G. J. Tearney, "Fourier-domain optical coherence tomography: recent advances toward clinical utility," *Curr. Opin. Biotech.* **20**(1), pp. 111–118, 2009.

[40] M. A. Choma, K. Hsu, and J. A. Izatt, "Swept source optical coherence tomography using an all-fiber 1300-nm ring laser source," *J. Biomed. Opt.* **10**(4), p. 044009, 2005.

[41] R. Huber, M. Wojtkowski, and J. G. Fujimoto, "Fourier domain mode locking (FDML): a new laser operating regime and applications for optical coherence tomography," *Opt. Express* **14**(8), pp. 3225–3237, 2006.

[42] W. Wieser, B. R. Biedermann, T. Klein, C. M. Eigenwillig, and R. Huber, "Multi-megahertz OCT: High quality 3D imaging at 20 million A-scans and 4.5 Gvoxels per second," *Opt. Express* **18**(14), pp. 14685–14704, 2010.

[43] T. Klein, W. Wieser, C. M. Eigenwillig, B. R. Biedermann, and R. Huber, "Megahertz OCT for ultrawide-field retinal imaging with a 1050 nm Fourier domain mode-locked laser," *Opt. Express* **19**, pp. 3044–3062, 2011.

[44] S.-H. Yun, G. J. Tearney, J. F. de Boer, and B. E. Bouma, "Motion artifacts in optical coherence tomography with frequency-domain ranging," *Opt. Express* **12**(13), pp. 2977–2998, 2004.

[45] R. Huber, D. C. Adler, V. J. Srinivasan, and J. G. Fujimoto, "Fourier domain mode locking at 1050 nm for ultra-high-speed optical coherence tomography of the human retina at 236,000 axial scans per second," *Opt. Lett.* **32**(14), pp. 2049–2051, 2007.

[46] F. D. Nielsen, L. Thrane, K. Hsu, A. Bjarklev, and P. E. Andersen, "Semiconductor optical amplifier based swept wavelength source at 1060 nm using a scanning Fabry-Perot filter and an YDFA-based booster amplifier," *Opt. Commun.* **271**(1), pp. 197–202, 2007.

[47] M. K. Harduar, A. Mariampillai, B. Vuong, X. Gu, B. A. Standish, and V. X. D. Yang, "Dual-core ytterbium fiber amplifier for high-power 1060 nm swept source multichannel optical coherence tomography imaging," *Opt. Lett.* **36**, pp. 2976–2978, 2011.

[48] B. E. A. Saleh and M. C. Teich, *Fundamentals of Photonics, 2nd ed.*, Wiley, 2007.

[49] S. Machida and Y. Yamamoto, "Quantum-limited operation of balanced mixer homodyne and heterodyne receivers," *IEEE J. Quantum Elect.* **22**, pp. 617–624, 1986.

[50] A. G. Podoleanu, "Unbalanced versus balanced operation in an optical coherence tomography system," *Appl. Opt.* **39**, pp. 173–182, 2000.

[51] U. Haberland, W. Rütten, V. Blazek, and H. J. Schmitt, "Investigation of highly scattering media using near-infrared continuous wave tunable semiconductor laser," *Proc. SPIE* **2389**, pp. 503–512, 1995.

[52] B. R. Biedermann, W. Wieser, C. M. Eigenwillig, T. Klein, and R. Huber, "Direct measurement of the instantaneous linewidth of rapidly wavelength-swept lasers," *Opt. Lett.* **35**, pp. 3733–3735, 2010.

[53] T. von Niederhäusern, C. Meier, M. Duelk, and P. Vorreau, "Instantaneous coherence length measurement of a swept laser source using a mach-zehnder interferometer," *Proc. SPIE* **7889**, p. 78892R, 2011.

[54] T. Mitsui, "Dynamic range of optical reflectometry with spectral interferometry," *Jpn. J. Appl. Phys. 1* **38**(10), pp. 6133–6137, 1999.

[55] R. A. Leitgeb, C. K. Hitzenberger, A. F. Fercher, and T. Bajraszewski, "Phase-shifting algorithm to achieve high-speed long-depth-range probing by frequency-domain optical coherence tomography," *Opt. Lett.* **28**, pp. 2201–2203, 2003.

[56] S. Yun, G. Tearney, J. de Boer, and B. Bouma, "Removing the depth-degeneracy in optical frequency domain imaging with frequency shifting," *Opt. Express* **12**, pp. 4822–4828, 2004.

[57] M. Sarunic, M. A. Choma, C. Yang, and J. A. Izatt, "Instantaneous complex conjugate resolved spectral domain and swept-source oct using 3x3 fiber couplers," *Opt. Express* **13**, pp. 957–967, 2005.

[58] J. Zhang, J. S. Nelson, and Z. Chen, "Removal of a mirror image and enhancement of the signal-to-noise ratio in fourier-domain optical coherence tomography using an electro-optic phase modulator," *Opt. Lett.* **30**, pp. 147–149, 2005.

[59] Y. Yasuno, S. Makita, T. Endo, G. Aoki, M. Itoh, and T. Yatagai, "Simultaneous B-M-mode scanning method for real-time full-range fourier domain optical coherence tomography," *Appl. Opt.* **45**, pp. 1861–1865, 2006.

[60] B. Hofer, B. Považay, B. Hermann, A. Unterhuber, G. Matz, and W. Drexler, "Dispersion encoded full range frequency domain optical coherence tomography," *Opt. Express* **17**, pp. 7–24, 2009.

[61] C. Chong, T. Suzuki, K. Totsuka, A. Morosawa, and T. Sakai, "Large coherence length swept source for axial length measurement of the eye," *Appl. Opt.* **48**(10), pp. D144–50, 2009.

[62] M. Góra, K. Karnowski, M. Szkulmowski, B. J. Kaluzny, R. Huber, A. Kowalczyk, and M. Wojtkowski, "Ultra high-speed swept source oct imaging of the anterior segment of human eye at 200 khz with adjustable imaging range," *Opt. Express* **17**, pp. 14880–14894, 2009.

[63] B. R. Biedermann, W. Wieser, C. M. Eigenwillig, T. Klein, and R. Huber, "Dispersion, coherence and noise of Fourier domain mode locked lasers," *Opt. Express* **17**(12), pp. 9947–9961, 2009.

[64] D. C. Adler, W. Wieser, F. Trepanier, J. M. Schmitt, and R. A. Huber, "Extended coherence length Fourier domain mode locked lasers at 1310 nm," *Opt. Express* **19**, pp. 20930–20939, 2011.

[65] W. Drexler, U. Morgner, F. X. Kärtner, C. Pitris, S. A. Boppart, X. D. Li, E. P. Ippen, and J. G. Fujimoto, "In vivo ultrahigh-resolution optical coherence tomography," *Opt. Lett.* **24**, pp. 1221–1223, 1999.

[66] I. Hartl, X. D. Li, C. Chudoba, R. K. Ghanta, T. H. Ko, J. G. Fujimoto, J. K. Ranka, and R. S. Windeler, "Ultrahigh-resolution optical coherence tomography using continuum generation in an air–silica microstructure optical fiber," *Opt. Lett.* **26**(9), pp. 608–610, 2001.

[67] B. Považay, K. Bizheva, A. Unterhuber, B. Hermann, H. Sattmann, A. F. Fercher, W. Drexler, A. Apolonski, W. J. Wadsworth, J. C. Knight, P. S. J. Russell, M. Vetterlein, and E. Scherzer, "Submicrometer axial resolution optical coherence tomography," *Opt. Lett.* **27**(20), pp. 1800–1802, 2002.

[68] W. Drexler, "Ultrahigh-resolution optical coherence tomography," *J. Biomed. Opt.* **9**(1), pp. 47–74, 2004.

[69] S. Inoué, *Handbook of Biological Confocal Microscopy*, ch. 1. Springer Science+Business Media, LLC, 3 ed., 2006. ISBN: 978-0-387-25921-5.

[70] V. X. D. Yang, N. Munce, J. Pekar, M. L. Gordon, S. Lo, N. E. Marcon, B. C. Wilson, and I. A. Vitkin, "Micromachined array tip for multifocus fiber-based optical coherencetomography," *Opt. Lett.* **29**, pp. 1754–1756, 2004.

[71] J. Holmes, S. Hattersley, N. Stone, F. Bazant-Hegemark, and H. Barr, "Multi-channel fourier domain OCT system with superior lateral resolution for biomedical applications," *Proc. SPIE* **6847**, p. 68470O, 2008.

[72] J. A. Izatt, M. R. Hee, G. M. Owen, E. A. Swanson, and J. G. Fujimoto, "Optical coherence microscopy in scattering media," *Opt. Lett.* **19**, pp. 590–592, 1994.

[73] B. Potsaid, I. Gorczynska, V. J. Srinivasan, Y. Chen, J. Jiang, A. Cable, and J. G. Fujimoto, "Ultrahigh speed spectral / Fourier domain OCT ophthalmic imaging at 70,000 to 312,500 axial scans per second," *Opt. Express* **16**, pp. 15149–15169, 2008.

[74] K. Bizheva, R. Pflug, B. Hermann, B. Považay, H. Sattmann, P. Qiu, E. Angers, H. Reitsamer, S. Popov, J. R. Taylor, A. Unterhuber, P. Ahnelt, and W. Drexler, "Optophysiology: Depth-resolved probing of retinal physiology with functional ultrahigh-resolution optical coherence tomography," *P. Natl. Acad. Sci. USA* **103**(13), 2006.

[75] R. A. Leitgeb, T. Schmoll, and C. Kolbitsch, "Dynamic retinal optical coherence microscopy without adaptive optics," *Proc. SPIE* **7372**, p. 737208, 2009.

[76] C. K. Hitzenberger, A. Baumgartner, W. Drexler, and A. F. Fercher, "Dispersion effects in partial coherence interferometry: Implications for intraocular ranging," *J. Biomed. Opt.* **4**(1), pp. 144–151, 1999.

[77] J. F. de Boer, C. E. Saxer, and J. S. Nelson, "Stable carrier generation and phase-resolved digital data processing in optical coherence tomography," *Appl. Opt.* **40**, pp. 5787–5790, 2001.

[78] M. Wojtkowski, V. Srinivasan, T. Ko, J. Fujimoto, A. Kowalczyk, and J. Duker, "Ultrahigh-resolution, high-speed, Fourier domain optical coherence tomography and methods for dispersion compensation," *Opt. Express* **12**, pp. 2404–2422, 2004.

[79] M. E. Brezinski, G. J. Tearney, B. E. Bouma, J. A. Izatt, M. R. Hee, E. A. Swanson, J. F. Southern, and J. G. Fujimoto, "Optical coherence tomography for optical biopsy: Properties and demonstration of vascular pathology," *Circulation* **93**(6), pp. 1206–1213, 1996.

[80] B. Wilson and S. Jacques, "Optical reflectance and transmittance of tissues: principles and applications," *Quantum Electronics, IEEE Journal of* **26**, pp. 2186–2199, 1990.

[81] A. F. Fercher, B. Sander, T. M. Jørgensen, and P. E. Andersen, *Encyclopedia of Analytical Chemistry*, p. 34. John Wiley & Sons, Ltd, 2009.

[82] K. F. Palmer and D. Williams, "Optical properties of water in the near infrared," *J. Opt. Soc. Am.* **64**, pp. 1107–1110, 1974.

[83] M. L. Wolbarsht, A. W. Walsh, and G. George, "Melanin, a unique biological absorber," *Appl. Opt.* **20**, pp. 2184–2186, 1981.

[84] P. Parsa, S. L. Jacques, and N. S. Nishioka, "Optical properties of rat liver between 350 and 2200 nm," *Appl. Opt.* **28**, pp. 2325–2330, 1989.

[85] S. J. Matcher, M. Cope, and D. T. Delpy, "In vivo measurements of the wavelength dependence of tissue-scattering coefficients between 760 and 900 nm measured with time-resolved spectroscopy," *Appl. Opt.* **36**, pp. 386–396, 1997.

[86] S. Srinivasan, B. W. Pogue, S. Jiang, H. Dehghani, C. Kogel, S. Soho, J. J. Gibson, T. D. Tosteson, S. P. Poplack, and K. D. Paulsen, "Interpreting hemoglobin and water concentration, oxygen saturation, and scattering measured in vivo by near-infrared breast tomography," *P. Natl. Acad. Sci. USA* **100**(21), pp. 12349–12354, 2003.

[87] U. Sharma, E. W. Chang, and S. H. Yun, "Long-wavelength optical coherence tomography at 1.7 μm for enhanced imaging depth," *Opt. Express* **16**, pp. 19712–19723, 2008.

[88] B. R. Biedermann, W. Wieser, C. M. Eigenwillig, and R. Huber, "Recent developments in fourier domain mode locked lasers for optical coherence tomography: Imaging at 1310 nm vs. 1550 nm wavelength," *J. Biophotonics* **2**(6-7), pp. 357–363, 2009.

[89] T. J. van den Berg and H. Spekreijse, "Near infrared light absorption in the human eye media," *Vis. Res.* **37**(2), pp. 249–253, 1997.

[90] A. Unterhuber, B. Považay, B. Hermann, H. Sattmann, A. Chavez-Pirson, and W. Drexler, "In vivo retinal optical coherence tomography at 1040 nm - enhanced penetration into the choroid," *Opt. Express* **13**(9), pp. 3252–3258, 2005.

[91] Y. Wang, J. S. Nelson, Z. Chen, B. J. Reiser, R. S. Chuck, and R. S. Windeler, "Optimal wavelength for ultrahigh-resolution op-

tical coherence tomography," *Opt. Express* **11**(12), pp. 1411–1417, 2003.

[92] J. M. Schmitt, S. H. Xiang, and K. M. Yung, "Speckle in optical coherence tomography," *J. Biomed. Opt.* **4**(1), pp. 95–105, 1999.

[93] K. W. Gossage, T. S. Tkaczyk, J. J. Rodriguez, and J. K. Barton, "Texture analysis of optical coherence tomography images: feasibility for tissue classification," *J. Biomed. Opt.* **8**(3), pp. 570–575, 2003.

[94] T. R. Hillman, S. G. Adie, V. Seemann, J. J. Armstrong, S. L. Jacques, and D. D. Sampson, "Correlation of static speckle with sample properties in optical coherence tomography," *Opt. Lett.* **31**, pp. 190–192, 2006.

[95] J. M. Schmitt, "Array detection for speckle reduction in optical coherence microscopy," *Phys. Med. Biol.* **42**(7), pp. 1427–1439, 1997.

[96] B. Sander, M. Larsen, L. Thrane, J. L. Hougaard, and T. M. Jørgensen, "Enhanced optical coherence tomography imaging by multiple scan averaging," *Brit. J. Ophthalmol.* **89**(2), pp. 207–212, 2005.

[97] T. M. Jørgensen, J. Thomadsen, U. Christensen, W. Soliman, and B. Sander, "Enhancing the signal-to-noise ratio in ophthalmic optical coherence tomography by image registration—method and clinical examples," *J. Biomed. Opt.* **12**(4), p. 041208, 2007.

[98] M. Pircher, E. Götzinger, R. Leitgeb, A. F. Fercher, and C. K. Hitzenberger, "Speckle reduction in optical coherence tomography by frequency compounding," *J. Biomed. Opt.* **8**(3), pp. 565–569, 2003.

[99] M. D. Kulkarni, C. W. Thomas, and J. A. Izatt, "Image enhancement in optical coherence tomography using deconvolution," *Electron. Lett.* **33**, pp. 1365–1367, 1997.

[100] J. M. Schmitt, "Restoration of optical coherence images of living tissue using the CLEAN algorithm," *J. Biomed. Opt.* **3**(1), pp. 66–75, 1998.

[101] S. H. Xiang, L. Zhou, and J. M. Schmitt, "Speckle noise reduction for optical coherence tomography," *Proc. SPIE* **3196**(1), pp. 79–88, 1998.

[102] J. Rogowska and M. E. Brezinski, "Evaluation of the adaptive speckle suppression filter for coronary optical coherence tomography imaging," *IEEE T. Med. Imaging* **19**, pp. 1261–1266, 2000.

[103] R. K. Wang, "Reduction of speckle noise for optical coherence tomography by the use of nonlinear anisotropic diffusion," *Proc. SPIE* **5690**(1), pp. 380–385, 2005.

[104] J. F. de Boer, T. E. Milner, M. J. C. van Gemert, and J. S. Nelson, "Two-dimensional birefringence imaging in biological tissue by polarization-sensitive optical coherence tomography," *Opt. Lett.* **22**, pp. 934–936, 1997.

[105] A. Baumgartner, S. Dichtl, C. K. Hitzenberger, H. Sattmann, B. Robl, A. Moritz, A. F. Fercher, and W. Sperr, "Polarization-sensitive optical coherence tomography of dental structures," *Caries Res.* **34**(1), pp. 59–69, 2000.

[106] N. Kemp, H. Zaatari, J. Park, H. G. R. III, and T. Milner, "Form-biattenuance in fibrous tissues measured with polarization-sensitive optical coherence tomography (PS-OCT)," *Opt. Express* **13**, pp. 4611–4628, 2005.

[107] M. Pircher, E. Götzinger, R. Leitgeb, H. Sattmann, O. Findl, and C. Hitzenberger, "Imaging of polarization properties of human retina in vivo with phase resolved transversal PS-OCT," *Opt. Express* **12**, pp. 5940–5951, 2004.

[108] J. F. de Boer, T. E. Milner, and J. S. Nelson, "Determination of the depth-resolved Stokes parameters of light backscattered from turbid media by use of polarization-sensitive optical coherence tomography," *Opt. Lett.* **24**, pp. 300–302, 1999.

[109] G. Yao and L. V. Wang, "Two-dimensional depth-resolved Mueller matrix characterization of biological tissue by optical coherence tomography," *Opt. Lett.* **24**, pp. 537–539, 1999.

[110] S. Jiao and L. V. Wang, "Jones-matrix imaging of biological tissues with quadruple-channel optical coherence tomography," *J. Biomed. Opt.* **7**(3), pp. 350–358, 2002.

[111] C. K. Hitzenberger, E. Götzinger, M. Sticker, M. Pircher, and A. F. Fercher, "Measurement and imaging of birefringence and optic axis orientation by phase resolved polarization sensitive optical coherence tomography," *Opt. Express* **9**(13), pp. 780–790, 2001.

[112] E. Götzinger, M. Pircher, W. Geitzenauer, C. Ahlers, B. Baumann, S. Michels, U. Schmidt-Erfurth, and C. K. Hitzenberger, "Retinal pigment epithelium segmentation by polarization sensitive optical coherence tomography," *Opt. Express* **16**, pp. 16410–16422, 2008.

[113] D. Stifter, P. Burgholzer, O. Höglinger, E. Götzinger, and C. Hitzenberger, "Polarisation-sensitive optical coherence tomography for material characterisation and strain-field mapping," *Applied Physics A: Materials Science & Processing* **76**, pp. 947–951, 2003. 10.1007/s00339-002-2065-5.

[114] Y. Zhao, Z. Chen, C. Saxer, S. Xiang, J. F. de Boer, and J. S. Nelson, "Phase-resolved optical coherence tomography and optical

Doppler tomography for imaging blood flow in human skin with fast scanning speed and high velocity sensitivity," *Opt. Lett.* **25**, pp. 114–116, 2000.

[115] C. Sun, B. Standish, and V. X. D. Yang, "Optical coherence elastography: current status and future applications," *J. Biomed. Opt.* **16**(4), p. 043001, 2011.

[116] R. Chan, A. Chau, W. Karl, S. Nadkarni, A. Khalil, N. Iftimia, M. Shishkov, G. Tearney, M. Kaazempur-Mofrad, and B. Bouma, "OCT-based arterial elastography: robust estimation exploiting tissue biomechanics," *Opt. Express* **12**, pp. 4558–4572, 2004.

[117] J. Rogowska, N. Patel, S. Plummer, and M. E. Brezinski, "Quantitative optical coherence tomographic elastography: method for assessing arterial mechanical properties," *Br J Radiol* **79**(945), pp. 707–711, 2006.

[118] R. K. Wang, Z. Ma, and S. J. Kirkpatrick, "Tissue Doppler optical coherence elastography for real time strain rate and strain mapping of soft tissue," *Appl. Phys. Lett.* **89**(14), p. 144103, 2006.

[119] S. J. Kirkpatrick, R. K. Wang, and D. D. Duncan, "OCT-based elastography for large and small deformations," *Opt. Express* **14**, pp. 11585–11597, 2006.

[120] X. Liang, A. L. Oldenburg, V. Crecea, E. J. Chaney, and S. A. Boppart, "Optical micro-scale mapping of dynamic biomechanical tissue properties," *Opt. Express* **16**, pp. 11052–11065, 2008.

[121] S. G. Adie, B. F. Kennedy, J. J. Armstrong, S. A. Alexandrov, and D. D. Sampson, "Audio frequency in vivo optical coherence elastography," *Phys. Med. Biol.* **54**(10), pp. 3129–3139, 2009.

[122] S. A. Boppart, A. L. Oldenburg, C. Xu, and D. L. Marks, "Optical probes and techniques for molecular contrast enhancement in coherence imaging," *J. Biomed. Opt.* **10**(4), p. 041208, 2005.

[123] U. Morgner, W. Drexler, F. X. Kärtner, X. D. Li, C. Pitris, E. P. Ippen, and J. G. Fujimoto, "Spectroscopic optical coherence tomography," *Opt. Lett.* **25**, pp. 111–113, 2000.

[124] D. J. Faber, E. G. Mik, M. C. G. Aalders, and T. G. van Leeuwen, "Light absorption of (oxy-)hemoglobin assessed by spectroscopic optical coherence tomography," *Opt. Lett.* **28**, pp. 1436–1438, 2003.

[125] J. M. Schmitt, S. H. Xiang, and K. M. Yung, "Differential absorption imaging with optical coherence tomography," *J. Opt. Soc. Am. A* **15**, pp. 2288–2296, 1998.

[126] C.-W. Lu, C.-K. Lee, M.-T. Tsai, Y.-M. Wang, and C. C. Yang, "Measurement of the hemoglobin oxygen saturation level with spectroscopic spectral-domain optical coherence tomography," *Opt. Lett.* **33**, pp. 416–418, 2008.

[127] C. Vinegoni, J. Bredfeldt, D. Marks, and S. Boppart, "Nonlinear optical contrast enhancement for optical coherence tomography," *Opt. Express* **12**, pp. 331–341, 2004.

[128] J. S. Bredfeldt, C. Vinegoni, D. L. Marks, and S. A. Boppart, "Molecularly sensitive optical coherence tomography," *Opt. Lett.* **30**, pp. 495–497, 2005.

[129] T. Støren, A. Simonsen, O. J. Løkberg, T. Lindmo, L. O. Svaasand, and A. Røyset, "Measurement of dye diffusion in agar gel by use of low-coherence interferometry," *Opt. Lett.* **28**, pp. 1215–1217, 2003.

[130] K. D. Rao, M. A. Choma, S. Yazdanfar, A. M. Rollins, and J. A. Izatt, "Molecular contrast in optical coherence tomography by use of a pump probe technique," *Opt. Lett.* **28**, pp. 340–342, 2003.

[131] J. K. Barton, J. B. Hoying, and C. J. Sullivan, "Use of microbubbles as an optical coherence tomography contrast agent," *Acad. Radiol.* **9**(suppl 1), pp. 52–55, 2002.

[132] T. M. Lee, A. L. Oldenburg, S. Sitafalwalla, D. L. Marks, W. Luo, F. J.-J. Toublan, K. S. Suslick, and S. A. Boppart, "Engineered microsphere contrast agents for optical coherence tomography," *Opt. Lett.* **28**, pp. 1546–1548, 2003.

[133] J. K. Barton, N. J. Halas, J. L. West, and R. A. Drezek, "Nanoshells as an optical coherence tomography contrast agent," *Proc. SPIE* **5316**, pp. 99–106, 2004.

[134] T. S. Troutman, J. K. Barton, and M. Romanowski, "Optical coherence tomography with plasmon resonant nanorods of gold," *Opt. Lett.* **32**, pp. 1438–1440, 2007.

[135] A. M. Winkler, P. F. S. Rice, R. A. Drezek, and J. K. Barton, "Quantitative tool for rapid disease mapping using optical coherence tomography images of azoxymethane-treated mouse colon," *J. Biomed. Opt.* **15**(4), p. 041512, 2010.

[136] D. Levitz, L. Thrane, M. Frosz, P. Andersen, C. Andersen, S. Andersson-Engels, J. Valanciunaite, J. Swartling, and P. Hansen, "Determination of optical scattering properties of highly-scattering media in optical coherence tomography images," *Opt. Express* **12**, pp. 249–259, 2004.

[137] I. V. Turchin, E. A. Sergeeva, L. S. Dolin, V. A. Kamensky, N. M. Shakhova, and R. Richards-Kortum, "Novel algorithm of processing optical coherence tomography images for differentiation of biological tissue pathologies," *J. Biomed. Opt.* **10**(6), p. 064024, 2005.

[138] F. J. van der Meer, D. J. Faber, D. M. B. Sassoon, M. C. Aalders, G. Pasterkamp, and T. G. van Leeuwen, "Localized measurement of optical attenuation coefficients of atherosclerotic plaque constituents by quantitative optical coherence tomography," *IEEE T. Med. Imaging* **24**, pp. 1369–1376, 2005.

[139] M. Sowa, D. Popescu, J. Werner, M. Hewko, A. Ko, J. Payette, C. Dong, B. Cleghorn, and L.-P. Choo-Smith, "Precision of Raman depolarization and optical attenuation measurements of sound tooth enamel," *Anal. Bioanal. Chem.* **387**, pp. 1613–1619, 2007. 10.1007/s00216-006-0856-9.

[140] G. van Soest, T. Goderie, E. Regar, S. Koljenović, G. L. J. H. van Leenders, N. Gonzalo, S. van Noorden, T. Okamura, B. E. Bouma, G. J. Tearney, J. W. Oosterhuis, P. W. Serruys, and A. F. W. van der Steen, "Atherosclerotic tissue characterization in vivo by optical coherence tomography attenuation imaging," *J. Biomed. Opt.* **15**(1), p. 011105, 2010.

[141] R. A. McLaughlin, L. Scolaro, P. Robbins, C. Saunders, S. L. Jacques, and D. D. Sampson, "Parametric imaging of cancer with optical coherence tomography," *J. Biomed. Opt.* **15**(4), p. 046029, 2010.

[142] A. F. Fercher, C. K. Hitzenberger, W. Drexler, G. Kamp, and H. Sattmann, "In vivo optical coherence tomography," *Am. J. Ophthalmol.* **116**(1), pp. 113–114, 1993.

[143] E. A. Swanson, J. A. Izatt, M. R. Hee, D. Huang, C. P. Lin, J. S. Schuman, C. A. Puliafito, and J. G. Fujimoto, "In vivo retinal imaging by optical coherence tomography," *Opt. Lett.* **18**, pp. 1864–1866, 1993.

[144] J. A. Izatt, M. R. Hee, D. Huang, J. G. Fujimoto, E. A. Swanson, C. P. Lin, J. S. Shuman, and C. A. Puliafito, "Ophthalmic diag-

nostics using optical coherence tomography," *Proc. SPIE* **1877**, pp. 136–144, 1993.

[145] P. K. Kaiser, B. A. Blodi, H. Shapiro, and N. R. Acharya, "Angiographic and optical coherence tomographic results of the marina study of ranibizumab in neovascular age-related macular degeneration," *Ophthalmology* **114**(10), pp. 1868–1875, 2007.

[146] W. Soliman, B. Sander, K. A. E.-N. Soliman, S. Yehya, M. S. A. Rahamn, and M. Larsen, "The predictive value of optical coherence tomography after grid laser photocoagulation for diffuse diabetic macular oedema," *Acta Ophthalmol.* **86**(3), pp. 284–291, 2008.

[147] D. Gaucher, C. Sebah, A. Erginay, B. Haouchine, R. Tadayoni, A. Gaudric, and P. Massin, "Optical coherence tomography features during the evolution of serous retinal detachment in patients with diabetic macular edema," *Am. J. Ophthalmol.* **145**(2), pp. 289–296, 2008.

[148] O. Tan, G. Li, A. T.-H. Lu, R. Varma, and D. Huang, "Mapping of macular substructures with optical coherence tomography for glaucoma diagnosis," *Ophthalmology* **115**(6), pp. 949–956, 2008.

[149] J. Larsson, K. Holm, and M. Lövestam-Adrian, "The presence of an operculum verified by optical coherence tomography and other prognostic factors in macular hole surgery," *Acta Ophthalmol. Scan.* **84**(3), pp. 301–304, 2006.

[150] I. Kovacs, M. Ferencz, J. Nemes, G. Somfai, G. Salacz, and Z. Recsan, "Intraocular lens power calculation for combined cataract surgery, vitrectomy and peeling of epiretinal membranes for macular oedema," *Acta Ophthalmol. Scan.* **85**(1), pp. 88–91, 2007.

[151] M. Doors, T. T. J. M. Berendschot, J. de Brabander, C. A. B. Webers, and R. M. M. A. Nuijts, "Value of optical coherence tomog-

raphy for anterior segment surgery," *J. Cataract Refr. Surg.* **36**(7), pp. 1213–1229, 2010.

[152] M. Kalev-Landoy, A. C. Day, M. F. Cordeiro, and C. Migdal, "Optical coherence tomography in anterior segment imaging," *Acta Ophthalmol. Scan.* **85**(4), pp. 427–430, 2007.

[153] S. H. Yun, G. J. Tearney, B. J. Vakoc, M. Shishkov, W. Y. Oh, A. E. Desjardins, M. J. Suter, R. C. Chan, J. A. Evans, I.-K. Jang, N. S. Nishioka, J. F. de Boer, and B. E. Bouma, "Comprehensive volumetric optical microscopy in vivo.," *Nat. Med.* **12**(12), pp. 1429–1433, 2006.

[154] I.-K. Jang, B. E. Bouma, D.-H. Kang, S.-J. Park, S.-W. Park, K.-B. Seung, K.-B. Choi, M. Shishkov, K. Schlendorf, E. Pomerantsev, S. L. Houser, H. T. Aretz, and G. J. Tearney, "Visualization of coronary atherosclerotic plaques in patients using optical coherence tomography: Comparison with intravascular ultrasound," *J. Am. Coll. Cardiol.* **39**(4), pp. 604–609, 2002.

[155] G. J. Tearney, H. Yabushita, S. L. Houser, H. T. Aretz, I.-K. Jang, K. H. Schlendorf, C. R. Kauffman, M. Shishkov, E. F. Halpern, and B. E. Bouma, "Quantification of macrophage content in atherosclerotic plaques by optical coherence tomography.," *Circulation* **107**(1), pp. 113–119, 2003.

[156] I.-K. Jang, G. J. Tearney, B. MacNeill, M. Takano, F. Moselewski, N. Iftima, M. Shishkov, S. Houser, H. T. Aretz, E. F. Halpern, and B. E. Bouma, "In vivo characterization of coronary atherosclerotic plaque by use of optical coherence tomography," *Circulation* **111**(12), pp. 1551–1555, 2005.

[157] T. Kume, T. Akasaka, T. Kawamoto, H. Okura, N. Watanabe, E. Toyota, Y. Neishi, R. Sukmawan, Y. Sadahira, and K. Yoshida,

"Measurement of the thickness of the fibrous cap by optical coherence tomography," *Am. Heart J.* **152**(4), pp. 755.e1–e4, 2006.

[158] S. D. Giattina, B. K. Courtney, P. R. Herz, M. Harman, S. Shortkroff, D. L. Stamper, B. Liu, J. G. Fujimoto, and M. E. Brezinski, "Assessment of coronary plaque collagen with polarization sensitive optical coherence tomography (PS-OCT)," *Int. J. Cardiol.* **107**(3), pp. 400–409, 2006.

[159] S. K. Nadkarni, M. C. Pierce, B. H. Park, J. F. de Boer, P. Whittaker, B. E. Bouma, J. E. Bressner, E. Halpern, S. L. Houser, and G. J. Tearney, "Measurement of collagen and smooth muscle cell content in atherosclerotic plaques using polarization-sensitive optical coherence tomography," *J. Am. Coll. Cardiol.* **49**(13), pp. 1474–1481, 2007.

[160] L. J. Diaz-Sandoval, B. E. Bouma, G. J. Tearney, and I.-K. Jang, "Optical coherence tomography as a tool for percutaneous coronary interventions," *Catheter. Cardio. Inte.* **65**(4), pp. 492–496, 2005.

[161] B. E. Bouma, G. J. Tearney, H. Yabushita, M. Shishkov, C. R. Kauffman, D. DeJoseph Gauthier, B. D. MacNeill, S. L. Houser, H. T. Aretz, E. F. Halpern, and I.-K. Jang, "Evaluation of intracoronary stenting by intravascular optical coherence tomography," *Heart* **89**(3), pp. 317–320, 2003.

[162] G. Guagliumi and V. Sirbu, "Optical coherence tomography: High resolution intravascular imaging to evaluate vascular healing after coronary stenting," *Catheter. Cardio. Inte.* **72**(2), p. 237, 2008.

[163] N. Gonzalo, P. W. Serruys, T. Okamura, Z. J. Shen, Y. Onuma, H. M. Garcia-Garcia, G. Sarno, C. Schultz, R. J. van Geuns, J. Ligthart, and E. Regar, "Optical coherence tomography assessment of the acute effects of stent implantation on the vessel wall: a

systematic quantitative approach," *Heart* **95**(23), pp. 1913–1919, 2009.

[164] A. Murata, D. Wallace-Bradley, A. Tellez, C. Alviar, M. Aboodi, A. Sheehy, L. Coleman, L. Perkins, G. Nakazawa, G. Mintz, G. L. Kaluza, R. Virmani, and J. F. Granada, "Accuracy of optical coherence tomography in the evaluation of neointimalcoverage after stent implantation," *J. Am. Coll. Cardiol. Img.* **3**(1), pp. 76–84, 2010.

[165] Y. Ozaki, M. Okumura, T. F. Ismail, H. Naruse, K. Hattori, S. Kan, M. Ishikawa, T. Kawai, Y. Takagi, J. Ishii, F. Prati, and P. W. Serruys, "The fate of incomplete stent apposition with drug-eluting stents: an optical coherence tomography-based natural history study," *Eur. Heart J.* **31**(12), pp. 1470–1476, 2010.

[166] M. Mogensen, B. M. Nürnberg, J. L. Forman, J. B. Thomsen, L. Thrane, and G. B. E. Jemec, "In vivo thickness measurement of basal cell carcinoma and actinic keratosis with optical coherence tomography and 20-MHz ultrasound," *Brit. J. Dermatol.* **160**(5), pp. 1026–1033, 2009.

[167] J. Welzel, "Optical coherence tomography in dermatology: A review," *Skin Res. Technol.* **7**(1), pp. 1–9, 2001.

[168] T. Gambichler, A. Orlikov, R. Vasa, G. Moussa, K. Hoffmann, M. Stücker, P. Altmeyer, and F. G. Bechara, "In vivo optical coherence tomography of basal cell carcinoma," *J. Dermatol. Sci.* **45**(3), pp. 167–173, 2007.

[169] M. Mogensen, H. A. Morsy, L. Thrane, and G. B. E. Jemec, "Morphology and epidermal thickness of normal skin imaged by optical coherence tomography," *Dermatology* **217**(1), pp. 14–20, 2008.

[170] T. Gambichler, P. Regeniter, F. G. Bechara, A. Orlikov, R. Vasa, G. Moussa, M. Stücker, P. Altmeyer, and K. Hoffmann, "Char-

acterization of benign and malignant melanocytic skin lesions using optical coherence tomography in vivo," *J. Am. Acad. Dermatol.* **57**(4), pp. 629–637, 2007.

[171] M. Mogensen, T. M. Jørgensen, B. M. Nürnberg, H. A. Morsy, J. B. Thomsen, L. Thrane, and G. B. E. Jemec, "Assessment of optical coherence tomography imaging in the diagnosis of non-melanoma skin cancer and benign lesions versus normal skin: Observer-blinded evaluation by dermatologists and pathologists," *Dermatol. Surg.* **35**(6), pp. 965–972, 2009.

[172] J. G. Fujimoto, M. E. Brezinski, G. J. Tearney, S. A. Boppart, B. Bouma, M. R. Hee, J. F. Southern, and E. A. Swanson, "Optical biopsy and imaging using optical coherence tomography," *Nat. Med.* **1**(9), pp. 970–972, 1995.

[173] G. J. Tearney, M. E. Brezinski, B. E. Bouma, S. A. Boppart, C. Pitris, J. F. Southern, and J. G. Fujimoto, "In vivo endoscopic optical biopsy with optical coherence tomography," *Science* **276**(5321), pp. 2037–2039, 1997.

[174] X. Li, C. Chudoba, T. Ko, C. Pitris, and J. G. Fujimoto, "Imaging needle for optical coherence tomography," *Opt. Lett.* **25**, pp. 1520–1522, 2000.

[175] S. A. Boppart, W. Luo, D. L. Marks, and K. W. Singletary, "Optical coherence tomography: Feasibility for basic research and image-guided surgery of breast cancer," *Breast Cancer Res. Tr.* **84**(2), pp. 85–97, 2004.

[176] B. A. Standish, X. Jin, J. Smolen, A. Mariampillai, N. R. Munce, B. C. Wilson, I. A. Vitkin, and V. X. D. Yang, "Interstitial Doppler optical coherence tomography monitors microvascular changes during photodynamic therapy in a Dunning prostate model under

varying treatment conditions," *J. Biomed. Opt.* **12**(3), p. 034022, 2007.

[177] S. A. Boppart, B. E. Bouma, C. Pitris, G. J. Tearney, J. G. Fujimoto, and M. E. Brezinski, "Forward-imaging instruments for optical coherence tomography," *Opt. Lett.* **22**, pp. 1618–1620, 1997.

[178] X. Li, S. Martin, C. Pitris, R. Ghanta, D. Stamper, M. Harman, J. Fujimoto, and M. Brezinski, "High-resolution optical coherence tomographic imaging of osteoarthritic cartilage during open knee surgery," *Arthritis Res. Ther.* **7**(2), pp. R318–R323, 2005.

[179] K. Zheng, S. D. Martin, C. H. Rashidifard, B. Liu, and M. E. Brezinski, "In vivo micron-scale arthroscopic imaging of human knee osteoarthritis with optical coherence tomography: comparison with magnetic resonance imaging and arthroscopy," *Am. J. Orthop.* **39**(3), pp. 122–125, 2010.

[180] R. A. McLaughlin, L. Scolaro, P. Robbins, S. Hamza, C. Saunders, and D. D. Sampson, "Imaging of human lymph nodes using optical coherence tomography: Potential for staging cancer," *Cancer Res.* **70**(7), pp. 2579–2584, 2010.

[181] F. T. Nguyen, A. M. Zysk, E. J. Chaney, S. G. Adie, J. G. Kotynek, U. J. Oliphant, F. J. Bellafiore, K. M. Rowland, P. A. Johnson, and S. A. Boppart, "Optical coherence tomography: The intraoperative assessment of lymph nodes in breast cancer," *IEEE Eng. Med. Biol.* **29**(2), pp. 63–70, 2010.

[182] S. A. Boppart, G. J. Tearney, B. E. Bouma, J. F. Southern, M. E. Brezinski, and J. G. Fujimoto, "Noninvasive assessment of the developing xenopus cardiovascular system using optical coherence tomography," *P. Natl. Acad. Sci. USA* **94**(9), pp. 4256–4261, 1997.

[183] A. Mariampillai, B. A. Standish, N. R. Munce, C. Randall, G. Liu, J. Y. Jiang, A. E. Cable, I. A. Vitkin, and V. X. D. Yang, "Doppler

optical cardiogram gated 2D color flow imaging at 1000 fps and 4D in vivo visualization of embryonic heart at 45 fps on a swept source OCT system," *Opt. Express* **15**, pp. 1627–1638, 2007.

[184] T. M. Yelbuz, M. A. Choma, L. Thrane, M. L. Kirby, and J. A. Izatt, "Optical coherence tomography: A new high-resolution imaging technology to study cardiac development in chick embryos," *Circulation* **106**(22), p. 2771, 2002.

[185] M. W. Jenkins, D. C. Adler, M. Gargesha, R. Huber, F. Rothenberg, J. Belding, M. Watanabe, D. L. Wilson, J. G. Fujimoto, and A. M. Rollins, "Ultrahigh-speed optical coherence tomography imaging and visualization of the embryonic avian heart using a buffered fourier domain mode locked laser," *Opt. Express* **15**(10), pp. 6251–6267, 2007.

[186] K. Norozi, L. Thrane, J. Männer, F. Pedersen, I. Wolf, S. Mottl-Link, H.-P. Meinzer, A. Wessel, and T. M. Yelbuz, "In vivo visualisation of coronary artery development by high-resolution optical coherence tomography," *Heart* **94**(2), p. 130, 2008.

[187] J. Männer, L. Thrane, K. Norozi, and T. M. Yelbuz, "In vivo imaging of the cyclic changes in cross-sectional shape of the ventricular segment of pulsating embryonic chick hearts at stages 14 to 17: A contribution to the understanding of the ontogenesis of cardiac pumping function," *Dev. Dynam.* **238**(12), pp. 3273–3284, 2009.

[188] W. Luo, D. L. Marks, T. S. Ralston, and S. A. Boppart, "Three-dimensional optical coherence tomography of the embryonic murine cardiovascular system," *J. Biomed. Opt.* **11**(2), pp. 021014–8, 2006.

[189] P. Targowski, M. Góra, and M. Wojtkowski, "Optical coherence tomography for artwork diagnostics," *Laser Chem.* **2006**, 2006.

[190] M. Kuznetsov, W. Atia, B. Johnson, and D. Flanders, "Compact ultrafast reflective Fabry-Perot tunable lasers for OCT imaging applications," *Proc. SPIE* **7554**, pp. 75541F–6, 2010.

[191] F. Harris, "On the use of windows for harmonic analysis with the discrete Fourier transform," *Proc. IEEE* **66**, pp. 51–83, 1978.

[192] R. Tripathi, N. Nassif, J. S. Nelson, B. H. Park, and J. F. de Boer, "Spectral shaping for non-gaussian source spectra in optical coherence tomography," *Opt. Lett.* **27**, pp. 406–408, 2002.

[193] M. Szkulmowski, M. Wojtkowski, T. Bajraszewski, I. Gorczyńska, P. Targowski, W. Wasilewski, A. Kowalczyk, and C. Radzewicz, "Quality improvement for high resolution in vivo images by spectral domain optical coherence tomography with supercontinuum source," *Opt. Commun.* **246**(4-6), pp. 569–578, 2005.

[194] A. C. Akcay, J. P. Rolland, and J. M. Eichenholz, "Spectral shaping to improve the point spread function in optical coherence tomography," *Opt. Lett.* **28**, pp. 1921–1923, 2003.

[195] B. R. Biedermann, W. Wieser, C. M. Eigenwillig, G. Palte, D. C. Adler, V. J. Srinivasan, J. G. Fujimoto, and R. Huber, "Real time en face Fourier-domain optical coherence tomography with direct hardware frequency demodulation," *Opt. Lett.* **33**, pp. 2556–2558, 2008.

[196] S. Hariri, A. A. Moayed, A. Dracopoulos, C. Hyun, S. Boyd, and K. Bizheva, "Limiting factors to the OCT axial resolution for in-vivo imaging of human and rodent retina in the 1060nm wavelength range," *Opt. Express* **17**, pp. 24304–24316, 2009.

[197] S. H. Yun, D. J. Richardson, and B. Y. Kim, "Interrogation of fiber grating sensor arrays with a wavelength-swept fiber laser," *Opt. Lett.* **23**, pp. 843–845, 1998.

[198] F. D. Nielsen, L. Thrane, J. Black, K. Hsu, A. Bjarklev, and P. E. Andersen, "Swept-wavelength sources for optical coherence tomography in the 1 µm range," *Proc. SPIE* **5861**, p. 58610H, 2005.

[199] R. Huber, M. Wojtkowski, K. Taira, J. G. Fujimoto, and K. Hsu, "Amplified, frequency swept lasers for frequency domain reflectometry and OCT imaging: Design and scaling principles," *Opt. Express* **13**(9), pp. 3513–3528, 2005.

[200] M. K. Harduar, A. Mariampillai, B. Vuong, K. H. Y. Cheng, L. R. Chen, X. Gu, B. A. Standish, and V. X. D. Yang, "Dual core ytterbium doped fiber ring laser in Fourier domain mode locked operation for swept-source optical coherence tomography," *Proc. SPIE* **7580**, p. 75802S, 2010.

[201] K. Sumimura, H. Yoshida, H. Okada, H. Fujita, and M. Nakatsuka, "Suppression of self pulsing in yb-doped fiber lasers with cooling by liquid nitrogen," *Proceedings of Conference on Lasers and Electro-Optics – Pacific Rim* , 2007.

[202] S.-H. Yun, C. Boudoux, G. J. Tearney, and B. E. Bouma, "High-speed wavelength-swept semiconductor laser with a polygon-scanner-based wavelength filter," *Opt. Lett.* **28**(20), pp. 1981–1983, 2003.

[203] W.-Y. Oh, S.-H. Yun, G. J. Tearney, and B. E. Bouma, "115 kHz tuning repetition rate ultrahigh-speed wavelength-swept semiconductor laser," *Opt. Lett.* **30**(23), pp. 3159–3161, 2005.

[204] K. Totsuka, K. Isamoto, T. Sakai, A. Morosawa, and C. Chong, "MEMS scanner based swept source laser for optical coherence tomography," *Proc. SPIE* **7554**, p. 75542Q, 2010.

[205] S. Yagi, K. Naganuma, T. Imai, Y. Shibata, S. Ishibashi, Y. Sasaki, M. Sasaura, K. Fujiura, and K. Kato, "A mechanical-free 150-

kHz repetition swept light source incorporated a ktn electro-optic deflector," *Proc. SPIE* **7889**(1), p. 78891J, 2011.

[206] T. Suzuki, R. ichi Nagai, O. Sasaki, and S. Choi, "Rapid wavelength scanning based on acousto-optically tuned external-cavity laser diode," *Opt. Commun.* **284**(19), pp. 4615–4618, 2011.

[207] C. M. Eigenwillig, B. R. Biedermann, G. Palte, and R. Huber, "K-space linear Fourier domain mode locked laser and applications for optical coherence tomography," *Opt. Express* **16**, pp. 8916–8937, 2008.

[208] R. Huber, D. C. Adler, and J. G. Fujimoto, "Buffered fourier domain mode locking: unidirectional swept laser sources for optical coherence tomography imaging at 370,000 lines/s," *Opt. Lett.* **31**(20), pp. 2975–2977, 2006.

[209] A. Bilenca, S. H. Yun, G. J. Tearney, and B. E. Bouma, "Numerical study of wavelength-swept semiconductor ring lasers: the role of refractive-index nonlinearities in semiconductor optical amplifiers and implications for biomedical imaging applications," *Opt. Lett.* **31**, pp. 760–762, 2006.

[210] S. Marschall, T. Klein, W. Wieser, B. R. Biedermann, K. Hsu, K. P. Hansen, B. Sumpf, K.-H. Hasler, G. Erbert, O. B. Jensen, C. Pedersen, R. Huber, and P. E. Andersen, "Fourier domain mode-locked swept source at 1050 nm based on a tapered amplifier," *Opt. Express* **18**(15), pp. 15820–15831, 2010.

[211] W.-Y. Oh, B. J. Vakoc, M. Shishkov, G. J. Tearney, and B. E. Bouma, ">400 kHz repetition rate wavelength-swept laser and application to high-speed optical frequency domain imaging," *Opt. Lett.* **35**, pp. 2919–2921, 2010.

[212] C. M. Eigenwillig, B. R. Biedermann, W. Wieser, and R. Huber, "Wavelength swept amplified spontaneous emission source," *Opt. Express* **17**, pp. 18794–18807, 2009.

[213] S. Moon and D. Y. Kim, "Ultra-high-speed optical coherence tomography with a stretched pulse supercontinuum source," *Opt. Express* **14**, pp. 11575–11584, 2006.

[214] H. Song, S. B. Cho, D. U. Kim, S. Jeong, and D. Y. Kim, "Ultra-high-speed phase-sensitive optical coherence reflectometer with a stretched pulse supercontinuum source," *Appl. Opt.* **50**, pp. 4000–4004, 2011.

[215] S. Yamashita and Y. Takubo, "Fast wavelength-swept dispersion-tuned fiber laser over 500khz using a wideband chirped fiber bragg grating," *Proc. SPIE* **7753**(1), p. 77537W, 2011.

[216] G. Lamouche, S. Vergnole, Y. Kim, B. Burgoyne, and A. Villeneuve, "Tailoring wavelength sweep for ss-oct with a programmable picosecond laser," *Proc. SPIE* **7889**(1), p. 78891L, 2011.

[217] V. Jayaraman, J. Jiang, H. Li, P. Heim, G. Cole, B. Potsaid, J. G. Fujimoto, and A. Cable, "OCT imaging up to 760 kHz axial scan rate using single-mode 1310 nm MEMS-tunable VCSELs with >100 nm tuning range," *CLEO:2011 - Laser Applications to Photonic Applications* , p. PDPB2, 2011.

[218] S. O'Connor, M. A. Bernacil, A. DeKelaita, B. Maher, and D. Derickson, "100 kHz axial scan rate swept-wavelength OCT using sampled grating distributed bragg reflector lasers," *Proc. SPIE* **7168**, pp. 716825–8, 2009.

[219] M. P. Minneman, J. Ensher, M. Crawford, and D. Derickson, "All-semiconductor high-speed akinetic swept-source for OCT," *Proc. SPIE* **8311**, p. 831116, 2011.

[220] E. D. Moore and R. R. McLeod, "Correction of sampling errors due to laser tuning rate fluctuations in swept-wavelength interferometry," *Opt. Express* **16**, pp. 13139–13149, 2008.

[221] M. Choma, M. Sarunic, C. Yang, and J. Izatt, "Sensitivity advantage of swept source and fourier domain optical coherence tomography," *Opt. Express* **11**(18), pp. 2183–2189, 2003.

[222] R. Leitgeb, C. K. Hitzenberger, and A. F. Fercher, "Performance of fourier domain vs. time domain optical coherence tomography," *Opt. Express* **11**(8), pp. 889–894, 2003.

[223] P. Groß, B. Adhimoolam, M. E. Klein, I. D. Lindsay, K. Hsu, and K.-J. Boller, "9-watt cw swept-wavelength diode-oscillator Yb-fiber-amplifier system," *Proceedings of Conference on Lasers and Electro-Optics/Quantum Electronics and Laser Science* , p. CFG5, 2006.

[224] B. Adhimoolam, M. E. Klein, I. D. Lindsay, P. Groß, C. J. Lee, and K.-J. Boller, "Widely and rapidly tunable semiconductor master-oscillator fiber amplifier around 1080 nm," *IEEE Photonic Tech. L.* **18**(24), pp. 2683–2685, 2006.

[225] M. Chi, O. B. Jensen, J. Holm, C. Pedersen, P. E. Andersen, P. M. Petersen, G. Erbert, and B. Sumpf, "Tunable high-power narrow-linewidth semiconductor laser based on an external-cavity tapered amplifier," *Opt. Express* **13**(26), pp. 10589–10607, 2005.

[226] S. Marschall, L. Thrane, P. E. Andersen, C. Pedersen, and K. Hsu, "Frequency-swept laser light source at 1050 nm with higher bandwidth due to multiple semiconductor optical amplifiers in series," *Proc. SPIE* **7168**(1), p. 716824, 2009.

[227] M. K. K. Leung, A. Mariampillai, B. A. Standish, K. K. Lee, N. R. Munce, I. A. Vitkin, and V. X. D. Yang, "High-power

wavelength-swept laser in Littman telescope-less polygon filter and dual-amplifier configuration for multichannel optical coherence tomography," *Opt. Lett.* **34**(18), pp. 2814–2816, 2009.

[228] Y. Wang, W. Liu, J. Fu, and D. Chen, "Quasi-distributed fiber bragg grating sensor system based on a fourier domain mode locking fiber laser," *Laser Phys.* **19**(3), pp. 450–454, 2009.

[229] M. Haverkamp, G. Kochem, and K. Boucke, "Single mode fiber coupled tapered laser module with frequency stabilized spectrum," *Proc. SPIE* **6876**, 2008.

[230] M. Y. Jeon, J. Zhang, and Z. Chen, "Characterization of fourier domain mode-locked wavelength swept laser for optical coherence tomography imaging," *Opt. Express* **16**(6), pp. 3727–3737, 2008.

[231] R. Paschotta, J. Nilsson, A. Tropper, and D. Hanna, "Ytterbium-doped fiber amplifiers," *IEEE J. Quantum Elect.* **33**, pp. 1049–1056, 1997.

[232] M. Y. Jeon, J. Zhang, Q. Wang, and Z. Chen, "High-speed and wide bandwidth fourier domain mode-locked wavelength swept laser with multiple SOAs," *Opt. Express* **16**(4), pp. 2547–2554, 2008.

[233] D. J. J. Park and J. Karesh, *Duane's Foundations of Clinical Ophthalmology*, vol. 1, ch. 1. Topographic Anatomy of the Eye: An Overview. Lippincott Williams & Wilkins, 2006. accessed online: `www.oculist.net/downaton502/prof/ebook/duanes/pages/v7/v7c001.html`.

[234] M. Pircher, E. Götzinger, O. Findl, S. Michels, W. Geitzenauer, C. Leydolt, U. Schmidt-Erfurth, and C. K. Hitzenberger, "Human macula investigated in vivo with polarization-sensitive optical coherence tomography," *Invest. Ophth. Vis. Sci.* **47**(12), pp. 5487–5494, 2006.

[235] Y. Yasuno, Y. Hong, S. Makita, M. Yamanari, M. Akiba, M. Miura, and T. Yatagai, "In vivo high-contrast imaging of deep posterior eye by 1-μm swept source optical coherence tomography and scattering optical coherence angiography," *Opt. Express* **15**, pp. 6121–6139, 2007.

[236] R. Ulrich, S. C. Rashleigh, and W. Eickhoff, "Bending-induced birefringence in single-mode fibers," *Opt. Lett.* **5**, pp. 273–275, 1980.

[237] H. Gray, *Anatomy of the human body*, ch. X.1.c.1. The Tunics of the Eye. Philadelphia: Lea & Febiger, 20 ed., 1918. accessed online: `www.bartleby.com/107/225.html`.

[238] E. Götzinger, M. Pircher, and C. K. Hitzenberger, "High speed spectral domain polarization sensitive optical coherence tomography of the human retina," *Opt. Express* **13**(25), pp. 10217–10229, 2005.

[239] E. Götzinger, M. Pircher, B. Baumann, T. Schmoll, H. Sattmann, R. A. Leitgeb, and C. K. Hitzenberger, "Speckle noise reduction in high speed polarization sensitive spectral domain optical coherence tomography," *Opt. Express* **19**, pp. 14568–14585, 2011.

ISBN: 87-92062-81-4

Published by:
DTU Fotonik
Department of Photonics Engineering
Technical University of Denmark
Ørsteds Plads, building 343
DK-2800 Kgs. Lyngby

Sebastian Marschall majored in physics at the Technical University of Darmstadt, Germany, including one year as exchange student at DTU. After receiving his Diplom in 2008, he joined the group of Prof. Peter E. Andersen at DTU Fotonik, where he conducted his project on frequency-swept laser light sources for optical coherence tomography. He defended his thesis and received the Ph.D. degree in 2012. Sebastian is founding member of the SPIE student chapter at DTU, and became its first president from 2010 to 2011.

DTU Fotonik
Department of Photonics Engineering

Printed in Denmark by SaloPrint, 2620 Albertslund